UNIVERSITY OF CALIFORNIA SAN DIEGO

Non-invasive neuromodulation using ultrasound: mechanisms of action and device design

A Dissertation submitted in partial satisfaction of the
requirements for the degree
Doctor of Philosophy

in

Engineering Sciences (Mechanical Engineering)

by

Aditya Vasan

Committee in charge:

Professor James R. Friend, Chair
Professor Sreekanth Chalasani
Professor Adam Engler
Professor Vishwanathan Krishnan
Professor Lisa Poulikakos

2023

The dissertation of Aditya Vasan is approved, and it is acceptable in quality and form for publication on microfilm and electronically.

University of California San Diego

2023

DEDICATION

To everyone who came before me. This body of work would not have been possible without everyone who believed and supported me, even in ways they might think are insignificant.

EPIGRAPH

"So we shall let the reader answer this question for himself: who is the happier man, he who has braved the storm of life and lived or he who has stayed securely on shore and merely existed? "

—Hunter S Thompson

TABLE OF CONTENTS

Dissertation Approval Page . . . iii

Dedication . . . iv

Epigraph . . . v

Table of Contents . . . vi

List of Figures . . . ix

List of Tables . . . x

Acknowledgements . . . xi

Vita . . . xiv

Abstract of the Dissertation . . . xvi

Chapter 1 Piezoelectric devices for atomization and acoustofluidics . . . 1
1.1 Introduction . . . 2
1.1.1 Protocol . . . 3
1.2 Representative Results . . . 9
1.2.1 Discussion . . . 10
1.3 Acknowledgements . . . 14

Chapter 2 Microscale concert hall acoustics to produce uniform ultrasound stimulation for targeted sonogenetics in hsTRPA1-transfected cells . . . 17
2.1 Chapter Abstract . . . 17
2.2 Introduction . . . 18
2.3 Results . . . 21
2.4 Discussion . . . 26
2.5 Methods . . . 28
2.6 Acknowledgements . . . 32

Chapter 3 Ultrasound mediated cellular deflection results in cellular depolarization . . . 35
3.1 Chapter Abstract . . . 35
3.2 Introduction . . . 36
3.3 Results . . . 41
3.3.1 Digital holographic imaging of cell membrane deflection . . . 41
3.3.2 Membrane deflection model . . . 43
3.3.3 Model prediction of action potentials and electrophysiology . . . 46
3.4 Discussion . . . 47
3.5 Methods . . . 50
3.5.1 HEK293 cell culture . . . 50
3.5.2 High-speed digital holographic microscopy . . . 50
3.5.3 Modeling of deflection and transmembrane voltage changes . . . 51
3.5.4 Sustaining oscillations on the membrane . . . 57

3.5.5 Ultrasound transducer fabrication . . . 58
3.5.6 Rat Primary Neuron Culture . . . 59
3.5.7 *In-vitro* electrophysiology . . . 59
3.5.8 Statistical Analysis . . . 60
3.6 Acknowledgements . . . 61

Chapter 4 Ultrasonic interrogation of neural circuits: Non-invasive methods for probing activity . . . 64
4.1 Chapter Abstract . . . 64
4.2 Introduction . . . 65
4.2.1 Two-photon imaging of ultrasound-evoked activity in visual cortex 66
4.2.2 A new ultrasound transducer for modulating neural activity in freely moving mice . . . 68
4.2.3 Stereotactic placement of device . . . 70
4.2.4 Ultrasound-evoked activation of striatum in freely moving mice . . 71
4.3 Discussion . . . 73
4.4 Methods . . . 74
4.4.1 Ultrasound transducers . . . 74
4.4.2 Ex-vivo hydrophone measurements . . . 74
4.4.3 Rotarod Assay . . . 75
4.4.4 Two-photon imaging . . . 75
4.4.5 Viral Injections and Implants . . . 75
4.4.6 Fiber photometry recordings . . . 76
4.4.7 Immunohistochemistry . . . 77
4.5 Acknowledgements . . . 77

Chapter 5 Conclusions . . . 78

Appendix A Medical Devices for Low and Middle Income Countries: A Review and Directions for Development . . . 81
A.1 Chapter Abstract . . . 81
A.2 Introduction . . . 82
A.3 Melioidosis . . . 82
A.4 Heavy metal and organophosphate contamination of water . . . 85
A.5 Neonatal mortality . . . 87
A.6 Neglected tropical diseases . . . 90
A.7 Policy and implementation . . . 93
A.8 Acknowledgement . . . 94

Appendix B MADVent: A low-cost ventilator for patients with COVID-19 . . . 95
B.1 Chapter Abstract . . . 95
B.2 Introduction . . . 96
B.3 Design of an automated self-inflating bag-based ventilator: MADVent Mark V . . . 99
B.4 Results . . . 104
B.5 Discussion . . . 110
B.6 Conclusions . . . 113
B.7 Acknowledgement . . . 114

Appendix C Supplementary information for chapter 3 115

Bibliography 120

LIST OF FIGURES

Figure 1.1: The real s_{11} scattering parameter values measured over a range of 1–25 MHz for a 127.86° YX lithium niobate device, indicating the presence of a resonance peak at approximately 7 MHz . . . 10
Figure 1.2: Example of an LDV scan on a thickness mode transducer . . . 11
Figure 1.3: Onset of capillary waves on a 2 μL water drop . . . 15
Figure 1.4: Droplet size distribution of atomized droplets using thickness mode transducer . 16

Figure 2.1: Design of the Schrörder Diffuser . . . 21
Figure 2.2: Simulations of pressure profile *in-vitro* . . . 23
Figure 2.3: Isofrequency contours with and without the diffuser . . . 25
Figure 2.4: Imaging HEK cell activity *in vitro* with the diffuser . . . 33
Figure 2.5: *Ex vivo* validation of diffuser . . . 34

Figure 3.1: High-speed DHM imaging of membrane deflection. . . . 42
Figure 3.2: Prediction of membrane deflection due to ultrasound . . . 62
Figure 3.3: Displacement driven capacitance changes result in action potential generation . 63

Figure 4.1: Simultaneous two-photon imaging and ultrasound stimulation of visual cortex. . 67
Figure 4.2: MMCX device fabrication and characterization for transcranial ultrasound neuromodulation of freely moving mice. . . . 69
Figure 4.3: Device implant procedure . . . 70
Figure 4.4: Simultaneous fiber photometry recordings and transcranial ultrasound stimulation in an awake, freely moving mouse . . . 72

Figure A.1: Worldwide infant mortality rates in 2017 . . . 88
Figure A.2: Incidence of neglected tropical diseases in 2015 . . . 91

Figure B.1: Test setup for MADVent including lung simulator . . . 98
Figure B.2: Render of production version of MADVent . . . 101
Figure B.3: Validation of pressure-controlled version of MADVent . . . 105
Figure B.4: Model for estimating tidal volume . . . 107
Figure B.5: Validation of volume-controlled version of MADVent . . . 109

Figure C.1: Current clamp electrophysiology . . . 115
Figure C.2: Modeling the Rayleigh-Plesset equation . . . 118
Figure C.3: Sustained oscillations on the membrane due as depicted by changes in the Ohnesorge number . . . 119

LIST OF TABLES

Table B.1: Suitable MADVent Mark V operating parameter ranges 108

ACKNOWLEDGEMENTS

All the work that led to this dissertation would not have been possible without support from a vast network of people. This includes people within my professional network at UCSD but also people I have encountered in life before moving to San Diego. This section of my dissertation is an attempt to capture their influence on the way I think and how they have shaped me as a researcher.

I first met with Professor James Friend on a campus visit to UCSD in March 2017. I recall how he patiently explained the various projects we could work on, his mentorship style and living in San Diego. I remember entering that meeting unsure if I'd made the right decision to leave a stable and potentially fulfilling career in industry. I left that meeting feeling inspired, energized, and reassured that I'd made the right decision. This has been a recurring theme over the course of my PhD and Professor Friend's measured advice and outlook on life have been a big influence on how I approach problems both within and outside the academic realm. Conversations and collaborations within the group have been incredibly fulfilling over the years – thanks Dr. Gopesh Tilwavala, Dr. An Huang, Dr. Jiyang Mei, Dr. Naiqing Zhang, Shuai, Dr. Jeremy Orosco and Dr. William Connacher.

I am fortunate to have a committee of Professors who are experts in their respective fields of study. Input from Prof. Adam Engler, Prof. Lisa Poulikakos, Prof. Vish Krishnan and Prof. Sreekanth Chalasani have helped this work come together over the years. Professor Sreekanth "Shrek" Chalasani has been a source of inspiration and I remember being excited about sonogenetics from the first day we met. I have also felt like I have been a part of two research groups since I started collaborating with Professor Chalasani – thank you for accommodating me and your willingness to collaborate. Of the many people at the Salk I have worked with over the years, my collaboration with Dr. Uri Magaram has resulted in a body of work that I am most proud of. It has also, at the time of writing this, led to ideas that will form the basis of a startup that I hope to pursue after defending my dissertation. Others in the Shrek lab that I'm indebted to include Dr. Yusuf Tufail and Dr. Corinne Lee Kubli – thank you for taking the time to answer all my questions related to the fundamentals of neuroscience as I was new to the project. Janki Patel, Mark Duque, and Connor Watson – thank you for your help over the years. My work on the Schroeder diffuser would not have been possible without input from Professor Nicholas Boechler and Dr. Florian

Allein, I can confidently say that working with them improved my analytical abilities.

The COVID-19 pandemic was a challenging time but was also a period when I got to lead an interdisciplinary project solving a pressing unmet clinical need. In March 2020, we received news that hospitals around the country were facing a shortage of ventilators due to supply chain limitations. This started out as a project in my garage and went on to become one that involved 15 people across multiple departments at UCSD. Thanks to Dr. Lonnie Petersen, Dr. Dan Lee for their clinical input, Reiley and Bill for working long hours with me as we tried to complete this project on a short timeline, and Mark for being there every step of the way and making sure we were all having a good time.

Working at St Jude Medical's cardiovascular division before starting my PhD and conducting a research internship at Facebook Reality Labs during my PhD have had an impact on how I direct my research. These experiences have enabled me to think of real-world impact of research projects I am pursuing and helped me translate ideas I generate in the lab to potential products or therapies that have real-world applications. I am grateful for institutions on campus that have supported my entrepreneurial pursuits: the Institute for the Global Entrepreneur for supporting me through the years and, Nucleate for providing me with a community of like-minded graduate students. The people who I have to thank for this are Professor Amy Nguyen-Chyung, Professor Vish Krishnan, Avi Bilu, Dr. Laura Matloff, and many more.

There are a few people I have had the privilege of meeting in San Diego that I am sure will remain lifelong friends. Bill was one of the first - no one I know stands up for things they believe in as well as he does. Alera, Austin, Ray, Teodora, Connor, Esther, Alyssa, Reiley, Emily, and Patrice for lighthearted conversations and shared interests that got me through some tough times.

Finally, I find that it's incredible I ended up in the position I am in now: I am writing this section of my dissertation by the beach, over 9000 miles from home and my thoughts go out to my family for being a constant source of support despite being so far away. Mom, dad, paati, Akhi, Jayant, Maya, Vik, and the multitude of aunts, uncles, and cousins - thank you for always believing in me.

Chapter 1, in full, is a reprint of Aditya Vasan, William Connacher, and James Friend. "Fabrication and Characterization of Thickness Mode Piezoelectric Devices for Atomization and Acoustofluidics." *JoVE (Journal of Visualized Experiments)* 162 (2020): e61015. The dissertation

author is the first author of this article.

Chapter 2, in full, is a reprint of Aditya Vasan, Florian Allein, Marc Duque, Uri Magaram, Nicholas Boechler, Sreekanth H. Chalasani, and James Friend. "Microscale Concert Hall Acoustics to Produce Uniform Ultrasound Stimulation for Targeted Sonogenetics in hsTRPA1-Transfected Cells." Advanced NanoBiomed Research 2, no. 5 (2022): 2100135. The dissertation author is the first author of this article.

Chapter 3, in full, is a reprint of Aditya Vasan, Jeremy Orosco, Uri Magaram, Marc Duque, Connor Weiss, Yusuf Tufail, Sreekanth H. Chalasani, and James Friend. "Ultrasound mediated cellular deflection results in cellular depolarization." Advanced Science 9, no. 2 (2022): 2101950. The dissertation author is the first author of this article.

Chapter 4, in full, has been submitted for publication of the material as it may appear: Aditya Vasan, Uri Magaram, Kirstie Salinas, Janki Patel, Ed Callaway, James Friend, Sreekanth Chalasani (2023) "Integrating ultrasound-induced neural activity modulation with two-photon microscopy and fiber photometry" *In Review.* The dissertation author is the first author of this article.

Appendix A, in full, is a reprint of Aditya Vasan and James Friend (2020) "Medical Devices for Low-and Middle-Income Countries: A Review and Directions for Development" *Journal of Medical Devices* 125(20), 205108. The dissertation author is the first author of these articles.

Appendix B, in full, is a reprint of Aditya Vasan, Reiley Weekes, William Connacher, Jeremy Sieker, Mark Stambaugh, Preetham Suresh, Daniel E. Lee , William Mazzei, Eric Schlaepfer, Theodore Vallejos, John Petersen, Sidney Merritt, Lonnie Petersen, James Friend. "MADVent: A low-cost ventilator for patients with COVID-19." *Medical devices & sensors* 3, no. 4 (2020). The dissertation author is the first author of this material.

VITA

2023	Ph. D. in Engineering Sciences (Mechanical Engineering), University of California San Diego
2015	M. S. in Mechanical Engineering, University of California Los Angeles
2014	B. S. in Mechanical Engineering, M. S. Ramaiah Institute of Technology

PUBLICATIONS

Aditya Vasan William Connacher, and James Friend. "Fabrication and Characterization of Thickness Mode Piezoelectric Devices for Atomization and Acoustofluidics." *JoVE (Journal of Visualized Experiments)* 162 (2020), doi: 10.3791/61015

Aditya Vasan Reiley Weekes, William Connacher, Jeremy Sieker, Mark Stambaugh, Preetham Suresh, Daniel E. Lee , William Mazzei, Eric Schlaepfer, Theodore Vallejos, John Petersen, Sidney Merritt, Lonnie Petersen, James Friend. "MADVent: A low-cost ventilator for patients with COVID-19." *Medical devices & sensors* 3, no. 4 (2020), doi:10.1002/mds3.10106

Aditya Vasan and James Friend (2020) "Medical Devices for Low-and Middle-Income Countries: A Review and Directions for Development" *Journal of Medical Devices* 125(20), 205108, doi: 10.1115/1.4045910.

Aditya Vasan, Jeremy Orosco, Uri Magaram, Marc Duque, Connor Weiss, Yusuf Tufail, Sreekanth H. Chalasani, and James Friend. "Ultrasound mediated cellular deflection results in cellular depolarization." Advanced Science 9, no. 2 (2022): 2101950, doi: 10.1002/advs.202101950.

Aditya Vasan Florian Allein, Marc Duque, Uri Magaram, Nicholas Boechler, Sreekanth H. Chalasani, and James Friend. "Microscale Concert Hall Acoustics to Produce Uniform Ultrasound Stimulation for Targeted Sonogenetics in hsTRPA1-Transfected Cells." Advanced NanoBiomed Research 2, no. 5 (2022), doi: 10.1002/anbr.202100135.

Aditya Vasan, Uri Magaram, Kirstie Salinas, Janki Patel, Ed Callaway, James Friend, Sreekanth Chalasani (2023) "Integrating ultrasound-induced neural activity modulation with two-photon microscopy and fiber photometry." *In Review.*

Alex Phan, Phuong Truong, Christoph Schade, Aditya Vasan, Friend, James "Drift of an intraocular pressure sensor." Microsystem Technologies 27.6 (2021): 2473-2479, doi: s00542-020-05164-2.

Marc Duque, Corinne A. Lee-Kubli, Yusuf Tufail, Uri Magaram, Janki Patel, Ahana Chakraborty, Jose Mendoza Lopez, Eric Edsinger, Aditya Vasan, Rani Shiao, Connor Weiss, James Friend, Sreekanth H. Chalasani "Sonogenetic control of mammalian cells using exogenous TRPA1 channels." Nature communications 13.1 (2022): 1-17, doi: 10.1038/s41467-022-28205-y.

Jiyang Mei, Aditya Vasan, Uri Magaram, Kenjiro Takemura, Sreekanth H. Chalasani, and James Friend. "Well-free agglomeration and on-demand three-dimensional cell cluster formation using guided surface acoustic waves through a couplant layer." Biomedical Microdevices 24, no. 2 (2022): 1-13., doi: 10.1007/s10544-022-00617-z.

Uri Magaram, Connor Weiss, Aditya Vasan, Kirthi C. Reddy, James Friend, and Sreekanth H. Chalasani. "Two pathways are required for ultrasound-evoked behavioral changes in Caenorhabditis elegans." PloS one 17, no. 5 (2022), doi: 10.1371/journal.pone.0267698

PATENTS

Aditya Vasan, Sreekanth H. Chalasani, James Friend, "System to create uniform ultrasound fields in enclosed cavities and methods of manufacture thereof." US Provisional Patent Application 63/194,162. 27 May 2021.

Aditya Vasan, Jeremy Orosco, Sreekanth H. Chalasani, James Friend, "System to predict neuronal activity due to ultrasound stimulation." US Provisional Patent Application 63/194,168. 27 May 2021.

Aditya Vasan, Uri Magaram, Sreekanth H. Chalasani, James Friend "Method of non-invasive cellular stimulation." US Provisional Patent Application 63/194,168. 27 May 2021.

ABSTRACT OF THE DISSERTATION

Non-invasive neuromodulation using ultrasound: mechanisms of action and device design

by

Aditya Vasan

Doctor of Philosophy in Engineering Sciences (Mechanical Engineering)

University of California San Diego, 2023

Professor James R. Friend, Chair

Modulating neuronal activity has implications for treating neurological disorders like Parkinson's disease, major depressive disorder, and drug-resistant epilepsy. Clinical neuromodulation is typically achieved by supplying electrical current to specific populations of neurons, thus triggering or inhibiting their activity. Apart from these clinical applications, advances in neuromodulation have enabled fundamental advances in our understanding of neural circuits. Some novel neuromodulation techniques that have emerged recently and enabled the elucidation of neural circuit function are optogenetics, chemogenetics, magnetogenetics, and sonogenetics.

Ultrasound neuromodulation and sonogenetics have the advantage of being non-invasive neuromodulation techniques. These methods have a high spatial and temporal resolution in comparison to others being developed and this makes them an attractive option for eventual clinical

translation. One of the key limitations in ultrasound neuromodulation is a lack of an understanding of the underlying mechanism of action of ultrasound on neurons. Specifically, it is unknown how mechanical energy carried by a sound wave is converted to the electrical activity of a neuron and an accurate understanding of the mechanism of action is critical to enable parameter selection and safety. The second key limitation in the field is the lack of devices specifically made for neuromodulation. Ultrasound has historically been used as an imaging modality but such devices are unsuitable for neuromodulation purposes. They cannot be driven at sufficient pressure without resulting in significant heating of tissue. This work seeks to address both of these limitations in the field.

Intramembrane cavitation and lipid clustering have been proposed as likely mechanisms of ultrasound neuromodulation but they lack experimental evidence. We use high-speed digital holographic imaging to visualize membrane dynamics under the influence of ultrasound. We also develop a biophysical framework that couples ultrasound-induced pressure changes with a Hodgkin-Huxley neuron model to predict neuronal responses at relevant pressures. This work collectively demonstrates that membrane perturbations due to ultrasound result in the generation of action potentials. It provides a mechanism for both ultrasound-evoked neurostimulation and sonogenetic control.

We also address the phenomenon of standing acoustic waves in the skull producing large variations in pressure, leading to localized tissue damage and disruption of normal brain function. Our approach to overcome this involves the development of novel transducer-mounted diffusers that result in spatiotemporally incoherent ultrasound. We demonstrate the effectiveness of the diffuser both computationally and experimentally, and, show that the use of the diffuser results in a twofold increase in ultrasound responsiveness in cells with a sonogenetic candidate.

Finally, we demonstrate the development of tools for conducting ultrasound neuromodulation studies *in vivo*. These include a transparent ultrasound transducer that we use with a two-photon microscope to study ultrasound-induced activation of paravalbumin positive neurons interneurons in the rodent visual cortex. We also develop a head-mounted transducer that can be combined with a fiber photometry system to stimulate activity in cholinergic neurons in the striatum.

Chapter 1

Piezoelectric devices for atomization and acoustofluidics

We present a technique to fabricate simple thickness mode piezoelectric devices using lithium niobate (LN). Such devices have been shown to atomize liquid more efficiently, it terms of flow rate per power input, than those that rely on Rayleigh waves and other modes of vibration in LN or PZT. The complete device is composed of a transducer, a transducer holder, and a fluid supply system. The fundamentals of acoustic liquid atomization are not well known, so we also present techniques to characterize the devices and to study the phenomena. Laser Doppler vibrometry (LDV) provides vibration information essential in comparing acoustic transducers and, in this case, indicates whether a device will perform well in thickness vibration. It can also be used to find the resonance frequency of the device, though this information is obtained more quickly via impedance analysis. Continuous fluid atomization requires careful fluid supply and we present such a method. Once the device is characterized and complete, the dynamics involved can be studied with high-speed imaging and the droplet size distribution can be measured with laser scattering. Fabrication of piezoelectric thickness mode transducers via DC sputtering of plate electrodes on lithium niobate is described. Additionally, reliable operation is achieved with a transducer holder and fluid supply system and characterization is demonstrated via impedance analysis, laser doppler vibrometry, high-speed imaging, and droplet size distribution using laser scattering.

1.1 Introduction

Ultrasound atomization has been studied for almost a century and although there are many applications, there are limitations in understanding the underlying physics. The first description of the phenomenon was made by Wood and Loomis in 1927 [1], and since then there have been developments in the field for applications ranging from delivering aerosolized pharmaceutical fluids [2] to fuel injection [3]. Although the phenomenon works well in these applications, the underlying physics is not well understood [4–6].

A key limitation in the field of *ultrasonic* atomization is the choice of material used, lead zirconate titanate (PZT); a hysteretic material prone to heating [7] and lead contamination with elemental lead available from the inter-grain boundaries [8, 9]. Grain size and mechanical and electronic properties of grain boundaries also limit the frequency at which PZT can operate [10]. By contrast, lithium niobate is both lead-free and exhibits no hysteresis [11], and can be used to atomize fluids an order of magnitude more efficiently than commercial atomizers [12]. The traditional cut of lithium niobate used for operation in the thickness mode is the 36-degree Y-rotated cut, but the 127.86-degree Y-rotated, X-propagating cut (128YX), typically used for surface acoustic wave generation, has been shown to have a higher surface displacement amplitude in comparison with the 36-degree cut [13] when operated in resonance and low loss. It has also been shown that thickness-mode operation offers an order of magnitude improvement in atomizer efficiency over other modes of vibration [13], even when using LN.

The resonance frequency of a piezoelectric device operating in the thickness mode is governed by its thickness, t: the wavelength $\lambda = 2t/n$ where $n = 1, 2, \ldots$ is the number of anti-nodes. For a 500 μm thick substrate, this corresponds to a wavelength of 1 mm for the fundamental mode, which can then be used to calculate the fundamental resonance frequency, $f = v/\lambda$ if the wave speed, v, is known. The speed of sound through the thickness of 128YX LN is approximately 7000 m/s, and so $f = 7$ MHz. Unlike other forms of vibration, particularly surface-bound modes, it is straightforward to excite higher-order thickness-mode harmonics to much higher frequencies, here to 250 MHz or more, though only the odd-numbered modes may be excited by uniform electric fields [14]. Consequently, the first harmonic ($n = 2$) near 14 MHz cannot be excited, but the second harmonic

at 21 MHz ($n = 3$) can. Fabrication of efficient thickness mode devices requires depositing electrodes onto opposing faces of the transducer. We use *direct current* (DC) sputtering to accomplish this, but electron-beam deposition and other methods could be used. Impedance analysis is useful to characterize the devices, particularly in finding the resonance frequencies and electromechanical coupling at these frequencies. Laser Doppler vibrometry (LDV) is useful to determine the output vibration amplitude and velocity without contact or calibration [15], and, via scanning, the LDV provides the spatial distribution of surface deformation, revealing the mode of vibration associated with a given frequency. Finally, for the purposes of studying atomization and fluid dynamics, high-speed imaging can be employed as a technique to study the development of capillary waves on the surface of a sessile drop [16, 17]. In atomization, small droplets are produced at a rapid rate, over 1 kHz in a given location, too quickly for high-speed cameras to observe with sufficient fidelity and field of view to provide useful information over a sufficiently large droplet sample size. Laser scattering may be used for this purpose, passing the droplets through an expanded laser beam to (Mie) scatter some of the light in reflection and refraction to produce a characteristic signal that may be used to statistically estimate the droplet size distribution.

It is straightforward to fabricate piezoelectric thickness-mode transducers, but the techniques required in device and atomization characterization have not been clearly stated in the literature to date, hampering progress in the discipline. In order for a thickness-mode transducer to be effective in an atomization device, it must be mechanically isolated so that its vibration is not damped and it must have a continuous fluid supply with a flow rate equal to the atomization rate so that neither dryout nor flooding occur. These two practical considerations have not been thoroughly covered in the literature because their solutions are the result of engineering techniques rather than pure scientific novelty, but they are nonetheless critical to studying the phenomenon. We present a transducer holder assembly and a liquid wicking system as solutions. Our protocol offers a systematic approach to atomizer fabrication and characterization for facilitating further research in fundamental physics and myriad applications.

1.1.1 Protocol

1. Thickness-mode device fabrication via DC sputtering

1.1 Wafer preparation

1.1.1 Place a 100 mm 128YX LN wafer in a clean PYREX dish of at least 125 mm diameter. Sonicate the wafer in at least 200 mL of acetone for 5 minutes.

1.1.2 Repeat sonication with isopropyl alcohol and again with de-ionized water for 5 minutes each.

1.1.3 Remove visible water from the surface using dry nitrogen.

1.1.4 Completely remove water from the surface by placing the wafer on a hotplate at 100° for 5 minutes. Ensure that there is a sheet of aluminum foil on the hotplate as this helps in dissipation of charge build up on the wafer.

1.2 Electrode deposition

1.2.1 Place the wafer in the vacuum chamber of the sputter deposition system and pump down the chamber to 5×10^{-6} mtorr. Set the argon pressure to 2.3 mTorr and the rotation speed to 13 rpm.

NOTE: If parameters for the specific instrument being used have been established that result in high quality films, then use those instead.

1.2.2 Deposit 5–10 nm of titanium at 1.2-1.6 A/s.

NOTE: Before beginning this process with the intended wafer, test the deposition rate with the plasma power set to 200 W and depositing for 1 minute. Then measure the height of the layer with a profilometer. Do this separately for each metal. Set the power according to this test in order to achieve the stated deposition rate.

1.2.3 Deposit 1 μm of gold at 7-9 A/s.

NOTE: Deposition at a higher rate due to increased plasma power or increased argon partial pressure may reduce film quality.

1.2.4 Remove the wafer and repeat steps 1.2.1–1.2.3 for the second side of the wafer.

1.3 Dicing

1.3.1 Use a dicing saw to dice the entire wafer as needed.

NOTE: A protective resist can be applied on the substrate prior to dicing, and our system uses a UV curable film just before the samples are loaded on the dicing stage. We have found that dicing the samples with an automated dicing saw does not compromise the integrity of the samples. Hand-scribe dicing of LN is possible, though tedious and prone to inconsistencies.

2. Make electrical and mechanical contact with the transducer. We provide several methods below from which to choose. Later in the protocol we highlight which method is most appropriate for each subsequent step.

2.1 Place the transducer flat on a magnetic steel plate. Mount one pogo-probe in contact with the plate and another pogo-probe in contact with the top surface of the transducer. Hereafter this will be referred to as pogo-plate contact.

2.2 Place the transducer between two pogo-probes. Hereafter referred to as pogo-pogo contact.

2.3 Solder wire to each face of the transducer. Hereafter referred to as solder contact.

3. Resonance frequency identification via impedance analysis

3.1 Ensure that a port calibration has been performed according to the manufacturer's instructions for the specific contact method being used.

3.2 Connect a transducer to the open port of the network analyzer with one of the above contact methods.

NOTE: It can be instructive to repeat this analysis with multiple electrical contact methods and compare the results.

3.3 Select the reflection coefficient parameter, s_{11}, via the user interface and choose the frequency range of interest.

NOTE: s_{11} is the input reflection coefficient and has a minimum value at the resonance

frequency of operation. For a typical 500 μm thick 128YX LN wafer, the primary resonance frequency will be near 7 MHz and the second harmonic will be near 21 MHz, as illustrated in Fig. 1.1.

3.4 Perform the frequency sweep by selecting the option on the system display.
NOTE: The impedance plot in frequency space displayed on the instrument will exhibit local minima at the resonance frequencies.

3.5 Export the data for closer inspection using data processing software to identify the precise minima locations.

4. Vibration characterization via LDV

4.1 Place a transducer in pogo-plate contact on the LDV stage. Connect the pogo-probe leads to the signal generator. Ensure that the correct objective is selected in the PSV acquisition software and focus the microscope on the surface of the transducer.

4.2 Define the scan points by selecting the 'Define scan points' option or proceed to the following section if performing a continuous scan.

4.3 Select the 'Settings' option and under the 'General' tab, select either the 'FFT' or 'Time' option depending on whether the scan is being performed in frequency or time domain. Select the number of averages in this section.
NOTE: The number of averages affects scan time.

4.4 In the 'Channel' tab, make sure that the 'Active' boxes are checked. These correspond to the reference and reflected signal from the transducer. Adjust the reference and incident channels in order to obtain maximum signal strength from the substrate.

4.5 In the 'Generator' tab, if the measurement is carried out under single frequency signal, select "Sine" from the 'Waveform' pull down list; if it is under a band signal, select 'MultiCarrierCW'.

4.6 Change the bandwidth and FFT lines in the 'Frequency' tab to adjust the scan

resolution for a frequency domain scan. Similarly, change the 'Sample Frequency' in the 'Time' tab when performing time domain measurements.

4.7 The PSV Presentation software can be used to process and analyze the data obtained from the scan. A typical displacement spectrum is provided in Fig. 1.2.

5. Dynamics observation via high-speed imaging

6.1 Rigidly mount a high-speed camera horizontally on an optical table, place a transducer in either pogo-pogo contact or pogo-plate contact on an x-y-z stage near the focal length of the camera, and position a diffuse light source at least one focal length on the opposite side of the transducer from the camera.

6.2 For the case of pogo-pogo contact, position the fluid supply so that it does not block the camera view or the light source. Or, for the case of pogo-plate contact, apply fluid directly to the substrate with a pipette.

6.3 Adjust the camera focus and the x-y-z position to bring the fluid sample into sharp focus.

6.4 Estimate the frequency of the specific phenomenon you wish to study based on your current knowledge of the field. Choose a frame rate at least twice as large as this frequency according to the Nyquist rate in order to avoid aliasing.

NOTE: For example, we are interested in capillary waves that occur on a sessile drop at a range of frequencies. Our camera is limited in its spatial resolution, so that we can only distinguish waves with a minimum amplitude. In this case our minimum amplitude occurs around 4 kHz so we choose 8,000 fps.

6.5 Adjust the light intensity, the camera shutter, or both in order to optimize contrast between the fluid and the background.

NOTE: An opaque dye can be added to the fluid in order to increase the contrast.

6.6 Connect alligator clips from the amplified signal generator to the pogo-probes leads.

6.7 Capture video in the camera software simultaneously with actuation via the voltage signal either by manually triggering both at the same time or by connecting a trigger out-put from your signal generator to your camera.
NOTE: Typical frame rate used is 8,000 frames per second and a CF4 objective.

6.8 Save only the frames containing the phenomenon to avoid wasted storage, which is particularly relevant at large frame rates, to produce a result as shown in Fig. 1.3.
NOTE: Make sure to save the file in a format that is compatible with your image processing software of choice so that useful data can be extracted.

6. Droplet size measurement via laser scattering analysis

7.1 The laser scattering system should have a module that transmits the laser and one that receives the scattered laser signal. Position these, along the rail provided with the system, with a 20-25 cm gap between them.

7.2 Rigidly mount a platform in this gap such that, when the transducer and fluid supply assemblies are placed on it, atomized mist will be ejected into the laser beam path. This alignment is facilitated by turning on the laser beam, 'Tools' - 'Laser Control...' - 'Laser on', as a visual indicator.

7.3 Fix the transducer holder to the platform and fix the fluid supply assembly to an articulated arm (such as those made by Fisso). Position the fluid supply assembly so that the tip of the wick is just in contact with the edge of the transducer.

7.4 Create an SOP in the software by clicking the 'New SOP' icon. Configure the SOP with the following settings: template ¿ 'Default continuous', Sampling period (s) ¿ '0.1', under "Data handling" click 'Edit...' and set Spray profile ¿ Path length (mm) to '20.0', 'Alarms' ¿ uncheck 'Use default values' and set 'Min transmission (%)' to '5' and '1' and set 'Min scattering' to '50' and '10'. Leave all other settings as defaults.
NOTE: Consult the software manual that came with the instrument.

7.5 Start the measurement within the software by clicking 'Measure' - 'Start SOP' and

selecting the SOP created above and following the onscreen guidelines. Fill the fluid supply reservoir, the syringe, with water up to the desired level and note the volume. Turn on the voltage signal to begin atomizing the fluid after the measurement has started and begin a stopwatch.

7.6 The software generates a size distribution based on the scattered laser signal at the receiver due to Mie theory and a multiple scattering algorithm. Once the desired volume of fluid has been atomized, turn of the voltage signal, end the stopwatch, and record the final volume.

NOTE: The atomization flow rate can simply be calculated by dividing the volume by the time duration.

7.7 In the measurement histogram, select the portion of the data during which the atomization was occurring as expected and the signal at the receiver was strong enough to be statistically significant.

NOTE: All measurements with this technique are statistical averages and thus, if there are too few droplets, then the scattered signal will be weak and the measurement will be statistically insignificant.

7.8 Click the 'Average' icon and click 'Ok' to generate a distribution based on the selected data. Save this by selecting the window and clicking 'Edit' - 'Copy text' then pasting the result in a text file and saving with an appropriate name. This distribution data can now be used with other software, for example to create the plot in Fig. 1.4 via MATLAB.

1.2 Representative Results

We fabricated thickness mode piezoelectric devices from 128YX lithium niobate. The characterization steps for these devices include determination of the resonant frequency and harmonics using an impedance analyzer Fig. 1.1. The fundamental frequency of the devices was found to be close to 7 MHz using the technique described in this protocol, as predicted by the thickness of the

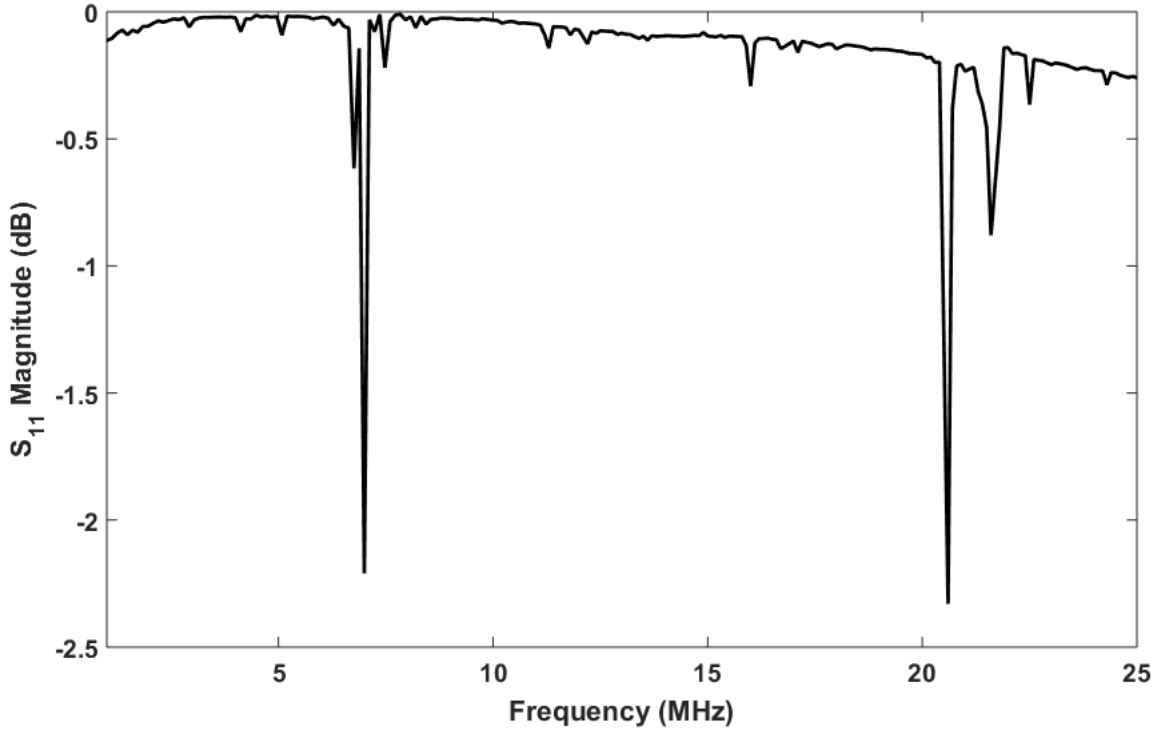

Figure 1.1: The real s_{11} scattering parameter values measured over a range of 1–25 MHz for a 127.86° YX lithium niobate device, indicating the presence of a resonance peak at approximately 7 MHz.

substrate. Further characterization of substrate vibration was performed using non-contact laser doppler vibrometer measurements. These measurements determine the magnitude of displacement of the substrate and is usually in the nm range Fig. 1.2. Continuous atomization is essential to enable practical applications of thickness mode devices, and we have demonstrated this by developing a passive fluid delivery system to the substrate. Finally, we describe two techniques to observe droplet vibration and atomization dynamics by performing high-speed imaging and by measuring droplet size distribution as shown in Fig. 1.3 and Fig. 1.4.

1.2.1 Discussion

The dimensions and aspect ratio of a transducer affects the vibration modes it produces. Because the lateral dimensions are finite, there are always lateral modes in addition to the desired

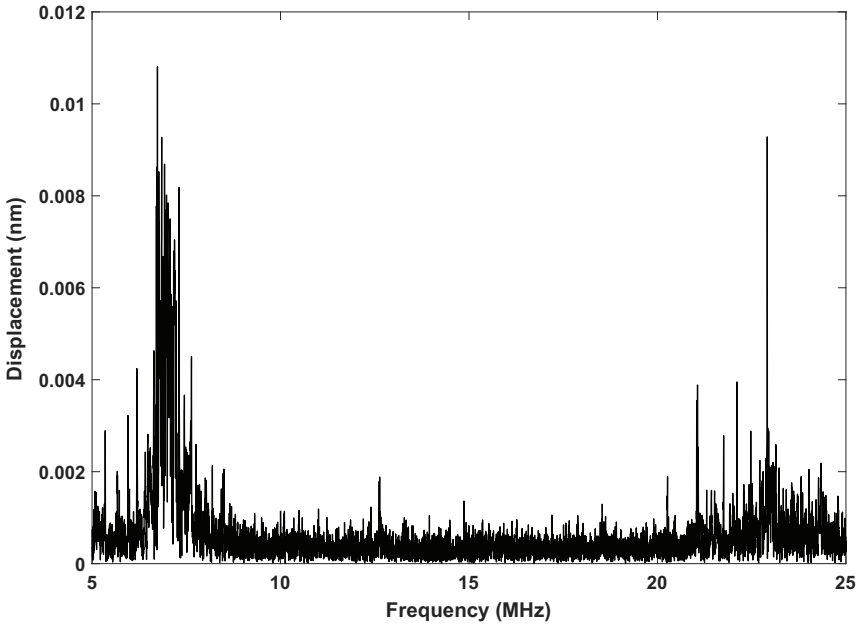

Figure 1.2: A multi-carrier, FFT scan with 5 averages at each point was performed over 9 by 9 scan points defined in a 0.6 by 0.6 mm area in the frequency range 5–25 MHz. The reported displacement is the maximum displacement averaged over all points. The fundamental thickness mode for 0.5 mm thick LN can be seen at 7 MHz, and a weaker second harmonic is present at ≈21 MHz. Notice there are multiple narrow peaks at each resonance due to interference with lateral modes. Multi-carrier scans spread the voltage input, so the displacement here is not an accurate measure of the performance of the device. For such a measurement, it is recommended to perform a single-frequency scan at the resonance frequency and with application relevant voltages. For example, this 10 by 5 mm thickness mode transducer produces a 5 nm max amplitude at 45 Vpp when driven at 6.93 MHz.

thickness modes. The above LDV methods can be used to determine dominant modes in the desired frequency range for a given transducer. We have found that a square with dimensions below 10 mm typically gives a close approximation to a thickness mode. Three by ten millimeter rectangles also work well. Supplementary videos SV1 and SV2 show LDV area scans of the square and the 3x10 transducers showing that they're close to thickness mode. These have been empirically determined rather than selected by simulation and design, though such methods could be used to find ideal lateral dimensions.

The method of electrical and mechanical contact with the transducer also affects the vibrations it produces since these are the boundary conditions to which the piezoelectric plate is subject. We

have performed an impedance spectrum for three measurement techniques - pogo-plate, pogo-pogo, and transducer holder as a comparison and confirmed the resonance peak locations are not changed in this case by our choices of contact. We do note that mechanical contact between the transducer and a plate surface dampens vibrations making atomization less efficient. We use pogo-plate contact in the case of LDV measurements, because this is the simplest way to get a flat, stationary surface on which to focus the laser.

The fluid supply assembly described here relies on capillary action and gravity to passively resupply the transducer with a thin film of water as it is atomized away. The vibration of the transducer produces a acoustowetting effect that can be enough to create a thin film and avoid flooding, but in some cases a hydrophilic treatment will be necessary on the transducer surface. If continuous atomization is not achieved, this is the most likely route to resolving the problem.

Measurements were performed with a UHF–120 from Polytec here, but other LDVs may be used. Electrical contact can be made by soldering a wire to each face of the transducer, though the solder can significantly alter the resonance frequencies and modes of the transducer. Another technique is to place the transducer on a metal base and use "pogo" spring contact probes pressed into contact on the top face of the piezoelectric transducer element while it sits flat upon the stage, useful when a large area has to be scanned. Accurate measurement of the resonance frequencies is important to efficiently operate the transducer and maximize energy throughput to mechanical motion at these frequencies. A frequency scan using the LDV provides this information, but requires a long time, on the order of tens of minutes. An impedance analyzer can determine the resonance frequencies much more quickly, often less than a minute. However, unlike the LDV, the impedance based measurement does not provide information on the vibration amplitude at the resonance frequencies, which is important in determining fluid atomization off the surface of the transducer.

Though vibration of the substrate occurs in the 10–100 MHz regime, the dynamics of fluids in contact with the substrate occur at far slower time scales. For example, capillary waves on the surface of a sessile drop are observable at 8,000 fps, assuming that the spatial resolution of the camera can distinguish the amplitude of a wave crest and that the wave frequency of interest is below 2,000 Hz. The camera arrangement described above images transmitted light and thus is

good for observing the outline of objects that transmit light differently than air. If insufficient, a reflected or fluorescent light arrangement may be required. The exposure time for each frame decreases as the frame rate is increased so the light intensity must be increased accordingly. The objective lens should be chosen based on the length scale of the phenomenon under study, but the above protocol will work with any commonly available magnification. As an example, Fig. 1.3 was obtained with the above high-speed video method. The contrast at the drop interface would allow these frames to be segmented in software (imageJ and MATLAB) so that the interface dynamics may be tracked over time.

In our droplet sizing equipment (Malvern Spraytec), the laser optics and scattering detectors are relatively standard but the software is proprietary and complex. In addition to Mie theory, multiple scattering events make droplet size and enumeration calculations much more difficult. Mie theory assumes that most photons are scattered only one time, but when droplets are densely spaced, i.e. the spacing between droplets is not much larger than the droplets themselves, and the spray plum covers a sufficiently large area, then this assumption fails[18]. As an example of troubleshooting results from this instrument, consider Fig. 1.4. Notice that the 0.5 mm diameter peak appears in both distributions. The commercial nebulizer is known to produce monodisperse droplets near 10 μm, so the larger peak is likely either a false result due to the large amount of multi-scattering events or agglomeration of smaller droplets within the spray. This implies that the large peak in the thickness mode distribution may also be a false result. This can be directly verified by high-speed video: such large droplets would be readily visible, but we do not observe them in this case.

Laser scattering particle size analysis can also be difficult when the scattering signal becomes weak. This is typically due to a low atomization rate or when part of the spray does not pass through the laser path. A weak vacuum may be used to draw the complete atomized mist through the expanded laser beam of the equipment in cases where it would otherwise escape measurement. For even greater control of spray conditions a humidity chamber can be installed around the laser beam path, but we have not found that to be absolutely necessary.

1.3 Acknowledgements

This chapter, in full, is a reprint of A. Vasan et.al. (2022) "Fabrication and Characterization of Thickness Mode Piezoelectric Devices for Atomization and Acoustofluidics." *JoVE (Journal of Visualized Experiments)* 162 (2020): e6101. The dissertation author is the first author of this article.

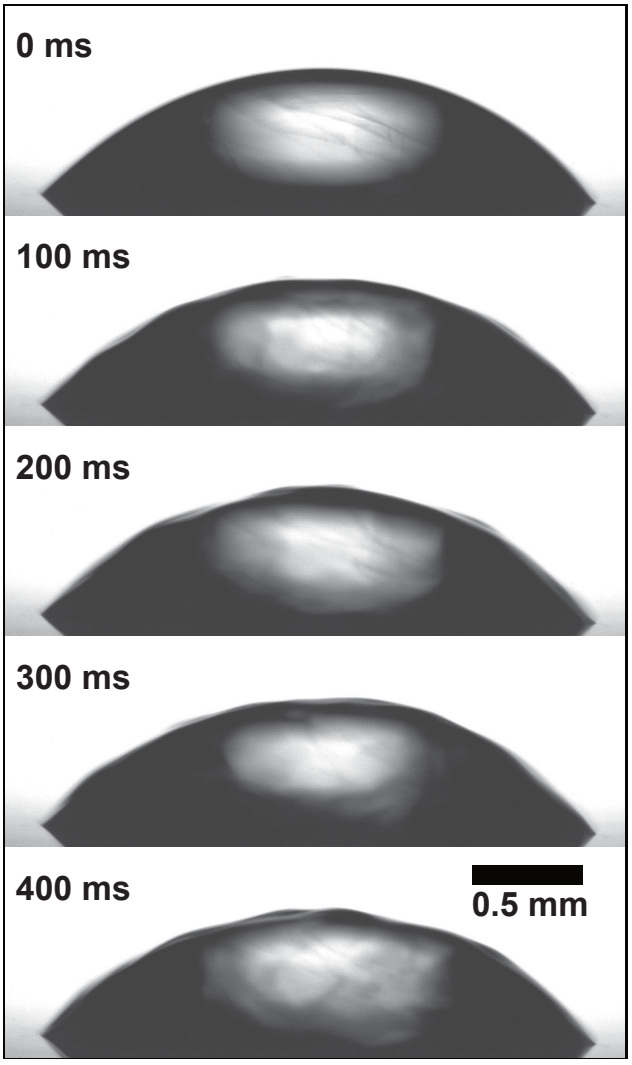

Figure 1.3: Onset of capillary waves on a 2 μL water drop is indicated by an 8000 fps video of the fluid interface; the drop is driven by a thickness mode transducer driven at 6.9 MHz, showing the significant time difference between the hydrodynamic response and the acoustic excitation.

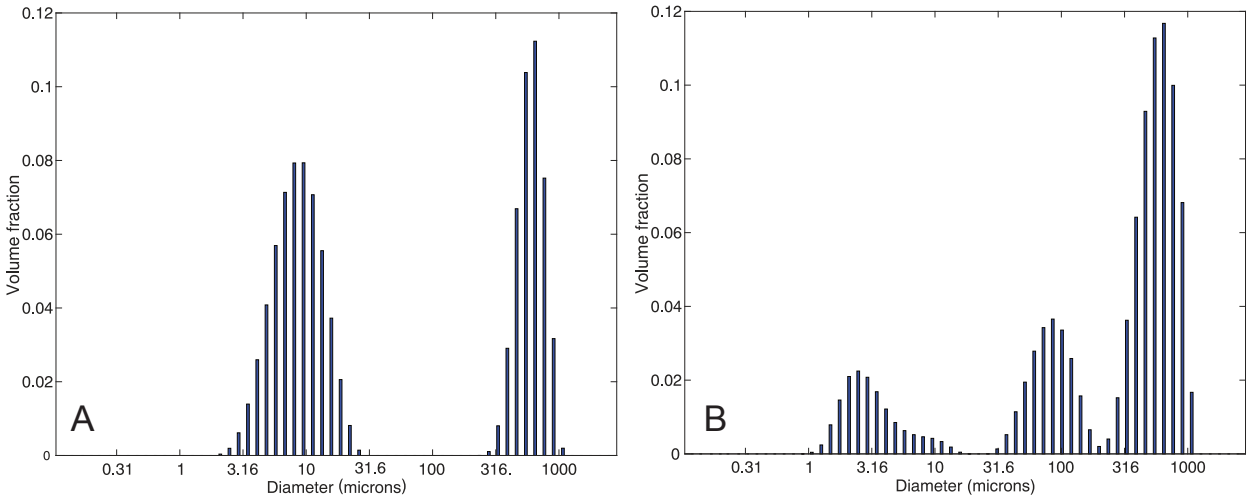

Figure 1.4: Droplet size distribution is typically measured as a volume fraction versus the droplet diameter, here comparing (A) a commercial nebulizer and (B) an LN thickness mode device, both using water.

Chapter 2

Microscale concert hall acoustics to produce uniform ultrasound stimulation for targeted sonogenetics in hsTRPA1-transfected cells

2.1 Chapter Abstract

The field of ultrasound neuromodulation has rapidly developed over the past decade, a consequence of the discovery of strain-sensitive structures in the membrane and organelles of cells extending into the brain, heart, and other organs. Notably, clinical trials are underway for treating epilepsy using focused ultrasound to elicit an organized local electrical response. A key limitation to this approach is the formation of standing waves within the skull. In standing acoustic waves, the maximum ultrasound intensity spatially varies from near zero to double the mean in one half a wavelength, and has lead to localized tissue damage and disruption of normal brain function while attempting to evoke a broader response. This phenomenon also produces a large spatial variation in the actual ultrasound exposure in tissue, leading to heterogeneous results and challenges with interpreting these effects. One approach to overcome this limitation is presented herein: transducer-mounted diffusers that result in spatiotemporally incoherent ultrasound. Herein, we numerically

and experimentally quantified the effect of a diffuser in an enclosed domain, and show that adding the diffuser leads to a two-fold increase in ultrasound responsiveness of hsTRPA1 transfected HEK cells. Furthermore, we demonstrate the diffuser allow us to produce an uniform spatial distribution of pressure in the rodent skull. Collectively, we propose that our approach leads to a means to deliver uniform ultrasound into irregular cavities for sonogenetics.

2.2 Introduction

Sound diffusers have been applied to concert hall acoustics since the 1800s, when ornamentation along the walls or concave ceilings were used to introduce greater binaural dissimilarity [19]. Evolution of concert hall architecture eventually led to the development of the Schröder diffuser, arguably the first practical technique to disperse sound in a predictable manner. In the 1970s, Schröder proposed the phase grating diffuser [19, 20], a method to artificially create diffuse reflection, with recent improvements to the design [21]. Composed of regular wells of different depths, these structures are governed by a two-dimensional (2D) pseudostochastic sequence. In the typical configuration, waves incident on this structure undergo phase shifts corresponding to the depth of the wells through which they travel. The structure then scatters sound rather than reflecting it, depending on the magnitude of these phase shifts. This method has been widely adopted in architectural acoustics, where sound absorption—the only feasible alternative—is undesirable. This method has also been applied to ultrasound imaging [22] and microparticle separation [23] where sound absorption is likewise difficult. More recently, the principle of applying phase shifts to a coherent ultrasound field has led to development of acoustic holography [24, 25]. This novel approach has enabled the generation of customized amplitude profiles based on the location and shape of the target region but has not yet been used to enable the creation of spatiotemporally incoherent fields within an enclosed cavity.

Ultrasound transducers have been used in neurological applications for imaging tissue [26], disrupting blood-brain barriers [27], invasive [28] and non-invasive neuromodulation [29], and thrombolysis [30]. In these cases, ultrasound is typically focused at a certain depth defined by a phased array of transducers [31] or an acoustic lens formed by a concave surface at the exit face of the transducer [32]. A fundamental limitation of these approaches is the formation of standing

waves due to resonant reflections within the skull cavity formed by the relatively high impedance of the skull's cortical bone compared to the tissue of the brain, and thus regions of either extremely high intensity or zero intensity at every one-half an acoustic wavelength [33]. The presence of these local maxima may lead to unintended bioeffects in tissues when applied to neuromodulation [34], including heating or even tissue damage from cavitation [35]. Such adverse effects in tissue have been reported during ultrasound-driven thrombolysis and blood brain barrier disruption [36, 37]. Additionally, commonly used transducer materials such as lead zirconate titanate (PZT) also have limitations in high power applications at frequencies above ~ 1 MHz, producing losses, hysteresis, and internal (ohmic) heating as current passes through elemental lead present at the morphological grain boundary [38], which limits the use of broadband stochastic signal generation for reducing the impact of standing wave generation. One approach to overcome these limitations is to build resonant devices using loss-free, single-crystal piezoelectric material to generate single frequency ultrasound output in the 1–10 MHz range that has an attached diffuser and is thus capable of delivering a spatiotemporally diffuse ultrasound field for various applications, including sonogenetics.

Sonogenetics relies on genetically engineering cells to be more sensitive to mechanical stimuli using membrane bound proteins [39, 40]. This technique eliminates the need for focused ultrasound by ensuring that targeted neural circuits are the only ones that will respond to an ultrasound stimulus. Recent work has revealed that one protein in particular, human transient receptor potential A1 (*hsTRPA1*), produces ultrasound-evoked responses in several cell types [40]. This response is due to deformation and consequent stretching of the cell membrane from exposure to ultrasound that, in turn, leads to a change in the membrane capacitance between a chemically-induced potential difference from inside to outside the cell. This produces a current sufficient to cause hsTRPA1 responses [41]. One limitation of sonogenetics is that existing transducers producing planar or focused ultrasound, typically at a single frequency, are unsuitable. Furthermore, in many applications, the transducer must be small to avoid affecting animal behavior, which excludes phased array based approaches. Transducers that can be attached to freely moving mice enable the study of neural circuits in their native state, without the confounding effects of anaesthesia as reported in past studies [42, 43]. Unfortunately, no small broadband transducers exist [44, 45] that might facilitate the generation of spatiotemporally random ultrasound noise from a similarly random input signal at sufficient power for sonogenetics. Moreover, commonly used animal models like rodents have

small heads with a typical mass of 3-4g [46], less than half the mass of all commercially available or research-based [47] power ultrasound transducers known to the authors.

The effective implementation of sonogenetics requires a very different transducer design. It must reduce interference between the radiated and reflected ultrasound, produce diffuse and uniform ultrasound throughout the region, transduce sufficient power to produce over 0.4 MPa acoustic pressure in tissue while remaining sufficiently small and light enough to attach to the head of a live, freely moving mouse. This would enable the study of neural circuits in their more native state, without the confounding effects of anaesthesia as reported in past studies [42, 43]. In addition, these devices also have to avoid generating electromagnetic signals and localized temperature changes. If left to appear, electromagnetic and thermal phenomena may conflate with the effects of ultrasound on the cells in sonogenetics experiments, reducing one's confidence in ultrasound's contribution to the observations.

We have overcome the limitations of existing transducers by incorporating a machined diffuser *on the transducer face* in order to produce spatiotemporally incoherent MHz-order (Fig. 2.1). Diffusers are typically used in reducing coherent reflected sound—echoes—and their use *on the sound generator itself* has not been reported to the knowledge of the authors. A diffuser is ideally suited for sonogenetics as it nearly losslessly reduces the presence of regions of either high or low intensity within an enclosed cavity, in both *in vitro* assays and within the rodent skull for longer-term applications. First, we discuss the design of the diffuser and validate its performance using numerical simulations. We then address the challenge of fabrication of a complex three-dimensional (3D) structure at sub-millimeter scales, as conventional photolithography, 3D printing, and classic machining techniques are unsuitable for this task. Next, we characterize a device which has been coupled to a lithium niobate transducer operating in the thickness mode [11]. We then present an application of the Schröder diffuser to screen for ultrasound-sensitive ion channels in human embryonic kidney (HEK293) cells *in vitro* for the purposes of identifying and isolating targets for sonogenetics in freely moving mice. Finally, we verify the presence of nearly equivalent acoustic pressures across two deep brain regions in an *ex vivo* model.

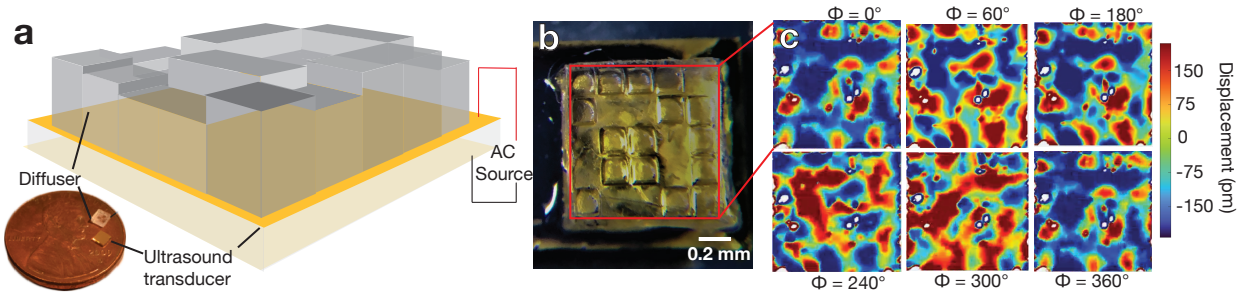

Figure 2.1: **(a)** A diffuser design based on Schröder's method of quadratic-residue sequences to determine well depth. The wells were machined in glass using a KrF excimer laser system with a custom metal mask to restrict beam width. The machined depth of the pillars are up to 309 μm. **(b)** The glass diffuser block was then **(c)** bonded to a transducer operating in the thickness mode at 7 MHz using an ultraviolet light-curable epoxy. **(c)** A scanning laser Doppler vibrometer image of the diffuser face in the time domain shows phase differences corresponding to pillar heights (normalized autocorrelation ¿ 0.73).

2.3 Results

The design of the Schröder diffuser is based on quadratic-residue sequences defined by $s_n = n^2$, where n^2 is the least non-negative remainder mod N, with N always an odd prime. One of the properties of this number sequence relevant to the design of an optimum diffuser is that both the Fourier transform of the exponential sequence $r_n = \exp(i2\pi s_n/N)$, and by extension the scattered wave produced by it, have a constant magnitude [19, 48] $|R_m|$ such that

$$|R_m|^2 = \left| \frac{1}{N} \sum_{n=1}^{N} r_n \mathrm{e}^{-\frac{2\pi\iota mn}{N}} \right|^2 = \frac{1}{N}, \tag{2.1}$$

where $\iota = \sqrt{-1}$.

We may then use this to define the wells' depths, $d(x_n, y_n)$, corresponding to the number sequence. In one dimension, the depth of the n^{th} well is given by [49]

$$L_n = \frac{\pi c n^2 \,(\mathrm{mod}\ N)}{N \omega_r}, \tag{2.2}$$

where ω_r is the design frequency, N is a prime number, and c is the speed of sound in the medium. Extending the concept of a diffuser defined per the above numerical sequence to two dimensions involves replacing n^2 in the above formula with $n^2 + m^2$, where m represents the number of wells in

the second dimension. A representative image of a diffuser fabricated using a 2D sequence is shown in Fig. 2.1.

While a one-dimensional diffuser creates a uniform 2D pressure field, a 2D diffuser with varying well depths creates a uniform 3D pressure field. Ultrasound neuromodulation typically relies on frequencies in the 1–10 MHz range [50] and this requires sub-millimeter well depths as defined by eqn. (2.2). Although structures based on the quadratic-residue sequence have been achieved at the macro-scale in two dimensions and at the microscale in one dimension [23], it has not been achieved in 2D structures on the micron to sub-mm scale due to the lack of established fabrication techniques for these dimensions [51]. Conventional photolithography is good for creating patterns that have the same depth or, at most, a few different depths. It becomes challenging when features of varying depths are desired because multiple photolithography and etching steps are required. Alternate approaches, including 3D or two-photon printing methods are unable to produce acoustically low-loss structures with sufficient dimensional accuracy at these scales. We sought to address these limitations by using an excimer laser to machine sub-millimeter pillars of varying heights in glass in two dimensions. Significant phase correlation (normalized autocorrelation ¿ 0.73) with the machined geometry is apparent from a time-domain laser Doppler vibrometry (LDV; *see* Methods) scan shown in Fig. 2.1. The transducer was driven at its resonance frequency with a sinusoidal input power range of $0.5 - 2$ W and a peak pressure output of 0.6 MPa as measured with a fiber optic hydrophone [52].

The benefit of using the diffuser was considered using finite element analysis (COMSOL 5.5, Comsol Inc., Los Angeles, CA USA). The domain was chosen to mimic an experimental setup used for identifying ultrasound-sensitive ion channels in an *in vitro* setup. This consists of an inverted fluorescence microscope with a custom perfusion chamber to house a coverslip and transducer. The simulation domain is illustrated in Fig. 2.2 and specific dimensions of the domain and simulation parameters are described in the *Methods*. The transducer and the diffuser assembly were fixed at the bottom of the domain. A custom perfusion chamber that contains a slot for a coverslip was mounted over the ultrasound source. The transducer was coupled to the coverslip through water and there was a layer of media above the coverslip. The walls were defined to be hard boundaries with the acoustic impedance $Z_{\mathrm{i}} = \infty$ such so that the normal derivative of the total acoustic pressure, $\frac{\partial p_t}{\partial n} = 0$. The diffuser consists of seventeen elements, the heights of which were calculated from

eqn. (2.2). The coverslip in serves as a solid boundary and allows the evaluation of the acoustic field in the closed domain below and the open domain above it, corresponding to the different boundary conditions assigned to the model.

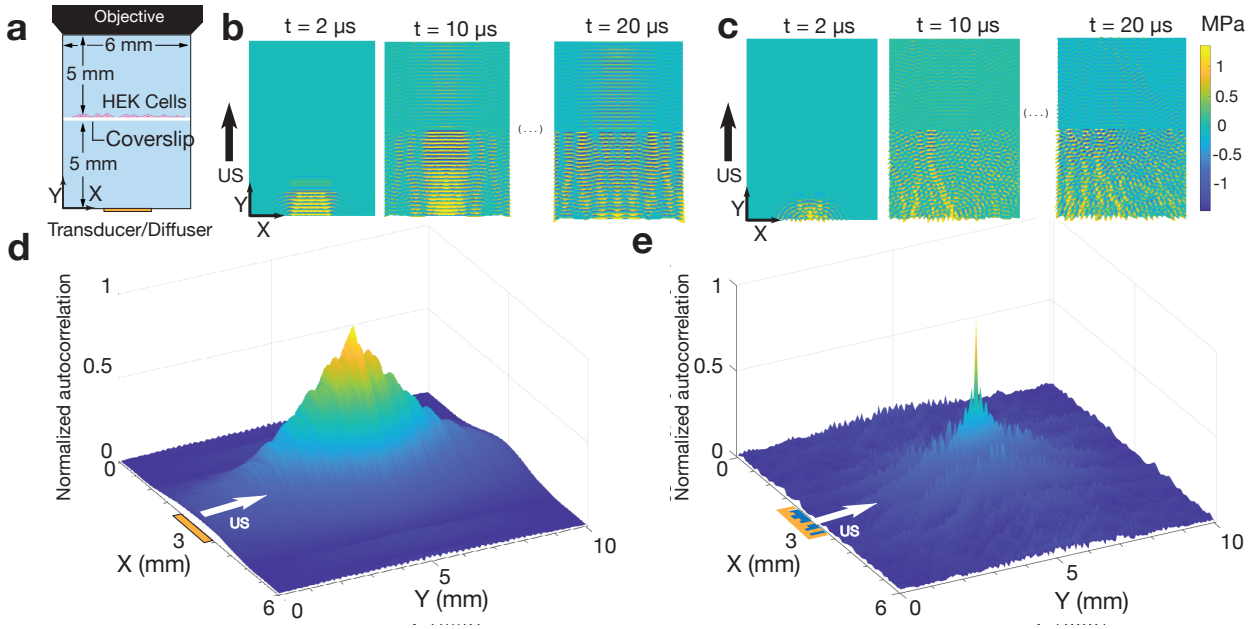

Figure 2.2: Two-dimensional instantaneous pressure profile for the **(a)** domain **(b)** without and **(c)** with the diffuser. Human embryonic kidney (HEK) cells were placed in the middle of the (light blue) fluid domain with an objective lens for an inverted microscope at top. The pressure field was generated by defining a sinusoidal pressure displacement to the transducer face, located at the bottom of the domain. Pressure maps were extracted from the results in 1μs time steps over grid points specified within the domain. A 2D autocorrelation was performed on this grid over time; each X,Y point plotted from the **(d,e)** results of the autocorrelation corresponds to a single point in the (a) domain. Spatial and temporal periodicity was observed through the existence of a large value of autocorrelation over the domain **(d)** without the diffuser. **(e)** With the diffuser, however, the autocorrelation was much smaller for most of the domain.

The time variation of the pressure field with and without the diffuser was evaluated (supplementary video S1 and S2). Several points in the fluid domain were chosen and the time evolution of the pressure field for the two cases was compared using the techniques described in the *Methods* section. A 2D autocorrelation was calculated in order to determine if there were any locations within the domain with coherence (echoes) or localized increases or decreases (constructive and destructive interference) in ultrasound intensity. Spatial and temporal patterns that form over the duration of the stimulus are represented by a 2D autocorrelation in Fig. 2.2. It is evident that there is both spatial and temporal periodicity with the transducer alone (Fig. 2.2a and supplementary

video S1) that is greatly reduced when the diffuser is introduced (Fig. 2.2b and supplementary video S2). Videos of the sample autocorrelation in the domain over the stimulus duration are presented in the supplementary information (videos S3 and S4) and show that there is greater autocorrelation over the duration of the stimulus without the diffuser (video S3). This indicates that the ultrasound field with the diffuser is temporally aperiodic.

For the purpose of quantifying any changes to the diffraction at 7 MHz through the inclusion of the diffuser, an isofrequency contour plot of the simulated data is provided in Fig. 2.3(a) without and (b) with the diffuser. Without the diffuser, wave vectors are only present in the vicinity of $k_{\mathrm{x}} = 0$, along the direction of propagation of the pressure wave in the medium: the Y axis. The angular spread is 20° on either side of the direction of propagation without the diffuser. Particularly, the majority of the wave can be seen to be propagating along the Y axis, with significant sidelobes immediately to the left and right and much smaller sidelobes slightly farther away. Including the diffuser produces wave vectors beyond the main direction of propagation (Fig. 2.3b), with significant components oriented along directions from the Y axis (along k_{x}) to the X axis (along k_{y}). The previously significant sidelobes remain significant, but are augmented by wave propagation beyond 45° in the XY plane. This indicates strong diffraction from the face of the transducer when including the diffuser. RMS pressure was calculated to determine the temporal and spatial distribution of pressure 10 μm above the coverslip as shown in Fig. 2.3(c). The inclusion of the diffuser results in a even RMS pressure distribution along the covserlip, whereas the control case shows a 5-fold variation of pressure across the coverslip face.

To verify the effects of the diffuser *in vitro*, we used an upright optical imaging setup including an immersion objective, a custom perfusion chamber, and the diffuser assembly. The diffuser assembly and the test setup are represented in Fig. 2.4a; we used lithium niobate due to its relatively high coupling coefficient and zero hysteresis [13] which implies no heating from the piezoelectric material itself. Human embryonic kidney (HEK293) cells expressing GCaMP6f [53] were transfected with hsTRPA1. We compared fluorescence changes ($\frac{\Delta F}{F}$) for four cases, with and without the channel, without the diffuser assembly (transducer alone), and with the diffuser assembly. Representative GCaMP6f images of HEK293 cells transfected with hsTRPA1 are shown in Fig. 2.4b and heat maps of fluorescence intensity with respect to time are presented in Fig. 2.4c, with a clear increase in both the magnitude and number of cells being activated with the diffuser

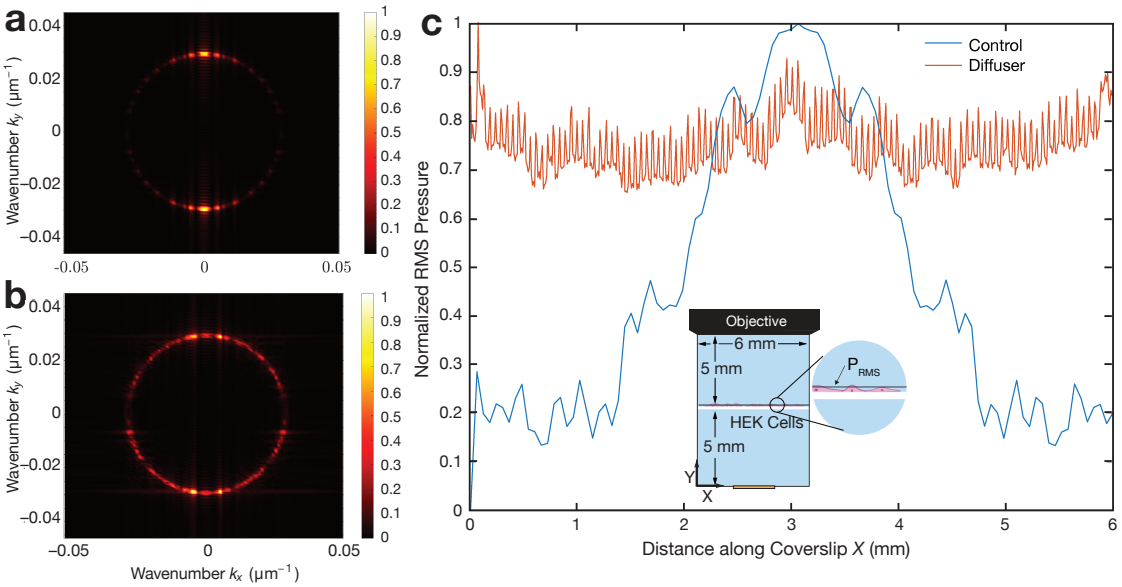

Figure 2.3: Calculated isofrequency contour at the driving frequency **(a)** without and **(b)** with the diffuser. The circular profile traced by both cases corresponds to the wave vector in water at the driving frequency. (a) Without the diffuser, most of the wave is isolated to propagation along the Y axis. Using (b) a diffuser with the transducer produced wave vectors spread around this circular profile, indicating a more uniform distribution of the ultrasound. Calculating (c) the normalized root mean square (RMS) pressure 10 μm above the coverslip (inset; halfway between the transducer and objective lens) indicates a smaller difference between minimum and maximum RMS values (red) with the diffuser than (blue) without it. The diffuser produces a much more uniform pressure distribution across the coverslip plane.

assembly. Cells expressing hsTRPA1 and controls were tested at two different pressures, 0.32 MPa and 0.65 MPa. There was a consistent increase in fluorescence intensity with an increase in acoustic pressure for both the control and the hsTRPA1 condition, whether or not the diffuser was present. Including the diffuser increased the mean fluorescence amplitude by at least a factor of two for cells that had been infected with hsTRPA1 ($p < 0.0001$, Fig. 2.4d).

We also tested the effects of ultrasound on mouse primary cortical neurons. Neurons were infected with adeno-associated viral (AAV) vectors to express hsTRPA1 and a genetically encoded calcium indicator, GCaMP6f [53], or a control with only the calcium indicator. We found that ultrasound triggered an increase in calcium uptake in both cases, with the hsTRPA1 neurons showing a greater number of activated cells in comparison to the control (Fig. S2). A video of real-time calcium response in hsTRPA1-expressing neurons is presented in the supplementary information (Video S5).

The uniform nature of the ultrasound field created by the diffuser was also verified *ex vivo* in a mouse skull, while keeping as much of the mouse skull intact during preparation as possible *see Methods*. Pressure measurements were taken at two different locations as indicated in Fig. 2.5 along the anterior-posterior axis, at the ventral surface of the pons and the ventral surface of the anterior olfactory bulb. With the diffuser, the pressure at both these locations was uniform, with minimal deviation between them and a uniform increase with input power to the transducer (Fig. 2.5). However, the transducer alone produced diverging values of pressure at these positions, so much so that the pressure at the pons (triangle) exceeded the pressure at the anterior olfactory bulb (circle) by a factor of 3 at an input power of 3 W, yet fell below the hydrophone's minimum measurement value, 0.2 MPa, at the anterior olfactory bulb when using less than 1.25 W of power. By contrast, the diffuser had minimal deviation in pressure values at these locations, with pressure values ranging from 0.25 - 0.5 MPa at the ventral surface of both the pons and the anterior olfactory bulb. These brain regions were chosen not for their function, but because they were remote and would therefore be expected to exhibit standing-wave behavior with large variations in the acoustic pressure. Collectively, these results demonstrate that the diffuser is capable of delivering uniform ultrasound fields *in vivo* in comparison to the a transducer alone, thus enabling sonogenetic studies across large brain regions.

2.4 Discussion

Existing non- and minimally-invasive techniques to stimulate brain regions, such as transcranial magnetic stimulation and transcranial direct current stimulation, offer poor spatial resolution. This is a problem for precisely targeting brain regions that have specific functions. Ultrasound-based stimulation enables targeting brain regions with sub-millimeter-scale accuracy. This precision can be achieved in different ways, either by using an array to focus ultrasound to a specific region [54] or by using sonogenetics to engineer cells to locally be more sensitive to mechanical stimuli. The development of sonogenetics that started with the *TRP4* channel has expanded to include a library of proteins that are sensitive to ultrasound stimuli at different ultrasound stimulation parameters. Examples include MSC [55], TREK [56], Piezo [57], and other TRP channels [**?**], all have which have been shown to be sensitive to ultrasound *in vitro*.

Still, a limitation with focused ultrasound is the alteration in the position and shape of the focal zone due to spatial variations in acoustic impedance [58]. Sonogenetics is an attractive option because of the potential of having a toolkit of specific proteins that can be engineered to be sensitive to ultrasound stimuli at different frequencies or pressures. Current ultrasound transducers and how ultrasound interacts with the skull cavity are important limitations to translate sonogenetics into clinical practice. Standing waves in the skull cavity produce nodes and antinodes, each separated by one-half of the acoustic wavelength and responsible for pressure minima and maxima, respectively. This may lead to haemorrhage and heating in tissue [36] in past studies. One could attempt to overcome this issue by using broadband white noise to produce a spatiotemporally random acoustic field, but ultrasonic transducers are unable to provide such noise at pressures sufficient to elicit cellular responses.

Designed via computational analysis and fabricated with an excimer laser, a microscale Schröder diffuser was devised to eliminate the spatiotemporally heterogeneous distribution of ultrasound by placing it upon the emitting transducer. The transducer alone was shown to produce standing waves in the absence of the diffuser. With the diffuser in place, autocorrelation of the ultrasound field quantifies the elimination of the standing waves and consequent suppression of antinodes associated with potential tissue damage. We verified the predictions of the simulation *in vitro* using HEK293 cells and neurons that were transfected with a sonogenetic candidate, hsTRPA1.

Development of sonogenetics in larger animal models—such as primates—will require ultrasound transducers that are capable of delivering an acoustic field that is spatially and temporally incoherent, as we have shown with the diffuser assembly. This ensures that the pressure in different brain regions is uniform over the stimulus duration, thus eliminating the aberrations in the acoustic field due to the skull cavity. Functionalization of specific brain regions using ultrasound-sensitive proteins can offer sub-millimeter spatial precision. Localization of Sonogenetic proteins in combination with an acoustic field provided by a diffuser assembly will also ensure that the observed neuromodulatory effects are solely due to ultrasound activation of targeted regions of tissue and not due to the confounding effects of reflection or interference from the geometry of the skull.

2.5 Methods

Ultrasound transducers

Ultrasound transducers used in this study were single crystal lithium niobate transducers operating in the thickness mode with lateral dimensions of 5x5 mm and thickness 500 μm. The 128YX cut of lithium niobate was used and the fabrication process involved cleaning of the wafer with acetone, isopropyl alcohol, and ultra-pure deionized (DI) water followed by sputtering both sides with an adhesion layer of 20 nm titanium followed by 1 μm gold. The deposition parameters were (with a Denton Discovery 635, Denton Vacuum LLC, New Jersey, USA) $5-10$ nm of Ti at $1.2-1.6$ A/s with the power set to 200 W, with argon as the gas in the chamber at 2.3 mT and the stage rotating at 13 RPM to ensure uniform deposition over the sample. The thickness of gold deposited was 1 μm at a rate of $7-9$ A/s.

Diffuser fabrication and characterization

Code (MATLAB, Mathworks, Massachusetts, USA) was used to define the well depths based on the medium of choice and was used to define a computer-aided design program that controlled the operation of a laser system. The excimer machining laser used for this application was a 6 mJ, 200 Hz, 248 nm (Lasershot, Optec Inc., San Diego, CA USA and Frameries, Belgium) KrF laser machining system. A grid was defined using the method of quadratic residues described above and the well depth was calculated for each increment along the X and Y directions. The parameters needed for determining well depth are the speed of sound in glass, $c = 4550$ m/s, and the operating frequency of the transducer, $\omega_r = 2\pi f$ where f in this case is 7 MHz, corresponding to the fundamental frequency for 500 μm thick 128YX lithium niobate [13]. The well depth ranged up to $309\,\mu$m and required between three and ten laser machining passes. The machined diffuser was bonded to the transducer face using a UV-curable epoxy (NOA81, Norland Products Inc, Cranbury, NJ USA) using previously described techniques [59]. This fabrication technique enables the miniaturization of devices that are capable of producing diffuse acoustic fields irrespective of the nature of the enclosed volume, as determined using surface and domain measurements as follows. A scanning laser Doppler vibrometer (UHF-120SV, Polytec, Waldbronn, Germany) was used to characterize the displacement of the substrate when actuated. Measurements of the pressure output

from the transducer were performed using a fiber optic hydrophone (FOHS92, Precision Acoustics, Dorchester, UK).

Ultrasound field simulation

Finite element analysis (COMSOL 5.5, Comsol Inc., Los Angeles, CA USA) was used to simulate the system as a linear media with a time-dependent acoustic pressure field present in two dimensions. The boundaries between the coupling fluid and the cover slip, and the cover slip and the media above it were defined as acoustic-structure boundaries, where there is fluid load on the structure due to pressure waves originating from the ultrasound source and structural acceleration on the fluid domain across the fluid-solid boundary. This results in stress build-up in the cover slip that is translated to the fluid domain above it for the duration of the stimulation. The coverslip was defined to have the elastic properties of silica glass, with an isotropic Young's modulus of 73.1 GPa, a density of 2203 kg/m^3 and a Poisson's ratio of 0.17. The distance between the transducer and the upper boundary is 5 mm. The simulations were conducted in the time domain, with a 20 μs burst followed by an 30 μs dwell to observe changes in the pressure field both during and after the stimulus. The acoustic field was modeled as a sinusoidal input to the transducer, $d = 5\sin(\omega t)$ nm, and the fluid domain was defined to have the properties of water ($\rho = 1000$ kg/m^3, $c = 1500$ m/s). The maximum mesh size was chosen so that all element sizes were always less than one-eighth of a wavelength, and the data were exported every 0.05 μs so that a frequency range of up to 10 MHz could be analyzed. The cover slip was defined to be 500 μm thick and spanned the entire width of the domain. The spatial step chosen for plotting the isofrequency contours was less then $k_{\max} = \omega c^{-1}$.

Imaging rig for ultrasound stimulation

An upright epi-fluorescent microscope (Imager M2, Carl Zeiss GmbH, Gottingen, Germany) was used for the *in vitro* experiments. For this application we used our transducer assembly placed in a heated stage fixture set to 37°C underneath the cell chamber, which ensures homeostatis. Stimulus frequency and duration was controlled by a waveform generator (33600A Series, Keysight, CA USA), and the pressure was controlled through a 300-W amplifier (VTC2057574, Vox Technologies, Richardson, TX USA). Simultaneous calcium imaging was performed using a 40x water dipping

objective at 16.6 frames per second with a camera (Orca Flash 4.0, Hamamatsu Photonics K.K., Japan) and a GFP filter.

HEK293 cell culture and transfection

HEK293 cells (ATCC CRL-1573) were cultured using a standard procedure in DMEM supplemented with 10% fetal bovine serum (FBS) and 20 mM glutamine in a 37°C and 5% CO_2 incubator. Cells beyond passage thirty were discarded and a new aliquot was thawed. A stable calcium reporter line was generated with a GCaMP6f lentivirus (Cellomics Technology PLV-10181-50) followed by fluorescence-activated cell sorting (FACS). For diffuser experiments, GCaMP6f-expressing HEK cells were seeded on a twelve-well cell culture plates with 18-mm glass coverslips coated with poly-D-lysine (PDL) (10 μg/μl; P6407, Sigma-Aldrich, St. Louis, Missouri, USA) for 1-2h. Coverslips were washed with (Milli-Q) ultrapure water and cells were seeded at a density of 250000 cells/well. Cells were transfected with lipofectamine LTX Reagent (15338100, ThermoFisher Scientific, Massachusetts, USA) according to the manufacturer's protocol and 24 hours after plating, using 500 ng DNA of the clone of interest for each well. Cells were kept at 37°C for an additional 24 h before imaging on our ultrasound stimulation setup. For imaging, cover slips were mounted on a specialized chamber featuring an ultrasound transducer approximately 5 mm below the cover slip and a 10 mL reservoir of media above the cover slip. Once cells were in focus, an ultrasound pulse of 100 ms duration was delivered as described in previous sections while imaging with a 40X immersion objective, and a cell membrane profile was reconstructed and analyzed from these images (ImageJ, National Institutes of Health, Bethesda, Maryland, USA).

Calcium imaging

Calcium imaging analysis was performed using custom scripts written as ImageJ macros. Transfected cells were segmented and cell fluorescence over time in the GCaMP6f channel was measured and stored in comma-delimited text (csv) files. Calcium data was analyzed using custom Python scripts. Calcium signals were normalized as Δ F/F using a 6 s baseline for each region of interest (ROI) and a peak detection algorithm with a fixed threshold of 0.25 was used to identify responsive cells after ultrasound stimulation.

Ex-vivo hydrophone measurements in murine model and animal safety considerations

Hydrophone measurements were performed with a fiber-optic hydrophone (FOHS92, Precision Acoustics, Dorchester, UK) *ex vivo*. C57BL/6 mice (JAX 000664), aged 10–14 weeks, were sacrificed and decapitated. The skin over the skull was removed, followed by removal of the lower mandible, soft palate, and hard palate. Once the ventral part of the brain was exposed, the mouse head preparation was placed dorsal side down on the diffuser assembly coupled with ultrasound gel, and the hydrophone tip was lowered into the ventral portion of the brain using a micromanipulator (Fig. S3).

This study was performed using one adult mouse, conforming to ARRIVE guidelines 2.0 (National Centre for the Replacement, Refinement & Reduction of Animals in Research). The work was conducted by A. Vasan and U. Magaram in the Salk Institute in La Jolla, CA. A. Vasan was present for all procedures. No control mice were used. The mouse was randomly and blindly selected from twenty healthy mice. No exclusions were made. Animals used in this trial were group housed in an American Association for the Accreditation of Laboratory Animal Care approved vivarium on a 12 hour light/dark cycle, and all protocols were approved by the Institutional Animal Care and Use Committee of the Salk Institute for Biological Studies (protocol # 15–00064). Food and water were provided ad libitum, and nesting material was provided as enrichment. The mouse was euthanized using CO_2 according to approved protocols before decapitation and dissection for the hydrophone measurements.

A murine model was selected for this study for the following reasons:

- Mice to be used in this study represent a published model for sonogenetics.
- From an anatomical and physiological perspective, the mouse brain is an acceptable approximation of the human brain. This is important because the test system that is being used in this study is one that may find its way into human use in the future.
- Historically, the mouse has proved to be an excellent model for neurological evaluations and therapy in humans.
- The experience of the laboratory with this model produces better judgment concerning

model-related complications.

- Artificial (*in silico*) and computational models are inadequate to represent the complexity of the neurological system in mice (and humans) in understanding sonogenetics.
- Smaller animals lack the scale and complexity of the surrounding skull necessary for sufficient evaluation of the technology considered in this study.

2.6 Acknowledgements

This chapter, in full, is a reprint of A. Vasan et.al. (2022) "Microscale concert hall acoustics to produce uniform ultrasound stimulation for targeted sonogenetics in hsTRPA1-transfected cells." *Advanced NanoBioMed Research* 2.5 (2022): 2100135. The dissertation author is the first author of this article.

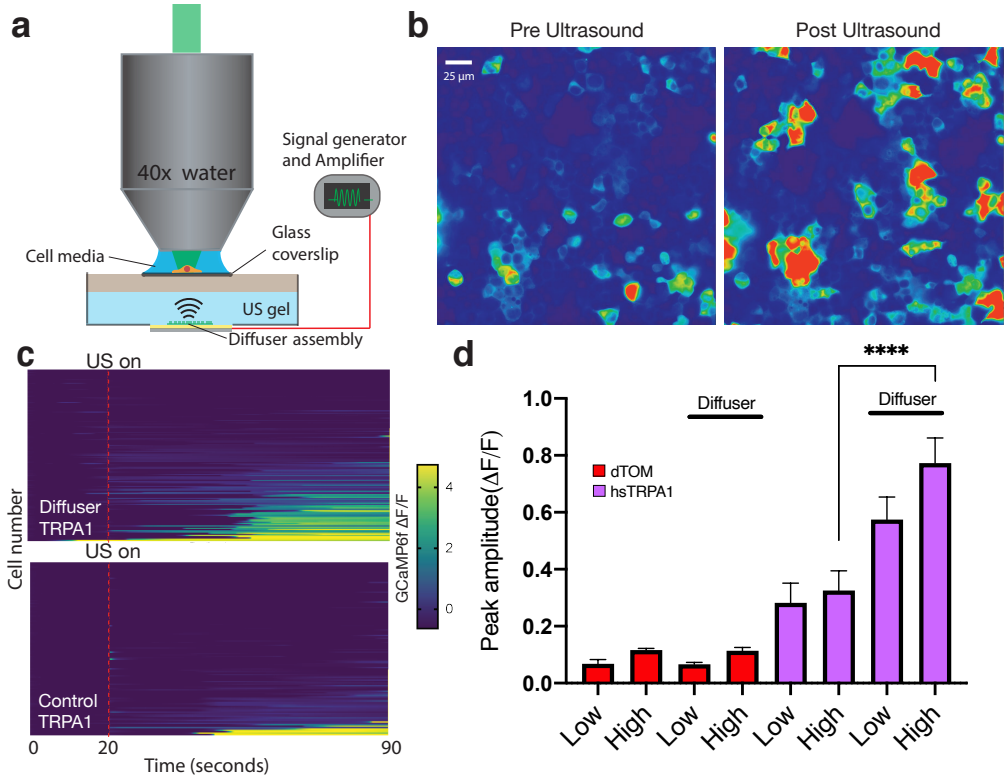

Figure 2.4: **(a)** The experimental setup for confirming the utility of the diffuser in an *in vitro* setting consists of a upright epi-fluorescent microscope, an immersion objective, and a chamber that houses cells on a coverslip and the diffuser assembly. Standing wave components may exist between the transducer and the cover slip and between the cover slip and the immersion objective. The calcium concentration before and after ultrasound stimulation in the same field of view is **(b)** shown for HEK cells expressing hsTRPA1. Comparison of fluorescence changes as measured using GCaMP6f reporters with respect to time for two cases, **(c)** without (control) and with the diffuser show an increase in both number and magnitude of cells being activated upon introduction of the diffuser. **(d)** HEK cells expressing TRPA1 show a greater response to ultrasound stimuli with a diffuser present in comparison to both no diffuser and dTom-based controls. The magnitude of the response when the diffuser is used is significantly greater (over twice as high) than when the diffuser is not used ($n = 76 - 221$, $^{****}p < 0.0001$ by a Mann-Whitney test).

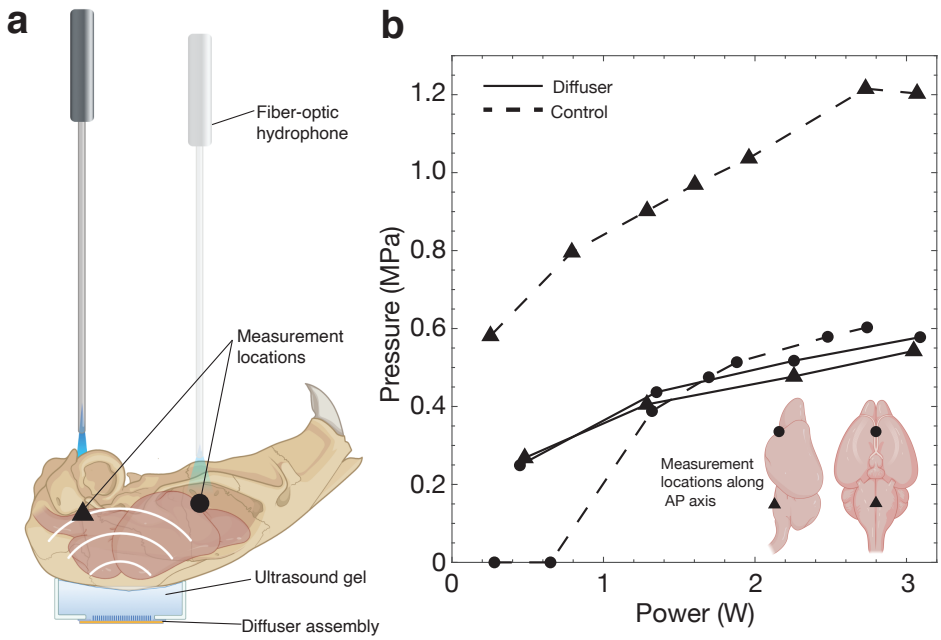

Figure 2.5: The pressure was measured using **(a)** a fiber optic hydrophone at two different locations along the anterior-posterior axis: the ventral surface of the pons (triangle) and the ventral surface of the anterior olfactory bulb (circle). The measured pressure is **(b)** uniform across different brain regions for different input powers above 0.2 MPa (minimum detectable pressure using our setup), indicating that the diffuser creates a uniform acoustic field within the skull cavity. This eliminates the influence of the cranial structure and ensures that only the brain regions that have been infected with hsTRPA1 will be sensitive to ultrasound stimuli. In comparison, the control case without the diffuser shows a three-fold deviation in pressure values for the same input power for different brain regions along the AP axis.

Chapter 3

Ultrasound mediated cellular deflection results in cellular depolarization

3.1 Chapter Abstract

Ultrasound has been used to manipulate cells in both humans and animal models. While intramembrane cavitation and lipid clustering have been suggested as likely mechanisms, they lack experimental evidence. Here we use high-speed digital holographic microscopy (kHz order) to visualize the cellular membrane dynamics. We show that neuronal and fibroblast membranes deflect about 150 nm upon ultrasound stimulation. Next, we develop a biomechanical model that predicts changes in membrane voltage after ultrasound exposure. Finally, we validate our model predictions using whole-cell patch clamp electrophysiology on primary neurons. Collectively, we show that ultrasound stimulation directly defects the neuronal membrane leading to a change in membrane voltage and subsequent depolarization. Our model is consistent with existing data and provides a mechanism for both ultrasound-evoked neurostimulation and sonogenetic control.

3.2 Introduction

Existing methods to stimulate neural activity include electrical [60–64], optical [65] and chemical techniques [66]. They have enabled the development of novel therapies that are used in clinical settings [67], in addition to helping understand aspects of neural function [68] and disease mechanisms [69]. Despite their beneficial impact, these approaches are fundamentally limited. Electrical stimulation is invasive, requiring direct contact with the target of interest. Inserting electrodes into the brain may lead to inflammation, bleeding, cell death [70], and local cytokine concentration increases in microglia that precipitate astrocyte formation around the electrodes that, in turn, reduce long-term effectiveness [71]. In addition, it may have non-specific effects depending on the electric field generated by the electrodes and the stimulation parameters used [72]. Transcranial direct current stimulation (tDCS) and transcranial magnetic stimulation (tMS) are new and non-invasive, yet they have poor spatial resolution on the order of 1 cm [73, 74]. Furthermore, approaches combining genetic tools with light or small molecules achieve cellular specificity. *Optogenetics*, which involves the use of light and genetically encoded membrane proteins [75], has enabled elucidation of cellular circuits in animal models. However, it remains an invasive technique and applications are limited by the depth of penetration of light in tissue. By contrast, *chemogenetics*, using small molecule sensitive designer receptors, is limited by poor temporal resolution and is unfortunately impractical for many neural applications that require millisecond response times [76].

Ultrasound can overcome the limitations of these methods. It is non-invasive and has a high spatiotemporal resolution ($<$ 1 mm and $<$ 1 ms) in comparison to existing techniques. Improvements in the spatial resolution through transfection of mechanosensitive proteins currently come at the cost of a minimally-invasive procedure to directly inject the vector into the target tissue [40], though there may soon be non-invasive alternatives [77]. The spatial resolution of ultrasound is governed by the wavelength of operation and is about 1.5 mm at 1 MHz in tissue. The temporal resolution is dependent on the pulse duration of stimulation and may be as short as a single time period, $T = 1/f$ where f is the operating frequency. The frequency choice is dictated by the depth and size of the target region in traditional focused ultrasound neuromodulation [78]. Harvey [79] was one of the first to utilize these advantages over ninety years ago on frog ventricular heart tissue. Recent advances in describing the suppression of epileptic activity in patients [80] are an indicator

the method is still being considered in clinical applications.

Despite these recent experimental and clinical developments, and progress in exploring the sonogenetic and ultrasonic-to-chemical action mechanisms, there is no convincing, overarching explanation for the observations reported *in vitro* or *in vivo*. Some of the proposed mechanisms include cavitation [81], indirect auditory signalling *in vivo* [82] and increased lipid clustering resulting in a change in the membrane tension [83]. These studies have either been conducted on time scales that are orders of magnitude larger than those used for ultrasound neuromodulation, lack robust imaging techniques that operate at timescales relevant to the frequency of stimulation, or use incorrect stimulation thresholds that are orders of magnitude lower than values reported in experimental work [84]. Additionally, studies often treat surface tension, membrane composition, and membrane stresses as a single term, *membrane fluidity* [83]. This term lacks rigorous physical description and is assigned a value based on relative fluorescence intensity changes. The imprecision of this description makes it difficult to isolate the influence of the measurable physical mechanisms of which it is comprised. A model using membrane fluidity leaves the explanation of the biophysical phenomenon incomplete.

More broadly, action potentials are known to appear in phase with the cell membrane's deflection [85, 86]. Pivotal work by Lee et al. [87] investigated neuronal displacement using high-pressure ultrasound sufficient to induce cavitation believed to be responsible for the observed effects. However, Lee et al. [87] acknowledged that it may not play a role in neuromodulation, contrary to models put forth in the past [81]. Instead, Lee et al. postulate that neuromodulatory effects *may* be driven by acoustic radiation forces[1], hinting at the results we later demonstrate in this paper. These and more recent studies into the thermodynamic effects associated with the generation of action potentials [88] point to transmembrane voltage changes being more than just an electrical phenomenon, they are possibly influenced by physical motion of the membrane and its components.

All that noted, a key limitation in validating existing models is the inability to measure physical motion across the vast differences in spatiotemporal scales. The ultrasound signal is on the order of 1 MHz and is three orders of magnitude faster than the electrical response of a cell. The wavelength of ultrasound in tissue at these frequencies is orders of magnitude larger than the membrane thickness. Existing methods to measure cell deflection include contact-based atomic

[1] *See* the Limitations section in their paper.

force microscopy (AFM) [89, 90], which has high spatial resolution but poor temporal resolution and lacks the ability to simultaneously scan multiple points [91]. Optical tweezers have been used for over twenty years, but only produce results from slow to static deformation of cells and often require attachment of beads or other structures that reduce the measurement to just a few spatial points [92]. Traditional digital holographic imaging [93] is slow but offers high spatial resolution across a large field of view.

We employ high-speed digital holographic microscopy (DHM), a unique method established in our group and reported for the first time here. It provides much higher resolution in both space and time than previous methods, and is therefore better suited to the study of dynamics of the cell membrane due to ultrasound. To illustrate this, we provide the first three-dimensional visualization of cell membrane deflection due to an ultrasound stimulus using the high-speed DHM. We use current clamp electrophysiology in the challenging environment of intense ultrasound to monitor ultrasound-driven, real-time changes in voltage across the membrane in single neurons *in vitro*. Furthermore, we have devised an analytical model to predict neuronal depolarization driven by membrane deflection from applied ultrasound stimulus. The experimental results confirm the predictions made by the biophysical model, both with regard to membrane deflection and voltage changes. These findings provide insight into the effects of ultrasound on cells and cell signaling, the understanding of which is vital to sonogenetics and its clinical application. Existing methods to stimulate neural activity include electrical [60–64], optical [65] and chemical techniques [66]. They have enabled the development of novel therapies that are used in clinical settings [67], in addition to helping understand aspects of neural function [68] and disease mechanisms [69]. Despite their beneficial impact, these approaches are fundamentally limited. Electrical stimulation is invasive, requiring direct contact with the target of interest. Inserting electrodes into the brain may lead to inflammation, bleeding, cell death [70], and local cytokine concentration increases in microglia that precipitate astrocyte formation around the electrodes that, in turn, reduce long-term effectiveness [71]. In addition, it may have non-specific effects depending on the electric field generated by the electrodes and the stimulation parameters used [72]. Transcranial direct current stimulation (tDCS) and transcranial magnetic stimulation (tMS) are new and non-invasive, yet they have poor spatial resolution on the order of 1 cm [73, 74]. Furthermore, approaches combining genetic tools with light or small molecules achieve cellular specificity. *Optogenetics*, which involves the use of light and

genetically encoded membrane proteins [75], has enabled elucidation of cellular circuits in animal models. However, it remains an invasive technique and applications are limited by the depth of penetration of light in tissue. By contrast, *chemogenetics*, using small molecule sensitive designer receptors, is limited by poor temporal resolution and is unfortunately impractical for many neural applications that require millisecond response times [76].

Ultrasound can overcome the limitations of these methods. It is non-invasive and has a high spatiotemporal resolution (¡ 1 mm and ¡ 1 ms) in comparison to existing techniques. Improvements in the spatial resolution through transfection of mechanosensitive proteins currently come at the cost of a minimally-invasive procedure to directly inject the vector into the target tissue [40], though there may soon be non-invasive alternatives [77]. The spatial resolution of ultrasound is governed by the wavelength of operation and is about 1.5 mm at 1 MHz in tissue. The temporal resolution is dependent on the pulse duration of stimulation and may be as short as a single time period, $T = 1/f$ where f is the operating frequency. The frequency choice is dictated by the depth and size of the target region in traditional focused ultrasound neuromodulation [78]. Harvey [79] was one of the first to utilize these advantages over ninety years ago on frog ventricular heart tissue. Recent advances in describing the suppression of epileptic activity in patients [80] are an indicator the method is still being considered in clinical applications.

Despite these recent experimental and clinical developments, and progress in exploring the sonogenetic and ultrasonic-to-chemical action mechanisms, there is no convincing, overarching explanation for the observations reported *in vitro* or *in vivo*. Some of the proposed mechanisms include cavitation [81], indirect auditory signalling *in vivo* [82] and increased lipid clustering resulting in a change in the membrane tension [83]. These studies have either been conducted on time scales that are orders of magnitude larger than those used for ultrasound neuromodulation, lack robust imaging techniques that operate at timescales relevant to the frequency of stimulation, or use incorrect stimulation thresholds that are orders of magnitude lower than values reported in experimental work [84]. Additionally, studies often treat surface tension, membrane composition, and membrane stresses as a single term, *membrane fluidity* [83]. This term lacks rigorous physical description and is assigned a value based on relative fluorescence intensity changes. The imprecision of this description makes it difficult to isolate the influence of the measurable physical mechanisms of which it is comprised. A model using membrane fluidity leaves the explanation of the biophysical

phenomenon incomplete.

More broadly, action potentials are known to appear in phase with the cell membrane's deflection [85, 86]. Pivotal work by Lee et al. [87] investigated neuronal displacement using high-pressure ultrasound sufficient to induce cavitation believed to be responsible for the observed effects. However, Lee et al. [87] acknowledged that it may not play a role in neuromodulation, contrary to models put forth in the past [81]. Instead, Lee et al. postulate that neuromodulatory effects *may* be driven by acoustic radiation forces[2], hinting at the results we later demonstrate in this paper. These and more recent studies into the thermodynamic effects associated with the generation of action potentials [88] point to transmembrane voltage changes being more than just an electrical phenomenon, they are possibly influenced by physical motion of the membrane and its components.

All that noted, a key limitation in validating existing models is the inability to measure physical motion across the vast differences in spatiotemporal scales. The ultrasound signal is on the order of 1 MHz and is three orders of magnitude faster than the electrical response of a cell. The wavelength of ultrasound in tissue at these frequencies is orders of magnitude larger than the membrane thickness. Existing methods to measure cell deflection include contact-based atomic force microscopy (AFM) [89, 90], which has high spatial resolution but poor temporal resolution and lacks the ability to simultaneously scan multiple points [91]. Optical tweezers have been used for over twenty years, but only produce results from slow to static deformation of cells and often require attachment of beads or other structures that reduce the measurement to just a few spatial points [92]. Traditional digital holographic imaging [93] is slow but offers high spatial resolution across a large field of view.

We employ high-speed digital holographic microscopy (DHM), a unique method established in our group and reported for the first time here. It provides much higher resolution in both space and time than previous methods, and is therefore better suited to the study of dynamics of the cell membrane due to ultrasound. To illustrate this, we provide the first three-dimensional visualization of cell membrane deflection due to an ultrasound stimulus using the high-speed DHM. We use current clamp electrophysiology in the challenging environment of intense ultrasound to monitor ultrasound-driven, real-time changes in voltage across the membrane in single neurons *in vitro*. Furthermore, we have devised an analytical model to predict neuronal depolarization driven

[2] *See* the Limitations section in their paper.

by membrane deflection from applied ultrasound stimulus. The experimental results confirm the predictions made by the biophysical model, both with regard to membrane deflection and voltage changes. These findings provide insight into the effects of ultrasound on cells and cell signaling, the understanding of which is vital to sonogenetics and its clinical application.

3.3 Results

3.3.1 Digital holographic imaging of cell membrane deflection

High resolution imaging approaches employing phase-contrast [94] and differential contrast [95] are commonly used to image biological specimens. These techniques transform phase differences to amplitude differences in an image, but they lack quantitative phase information. High-speed digital holographic microscopy (DHM) [96] is a cutting-edge method that produces three-dimensional holograms at high frame rates. We use transmission DHM, which measures transparent media based on quantifying phase disparities induced by the measured sample. In short, this approach works by comparing phase differences induced in the coherent light transmitted through the sample with reference light traversing an unobstructed path. Digital holographic microscopy has several advantages in comparison to conventional microscopic techniques. Numerical processing of the wavefront transmitted through the sample permits simultaneous computation of intensity and phase distribution [97]. The holographic measurements also make it possible to focus on different object planes without relative movement between the stage and the lens [98] and enables numerical lens aberration correction [99]. Our unique DHM system operates at high frame rates (40,000 frames per second) and consists of a custom-built perfusion chamber with a built-in ultrasound transducer (Fig. 4.1a). A heated stage keeps the media at a constant temperature over the duration of the recording. The system reconstructs phase images of cells that are then analyzed to determine the baseline profile (prior to ultrasound), during exposure to ultrasound, and afterwards. This enables us to accurately visualize the maximum displacement of the membrane from the mean position under the influence of ultrasound.

The measurements of apical cellular membrane deflection due to ultrasound consisted of a 25 ms baseline recording, followed by a 50 ms ultrasound stimulus and a 25 ms post-stimulus dwell (Fig. 4.1b), leading to a median deflection of 214 nm for human embryonic kidney (HEK293)

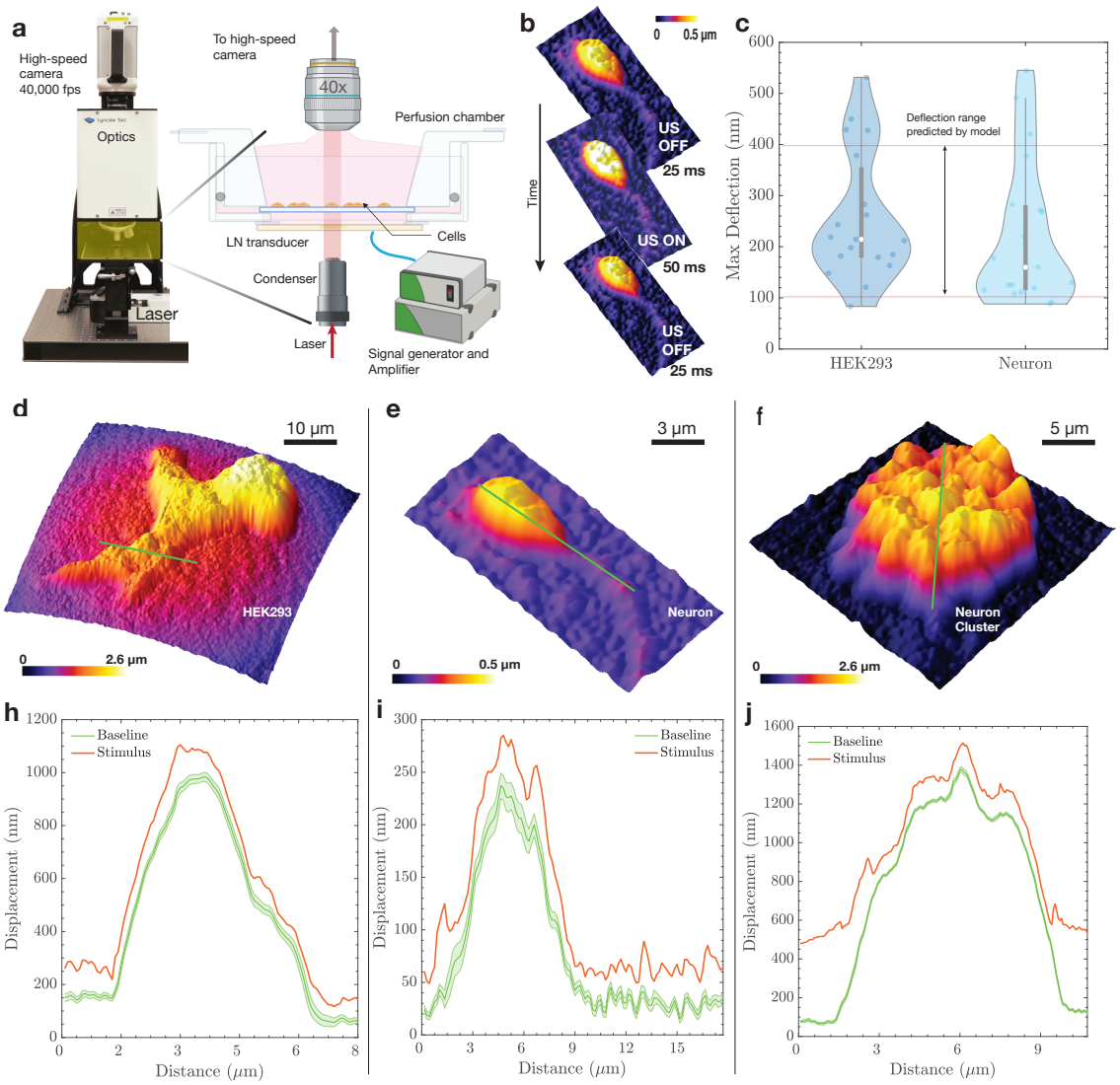

Figure 3.1: The deflection of the membrane under the influence of ultrasound was visualized using (a) high-speed digital holographic microscopy (DHM). The DHM setup included a lithium niobate transducer driven by a signal generator and an amplifier at 6.72 MHz. The cells were mounted on a coverslip and placed in a custom perfusion chamber maintained at 37°C. The DHM enables the (b) quantitative reconstruction of phase images acquired by the high-speed camera at 40,000 frames per second. Each recording began with 25 ms of no stimulus as a baseline, followed by a 50 ms ultrasound stimulus, and ended with a 25 ms baseline. (c) The maximum deflection from the mean position was found to be 100–400 nm, with a median deflection of 214 nm for HEK293 cells and 160 nm for neurons (N = 30 for each cell type). Reconstructed phase profiles are shown for different cell types: (d) HEK293 cells, (e) neurons and (f) neuronal clusters. Displacement was measured as a function of distance along the green lines provided in the (d–f) contour plots and were (g–i) plotted with (red line plot, max displacement during stimulus) and without (green plot, Baseline) ultrasound stimulus. A distance of "zero" in (g–i) is at the left end of the green line in (d,e) and at the bottom of the green line in (f). For the (green) baseline displacement, note the mean and 95% confidence intervals are provided. The maximum variation throughout all baseline responses was less than ±20 nm.

cells and 159 nm for neurons, with a range of 100 nm to 550 nm across the two tested cell types (Fig. 4.1c and Supplementary Videos 1 and 2). These stimulation parameters are consistent with prior studies for calcium imaging in vitro and in vivo [40] and are consistent with recommendations from past important work [100]. Sample reconstructed phase images of HEK cells, neurons and neuronl clusters are shown in Fig. 4.1d-f. The baseline deflection for these samples, including a 95% confidence interval, had a range of ± 20 nm, inclusive of both random thermal fluctuations across the cell membrane and potential noise introduced to the system due to the imaging arrangement (Fig. 4.1g-i). Sample displacement baseline membrane profiles are illustrated in Fig. 4.1g–h (*see* Supplemental Videos as well) for HEK cells and neurons, and Fig. 4.1i represents the deflection profile for a cluster of neurons. The cluster was imaged to confirm deflection in a group of neurons and help provide insight into the *in vivo* mechanisms of activation. Results from the neuronal cluster show that the magnitude of deflection remains roughly the same for a group of cells as for a single neuron. The larger deflection at the edges of the cluster is due to the neurons at the edges being less constrained in comparison to the ones in the center.

Membrane deflection during the generation of action potentials has been observed in the past [101], but the converse phenomenon of membrane deflection leading to the generation of action potentials has not been explored at the level of an individual neuron using clinically relevant stimulation pressures. As described before, other imaging techniques have been reported for measuring cell membrane deflection, but are unable to match the spatiotemporal capabilities of the high-speed DHM technique. Overall, our experimental setup allows us to confirm membrane deflection due to ultrasound for cells adherent to a coverslip and we relate these results to a mathematical model in the following section.

3.3.2 Membrane deflection model

Based upon the results from the experiments, with cells cultured on a surface and surrounded by media, the membrane is assumed to be fixed at the periphery. A similar case occurs *in vivo*, where the extracellular matrix holds individual cells in place and provides anchoring locations for sections of the membrane [102]. Cellular anchoring is important because it imposes a characteristic distance over which the range of permissible deflection wavemodes may occur [*see* methods]. Its deflection is restricted in the analysis to a single direction, perpendicular to the plane of the membrane and

parallel to the direction of propagation of sound. The model does not take into account the restoring effects of the actin cytoskeleton, which is difficult to estimate and likely plays an important role in restoring the membrane to its original equilibrium position.

The stimulus provided to the cells is in the form of a sinusoidal *burst*, a short-term continuously oscillating ultrasound signal of constant amplitude and frequency. In a burst, a sinusoidal electrical signal is typically applied across the piezoelectric material used in a transducer, which transforms this signal into a sinusoidally varying pressure field in the fluid medium at the frequency of excitation. This is rather different than the approach used by Prieto et. al [84], where the ultrasound is modeled as a step increase in hydrostatic pressure from zero to a fixed positive value at $t = 0$. In our approach [*see* methods], the burst signal oscillates at the ultrasound frequency, and an analytical solution for the slower time scale of the membrane mechanics is found in response to this harmonic ultrasound excitation. This solution is then used in a numerical model to produce the solution for the deflection of the fixed membrane, resolving the discrepancy between the timescales of ultrasonic stimulation ($\sim$0.1 μs) and the experimentally verified membrane deflection occurring on the order of milliseconds. This hybrid approach was chosen because a numerical simulation of the entire phenomena from ultrasound to membrane deflection would be extremely difficult due to the vastly different spatiotemporal scales, even with state-of-the-art computational resources. Finally, the hydrostatic pressure included by Prieto et. al [84] is discarded here, because it is orders of magnitude lower than the ultrasonic radiation pressure.

The damped wave equation describing the deflection, u, of the membrane in response to ultrasonic pressure, P_{US}, is written as

$$\rho\,\partial_t^2 u = 2\,\eta\,\frac{\partial^3 u}{\partial x^2 \partial t} + \left(2\,\gamma\,\partial_x^2 u + P_{\mathrm{US}}\right)\left(\frac{\pi}{d}\right), \tag{3.1}$$

where ρ and η are the dynamic viscosity and density of the surrounding fluid, both assumed to be the same as water as used in prior studies [103, 104]); γ is the surface tension between the membrane and media; and d is the characteristic length of the membrane between anchor points. Equation (3.1) was solved by the method of eigenfunction expansion [methods]. Figure 4.1 provides results representative of the analysis, with a 1 MPa pressure supplied to the membrane using a 7 MHz transducer in the form of a sine wave over a period of 5 ms. The mechanical index for

the parameters listed in this study is 0.37, well below the oft-cited mechanical index threshold for cavitation onset of 0.7 in bubble-perfused tissue [105]. However, our study uses no bubbles. In this case, the U.S. Federal Drug Administration's mandated clinical safety threshold index of 1.9 without introduced microbubbles [106, 107] is more appropriate. These data suggest that we are unlikely to cause cavitation and cell viability remains unaffected as shown by prior work with similar stimulus parameters [40].

Maximum membrane deflection occurs when the ultrasound stimulus is applied (Fig. 4.2a), followed by decay due to viscous losses to the host medium. The magnitude of deflection depends on the stimulation frequency and peak pressure, with lower frequencies and higher pressures producing greater membrane deflection. The critical parameters that influence the deflection magnitude are the characteristic membrane anchor length and surface tension, as shown in Fig. 4.2b. The deflection predicted by the model for dimensions relevant to the size of a cell are between 100 nm to 400 nm, irrespective of the value of surface tension for an anchor length ranging from 5 - 20 μm based on the average size of the soma [108] and average diameter of HEK cells [109]. We modelled membrane deflection due to a range of surface tension values reported in the literature [84, 110]. Maximum membrane deflection occurs at the midpoint of the axisymmetric membrane model. This is portrayed in Fig. 4.2c, where we provide graphical "snapshots" of the ultrasonically-forced membrane over time. The closed-form displacement solution to Eq. (3.1) allows us to link the fast ultrasonic timescales (on μs order, or, *total* response) to phenomena occurring at observable timescales (on ms order, or, *observed* response), as shown in Fig. 4.2d. The character of the membrane "slow time" response—that is, its ability (or lack thereof) to sustain oscillations—is governed by the value of the Ohnesorge number, Oh. The term is defined in this way because the membrane oscillations typically occur slowly: at a frequency far less than the incident ultrasound.

The nondimensional parameter Oh characterizes the importance of dissipative viscous forces relative to the combined interaction of conservative inertial and surface tension forces. In other words, Oh characterizes, on average, the extent to which the membrane dissipates or conserves mechanical energy. Typical Oh values for neurons range from $\sim$0.06 to $\sim$0.45 based on values of surface tension, viscosity and membrane length considered in this work. This implies that inertial and surface tension forces dominate over viscous forces: the slow time membrane response is characteristically oscillatory. This behavior results from the membrane's tendency toward retaining

mechanical energy in the form of sustained oscillations when $Oh < \sqrt{2/\pi} \approx 0.8$. This is explicitly derived in the detailed analysis [*see* methods] and suggests that the slow time oscillations of the ultrasonically actuated membrane is implicated in the changes in the membrane capacitance as detailed in the following sections.

3.3.3 Model prediction of action potentials and electrophysiology

To model the electrical output of a neuron under the influence of ultrasound, a modified version of the original Hodgkin-Huxley equations is first used[111],

$$\frac{dV_m}{dt} = -\frac{1}{C_m}\left[I_{\text{app}} + I_{\text{Na}} + I_{\text{Kd}} + I_{\text{M}} + I_{\text{leak}}\right]. \tag{3.2}$$

In this equation, the membrane potential of the neuron, V_m, changes over time with respect to the membrane capacitance, C_m, and the underlying currents, I_{app}, I_{Na}, I_{Kd}, I_{M}, and I_{leak}. At rest, $V_m = -71.9$ mV is the well-known membrane potential of the cell and, notably, the action potential generation is controlled by the presence of an applied current, I_{app}, while the other currents are based on the membrane morphology and chemistry and are detailed in the methods. The increase of I_{app} beyond a certain threshold produces spiking behavior typical of neurons.

The capacitance, C_m, may also fluctuate due to a morphological change in the membrane. Such a modification is not modeled in the original representation of this equation, but it may be included. The voltage change as described in eqn. (3.2) includes a time-dependent capacitive current, $I_{\text{app}} \equiv V_m \frac{dC_m}{dt}$. With this included in eqn. (3.2), it is possible to solve the differential equation for the voltage and gating variables while incorporating the capacitance change due to membrane deflection. Membrane deflection is constrained to a certain extent due to parts of the cell that are adherent to the substrate or the extracellular matrix. This causes an increase in area between the adherent locations and with sufficient deflection, this produces a depolarization across the membrane. The value of the transmembrane voltage is dependent on the magnitude and duration of the applied stimulus. Figure 4.3 indicates the change in capacitance due to 6.72 MHz ultrasound at 0.5 MPa (Fig. 4.3a) and 1 MPa (Fig. 4.3b) with the corresponding area fluctuations that bring about the change in capacitance represented in Fig. 4.3c. In order to compute the time-dependent membrane area variation, we extract the slow time output of Eq. (3.1) for use with the axisymmetric area

integral. The capacitance of the membrane is then determined by treating it as a dielectric between charged surfaces. This produces a slow time capacitive response, bearing an order of magnitude equivalence to the ion channel relaxation times in the modified Hodgkin-Huxley model [112].

The stimulus of 1 MPa results in depolarization as indicated in Fig. 4.3d, while the lower pressure does not result in the generation of an action potential over the stimulus duration. Reported values of baseline membrane capacitance have been shown to vary [113], and we show that longer stimuli will result in the generation of action potentials as a cumulative effect of capacitance change over the duration of the stimulus. Figure 4.3e represents transmembrane voltage changes for a stimulus of 50 ms. We notice that depolarization takes place in both cases. However, initial spikes are delayed by up to 20 ms in the lower pressure case, indicating the need for increased stimulus durations for lower pressures. Our model also shows a lower spike frequency for the 0.5 MPa case in comparison to 1 MPa. The simulation output of our model for the lower pressure and longer stimulus duration case were verified experimentally using voltage clamp electrophysiology (Fig. 4.3f) and shows an initial spike corresponding to the delivery of the ultrasound stimulus, followed by oscillations.

3.4 Discussion

We model how ultrasound results in membrane deflection and eventually leads to transmembrane voltage changes. In a first, we demonstrate real-time membrane deflection due to ultrasound using high-speed DHM imaging (Supplementary Videos 1 and 2). We leverage the Hodgkin-Huxley equations, which are a set of phenomenological equations describing action potential generation in a squid axon and are one of the most important neuronal models. However, observations of mechanical deflection accompanying action potentials [101] show that the underlying assumptions of the Hodgkin-Huxley model may need to be revisited, as there are mechanical phenomena involved. In the context of ultrasound neuromodulation, our model presents insights into the the generation of action potentials due to mechanical deflections and is theoretically supported by models such as the ones put forth in the past few years [88, 114]. The deflection due to the applied ultrasound stimulus results in a net area change of the membrane between the two pin locations that represent an adherent cell. The area changes take place elastically while maintaining constant volume. This

results in a change in capacitance that, when incorporated in the Hodgkin-Huxley model, results in transmembrane voltage changes. Capacitance of the membrane can be modeled using an expression for a parallel plate capacitor [115], and an increase in area results in a proportional increase in capacitance [*see* methods].

The model does not take into account restoring effects of the actin cytoskeleton, whose influence will lower the membrane deflection and cause the inner leaflet to deflect less than the outer leaflet. However, this cannot account for the ∼100 nm deflection experimentally observed in this work, and only plays a minor role in bringing about capacitance changes according to previous studies [81]. The model and the use of high-speed DHM imaging present opportunities for exploring the influence of ultrasound on native neurons and HEK293 cells, as presented here. A combination of fluorescence imaging with DHM can be used to image focal adhesions and cells that have been engineered to express membrane proteins that are sensitive to ultrasound stimuli, in other words using sonogenetics [39]. At a cellular level, there are two proposed models for the activation of a mechanically-gated ion channel: the force from lipid model and the force from filament model. The force from lipid model was put forth by Martinac *et al.* [116] and proposes that changes in membrane tension or local membrane curvature result in opening or closing of channels. In the force from filament model [110], the stimulus is transferred to tethers that connect the membrane to the cytoskeleton. Conformational changes in the tethers result in opening or closing of the channel. In reality, both models play a part in opening and closing a given channel.

Although it is difficult to estimate the relative contribution of these mechanisms, it is possible to estimate the deflection of the cell membrane as highlighted in the preceding sections. This is of particular significance when we consider the membrane-bound proteins such as TRPA1, MsCL [55], Piezo [57] and their interaction with the actin network. Disruption of the actin cytoskeleton has been shown to reduce mechanosensitive activity of such ion channels [117] and it is possibly due to decreased separation between the leaflets of the bilayer when the actin network is disrupted. In addition to quantifying the deflection due to mechanosensitive proteins, there is potential to quantify the forces on the cell due to ultrasound using FRET (Förster resonance energy transfer) force sensors [118].

Our model also predicts the generation of action potentials from capacitive changes that occur when the adherent cell is exposed to ultrasound. Charge across the membrane is maintained by

a gradient in ion concentration across the cell membrane, with Na^+ ions on the outside and Cl^- ions on the inside, resulting in a net negative resting potential. As the membrane deflects, it is partially constrained by the adherent regions, resulting in an increase in area of the membrane between the adherent locations. An increase in the area of the membrane directly increases its capacitance (*see* eqn. (3.18) in Methods). This relationship between area, capacitance and transmembrane voltage change has also been indicated in prior publications that investigate, outside the context of ultrasound neuromodulation, the capacitive properties of biological membranes [115].

We demonstrate transmembrane voltage changes for two cases, a pressure of 0.5 MPa and 1 MPa and observe that voltage changes only take place for the higher pressure case for lower stimulus durations, defining a pressure threshold dependent upon the duration of stimulus. We also investigate the influence of longer stimulus durations on the generation of action potentials for different values of baseline capacitance. As verified by a current clamp electrophysiology study in the whole cell configuration, increased stimulus durations even at at lower pressures result in action potential generation, though with lower spike rates. The parameters used in this study are similar to prior work *in vivo* [40] and deflection has been shown by other groups to occur *in vivo* by Lee et al. [87], although at much higher pressures and with cavitation.

One of the limitations with performing single cell current clamp electrophysiology while using ultrasound at amplitudes sufficient to drive a physiological response is the loss of a seal between the membrane and the patch pipette due to the membrane's deflection. There are, however, reports of current clamp electrophysiology results with ultrasound using microbubbles [119] and at much higher frequencies [120] or with devices [121]. In each of these three cases, there is reason to believe that while the stimulation techniques or device may work for *in vitro* work, they will not be suitable for *in vivo* work. One potential way to overcome this issue would be to perform electrophysiological recordings for cells encased in matrigel that would limit the movement of the recording pipette with respect to the membrane.

Until now, the mechanisms underlying ultrasound neuromodulation have lacked explanation and existing models lack experimental data. Taken together, our results offer valuable insight into the underlying effects of ultrasound on cell membranes, as well as insight into how these effects translate to transmembrane voltage changes. The predictions of our model were confirmed using a novel, high-speed imaging technique. We were able to visualize and quantify membrane deflection

in real-time and predict depolarization due to the imposed ultrasound stimulus.

3.5 Methods

3.5.1 HEK293 cell culture

Human embryonic kidney (HEK293) cells (CRL-1573, ATCC, Manassas, Virginia, USA) were cultured using standard procedure in DMEM supplemented with 10% fetal bovine serum (FBS) and 20 mM glutamine in a 37°C and 5% CO_2 incubator. Cells beyond passage 30 were discarded and a new aliquot was thawed. For experimental plating, 18 mm coverslips were coated with poly-d-lysine (PDL; 10 g/L, minimum 2 hours, P6407, Sigma-Aldrich, St. Louis, Missouri, USA), and HEK293 cells were seeded at 150K, 200K, or 250K cells/mL for 24 hours before the experiment. Cells were allowed to grow over 24 hours and a balance was struck between an increase in the cell density to improve cell health and the need to perform observations with the DHM that improve as the cell density is decreased. The cells are healthier at a higher density, but the DHM relies on contrast between a given cell and its environment, which is reduced as the cell density increases. For imaging, coverslips were mounted on a specialized chamber featuring an ultrasound transducer approximately 2 mm below the coverslip and a 10 mL reservoir of media above the coverslip. Once cells were in focus, a 6.72 MHz ultrasound pulse of 50 ms duration was delivered while imaging with an immersion objective as described in following sections, and a cell membrane profile was reconstructed and analyzed.

3.5.2 High-speed digital holographic microscopy

HEK cells and neurons were observed through a 40X, 0.8 NA (numerical aperture) water immersion microscope objective. The field of view used for the setup was 60.5 μm $\times$ 60.5 μm, with a vertical accuracy and repeatability of 4 nm and 0.08 nm respectively [122]. Holograms were recorded using a high-speed camera (Nova S12, Photron, San Diego, California, USA). Acquisition and reconstruction were performed using custom software (Koala, Lynceé-tec Inc., Lausanne, Switzerland) on a computer workstation. Data were recorded on a separate computer equipped with a solid-state drive, with each 100 ms recording equating to $\sim$ 20 gigabytes of data. The observations reported in this study represent a combined analysis of 1.4 terabytes of data. The

data were reconstructed after each batch of six coverslips was processed in order to reduce the time between trials and to ensure optimum cell health. The setup consisted of a custom perfusion chamber that was built to accommodate a lithium niobate transducer operating at 6.72 MHz. The perfusion chamber was housed on a stage maintained at 37°C (Fig. 4.2a) using a heated stage (Bioscience Tools TC-100s).

3.5.3 Modeling of deflection and transmembrane voltage changes

As the pressure wave propagates through the fluid and contacts the adherent cell, the region of the cell membrane between adhesion zones deflects. This deflection leads to a change in area of the membrane and causes a capacitance change. The two-dimensional model assumes that the membrane has a known value of surface tension [123]. The membrane is surrounded by a fluid, assumed to have the properties of water in this case. The vertical displacement of the membrane is approximated to be equal to the displacement of the fluid just above the membrane. We start with a simplified version of the Navier-Stokes equation,

$$\rho\,(\partial_t\, v + v\cdot\nabla\, v) = \eta\,\nabla^2\, v - \nabla\, P, \tag{3.3}$$

where ρ and η are the density and viscosity of water, respectively. The expression ∇P is the pressure gradient and v is the velocity. In Eq. (3.3), the convective acceleration is $v\cdot\nabla v = 0$ as the flow is unidirectional in z [124] and the fluid is assumed to be incompressible. The membrane is symmetric in x and y, allowing the viscous term to be simplified as $\partial_x v_z = \partial_y v_z$. We are left with

$$\rho\,\partial_t\, v_z = 2\,\eta\,\partial_x^2\, v_z - \nabla\, P. \tag{3.4}$$

The net pressure gradient in this case is a function of the time dependent pressure in the fluid due to ultrasound and the surface tension of the membrane, which resists deformation:

$$\nabla\, P = -\,(\,2\,\gamma\,\partial_x^2\, u + P_{\mathrm{US}}\,)\,\pi\, d, \tag{3.5}$$

where u is the displacement in z and P_{US} is the pressure due to an ultrasound source, typically acting in the form of a sinusoidal pulse, $P_{\mathrm{US}} = P_0 \sin(\omega t)$, where $\omega = 2\pi f$. By contrast, Prieto *et al.* [84] at this point chose to represent the ultrasound as a step change in the pressure, from a static, zero relative pressure to a static positive value at time $t = 0$ well below the pressure amplitudes used in experimental studies, typically 1 kPa to 1 MPa. Prieto *et al.*'s representation is numerically attractive but difficult to reconcile with the harmonic oscillatory pressure delivered by the transducer. In the absence of an analytical solution for the ultrasound propagating through the medium and membrane, one would be forced to numerically represent the MHz-order sinusoidal signal with sufficiently small spatiotemporal step sizes to satisfy the Nyquist criterion, and do so for at least several hundred milliseconds to determine the response of the cell membrane to the ultrasound pressure oscillation, producing very large models with many millions to billions of temporal steps for a single solution. Consequently, these past studies have been understandably forced to make spurious approximations[3] to avoid impossibly prohibitive computation times.

Substituting this into Eq. (3.4) produces a partial differential equation for the displacement of the membrane driven by ultrasound:

$$\rho\, \partial_t^2 u = 2\,\eta \frac{\partial^3 u}{\partial x^2 \partial t} + \left(2\,\gamma\, \partial_x^2 u + P_{\mathrm{US}}\right) \left(\frac{\pi}{d}\right). \tag{3.6}$$

The boundary conditions are the clamped conditions at the ends of the membrane and the initial displacement condition,

$$u(0,t) = 0, \tag{3.7a}$$

$$u(d,t) = 0, \tag{3.7b}$$

$$u(x,0) = \frac{P_0\, x\,(d-x)}{4\,\gamma} \equiv u_0(x), \tag{3.7c}$$

$$\partial_t\, u(x,0) = 0. \tag{3.7d}$$

If hydrostatic pressure is included, the initial condition for membrane displacement may be found by solving $P_o + 2\,\gamma\, \partial_x^2 u = 0$. The general soltuion to partial differential Eq. 3.6 was obtained

[3] One can use the analytical solution to show that the results from the noted study are spurious when the correct amplitudes and frequencies of the ultrasound are used.

with the method of eigenfunction expansion, as outlined further on. This is achieved using an orthogonal eigenbasis:

$$\phi_n(x) = \sin(\sqrt{\chi_n}\, x), \tag{3.8}$$

where $\chi_n = (n\,\pi/d)^2$ corresponds to the n^{th} wavemode for a membrane with diameter d. Expanding u gives us

$$u(x,t) = \sum_n u_n(x,t) = \sum_n h_n(t)\,\phi_n(x), \tag{3.9}$$

so that clearly the even modes vanish and we may write $n = 2\,k+1$, and $k \in \mathbb{Z} \geqslant 0$ where $\mathbb{Z}$ is an integer set. Substituting this expression into (3.6), one has

$$\sum_n (\ddot{h}_n + c_1\,\chi_n\,\dot{h}_n + c_0\,\chi_n\,h_n)\,\phi_n(x) = f(t), \tag{3.10}$$

where $c_1 = 2\,\eta/\rho$ and $c_0 = 2\,\pi\,\gamma/\rho\,d$, are written in terms of the density of the surrounding fluid, ρ; the viscosity of the surrounding fluid, η; the surface tension along the fluid-membrane interface, γ; and the membrane diameter, d. By multiplying both sides by $\phi_m(x)$ (with $m \in \mathbb{Z}^+$), integrating over x from 0 to d, and then leveraging the orthogonality of sines, we find that the time-dependent component for the n^{th} eigenmode satisfies the second-order ordinary differential equation

$$\ddot{h}_n + b_{1,n}\,\dot{h}_n + b_{0,n}\,h_n = \hat{f}_n(t), \tag{3.11}$$

where $b_{1,n} = c_1\,\chi_n$, $b_{0,n} = c_0\,\chi_n$, and

$$\hat{f}_n(t) = \frac{2}{d}\int_0^d \phi_n(x)\,f(t)\,\mathrm{d}x = \frac{2\,(1-(-1)^n)}{n\,\pi}\,f(t). \tag{3.12}$$

The means for obtaining a solution to equations of the form (3.11) is well known. The homogeneous solution and its coefficients are given by

$$h_n^{(h)}(t) = a_{+,n}^{(h)} e^{r_{+,n} t} + a_{-,n}^{(h)} e^{r_{-,n} t} \tag{3.13}$$

where the coefficients $a_{+,n}^{(h)}$ and $a_{-,n}^{(h)}$ are

$$a_{+,n}^{(h)} = \frac{r_{-,n}}{r_{-,n} - r_{+,n}} h_n(0), \tag{3.14a}$$

$$a_{-,n}^{(h)} = \frac{r_{+,n}}{r_{+,n} - r_{-,n}} h_n(0). \tag{3.14b}$$

The inhomogeneous solution is

$$h_n^{(i)}(t) = \frac{1}{r_{+,n} - r_{-,n}} \left(e^{r_{-,n} t} \mathcal{I}_{-,n}(t) - e^{r_{+,n} t} \mathcal{I}_{+,n}(t) \right), \tag{3.15}$$

where

$$\mathcal{I}_{\pm,n}(t) = \int_0^t e^{-r_{\pm,n} \tau} \hat{f}(\tau)\, d\tau. \tag{3.16}$$

The total waveform solution is then numerically implemented by taking a finite-term approximation of (3.9).

The change in area, A, of the membrane then be calculated once the time-dependent membrane deflection is obtained:

$$A = \int_0^d 2\pi \sqrt{\left(1 + (\partial_x u)^2\right)}\, dx. \tag{3.17}$$

By extension, this allows us to determine the change in membrane capacitance, C, due to the area change,

$$C = \frac{\epsilon_0 \epsilon A}{L}, \tag{3.18}$$

where we have regarded the membrane as a dielectric between two charged surfaces. In this case, L is the thickness of the bilayer and has values between 4 nm and 9 nm, and the relative

permittivity, ϵ, has a value of 2 [125].

The above value of capacitance change is coupled with the modified Hodgkin-Huxley neuronal model, where the capacitive current is defined as $I_{\text{app}} \equiv V_m \frac{dC_m}{dt}$. This model contains a voltage-gated sodium current and delayed-rectifier potassium current to generate actions, a slow non-inactivating potassium current to recapitulate the spike-frequency adaptation behavior seen in thalamocortical cells, and a leakage current.

Equation (3.19) defines the voltage-gated Na^+ current where $\bar{g}_{\text{Na}} = 56\,\text{mS/cm}^2$ is the maximal conductance and $E_{\text{Na}} = 50\,\text{mV}$ is the Nernst potential of the Na^+ channels. The parameter $V_{\text{th}} = -56.2\,\text{mV}$ sets the spike threshold

$$I_{\text{Na}} = \bar{g}_{\text{Na}} \cdot m^3 \cdot h \cdot (V_m - E_{\text{Na}}) \tag{3.19}$$

where the gating variables m and h vary with time according to

$$\frac{dm}{dt} = \alpha_m \cdot (1 - m) - \beta_m \cdot m, \tag{3.20a}$$

$$\frac{dh}{dt} = \alpha_h \cdot (1 - h) - \beta_h \cdot h, \tag{3.20b}$$

$$\alpha_m = \frac{-0.32 \cdot (V_m - V_{\text{th}} - 13)}{\exp\left[-(V_m - V_{\text{th}} - 13)/4\right] - 1}, \tag{3.20c}$$

$$\beta_m = \frac{0.28 \cdot (V_m - V_{\text{th}} - 40)}{\exp\left[(V_m - V_{\text{th}} - 40)/5\right] - 1}, \tag{3.20d}$$

$$\alpha_h = 0.128 \cdot \exp\left[-(V_m - V_{\text{th}} - 17)/18\right], \tag{3.20e}$$

$$\beta_h = \frac{4}{1 + \exp\left[-(V_m - V_{\text{th}} - 40)/5\right]}. \tag{3.20f}$$

The delayed rectifier K^+ current is

$$I_{\text{Kd}} = \bar{g}_{\text{Kd}} \cdot n^4 \cdot (V_m - E_{\text{K}}), \tag{3.21}$$

where $\bar{g}_{\text{Kd}} = 6\,\text{mS/cm}^2$ is the maximal conductance of the delayed-rectifier K^+ channels and $E_{\text{K}} =$

$-90\,\mathrm{mV}$ is the Nernst potential of the K^+ channels, and with n evolving over time as

$$\frac{dn}{dt} = \alpha_n \cdot (1-n) - \beta_n \cdot n, \tag{3.22a}$$

$$\alpha_n = \frac{-0.032 \cdot (V_m - V_{\mathrm{th}} - 15)}{\exp\left[-(V_m - V_{\mathrm{th}} - 15)/5\right] - 1}, \tag{3.22b}$$

$$\beta_n = 0.5 \cdot \exp\left[-(V_m - V_{\mathrm{th}} - 10)/40\right], \tag{3.22c}$$

A slow non-inactivating K^+ current may be defined as

$$I_{\mathrm{M}} = \bar{g}_{\mathrm{M}} \cdot p \cdot (V_m - E_{\mathrm{K}}), \tag{3.23}$$

where $\bar{g}_{\mathrm{M}} = 0.075\,\mathrm{mS/cm^2}$ is the maximal conductance and $\tau_{\max} = 608\,\mathrm{ms}$ is the decay time constant for adaptation of the slow non-inactivation K^+ channels. The parameter p is such that

$$\frac{dp}{dt} = \frac{p_\infty - p}{\tau_p}, \tag{3.24a}$$

$$p_\infty = \frac{1}{1 + \exp\left[-(V_m + 35)/10\right]}, \tag{3.24b}$$

$$\tau_p = \frac{\tau_{\max}}{3.3 \cdot \exp\left[(V_m + 35)/20\right] + \exp\left[-(V_m + 35)/20\right]}. \tag{3.24c}$$

The leakage current is

$$I_{\mathrm{Leak}} = \bar{g}_{\mathrm{Leak}} \cdot (V_m - E_{\mathrm{Leak}}), \tag{3.25}$$

where $\bar{g}_{\mathrm{Leak}} = 0.0205\,\mathrm{mS/cm^2}$ is the maximal conductance and $E_{\mathrm{Leak}} = -70.3\,\mathrm{mV}$ is the Nernst potential of the non-voltage-dependent, non-specific ion channels.

We set the following initial conditions for the gating terms:

$$m_0 = \frac{\alpha_m}{\alpha_m + \beta_m}, \tag{3.26a}$$

$$h_0 = \frac{\alpha_h}{\alpha_h + \beta_h}, \tag{3.26b}$$

$$n_0 = \frac{\alpha_n}{\alpha_n + \beta_n}, \tag{3.26c}$$

$$p_0 = p_\infty. \tag{3.26d}$$

Equations (20) through (25) are solved with initial conditions (27) to obtain the transmembrane voltage change of a neuron when subjected to ultrasound stimuli.

3.5.4 Sustaining oscillations on the membrane

A better understanding of the membrane wave propagation can be obtained by considering the decay transience of the constituent wavemodes within the context of the solution to Eq. (3.11). Each wavemode will have a solution of the form

$$h_n(t) = h_n^{(h)}(t) + h_n^{(i)}(t), \tag{3.27}$$

where $h_n^{(h)}$ is the homogeneous solution and $h_n^{(i)}$ is the inhomogeneous solution for the forced wavemode propagation initialized from zero initial conditions. The general form of the former can be used to characterize the decay transience,

$$h_n^{(h)}(t) = a_{+,n}^{(h)} e^{r_{+,n}\, t} + a_{-,n}^{(h)} e^{r_{-,n}\, t}, \tag{3.28}$$

where the coefficients $a_{\pm,n}^{(h)}$ are determined by the initial conditions and $r_{\pm,n}$ are the eigenvalues of the left side of (3.11) (the roots of the characteristic equation):

$$r_{\pm,n} = -\frac{1}{2}\left(b_{1,n} \pm \sqrt{b_{1,n}^2 - 4\, b_{0,n}}\right). \tag{3.29}$$

Then the discriminant determines the character of the wavemode:

$$b_{1,n}^2 - 4\, b_{0,n} \begin{cases} > 0, & r_{\pm,n} \in \mathbb{R}, \quad \text{two distinct roots}, \\ = 0, & r_{\pm,n} \in \mathbb{R}, \quad \text{two degenerate roots}, \\ < 0, & r_{\pm,n} \in \mathbb{C}, \quad \text{two conjugate roots}. \end{cases} \tag{3.30}$$

The physical conditions for degeneracy require an exacting degree of marginality rarely (if ever) encountered in real systems, so that we may safely ignore this solution type (degeneracy corresponds to algebraic growth at small times that is mediated by exponential decay at long times).

Rewriting the conditions (3.30) in terms of physical parameters, one finds that

$$n \begin{cases} > \sqrt{\frac{2}{\pi}}\, Oh^{-1}, & r_{\pm,n} \in \mathbb{R}, \quad \text{strictly decaying wavemode,} \\ < \sqrt{\frac{2}{\pi}}\, Oh^{-1}, & r_{\pm,n} \in \mathbb{C}, \quad \text{oscillatory decaying wavemode,} \end{cases} \tag{3.31}$$

where

$$Oh = \frac{\eta}{\sqrt{\rho \gamma d}} \tag{3.32}$$

is the Ohnesorge number characterizing the balance between the dissipative viscous effects and the conservative effects resulting from interaction between inertia and surface tension. There exists a condition for oscillation of the unforced membrane and this condition is $Oh < \sqrt{2/\pi}$. When $Oh \geqslant \sqrt{2/\pi}$, no oscillatory unforced wavemodes are permitted and the unforced membrane *will not oscillate*. When the condition *is* satisfied, one observes that oscillation can be attributed exclusively to wavemodes with the "smallest" mode numbers, and that these will always include the fundamental mode. Fig. S3 represents the change in Oh for a range of surface tensions and membrane length.

3.5.5 Ultrasound transducer fabrication

We used a set of custom-made single crystalline 127.86 Y-rotated X-propagating lithium niobate transducers operating in the thickness mode, as previously described [126]. The fundamental frequency was measured to be 6.72 MHz using non-contact laser Doppler vibrometry (UHF-120SV, Polytec, Waldbronn, Germany). The transducers were coated with a 1 μm layer of Au atop 20 nm of Ti acting as an adhesion layer, using a direct-current sputtering (Denton 635 DC Sputtering system) process was used to coat 4 inch diameter wafers in an inert gas environment with a 2.3 mTorr pressure and rotation speed of 13 rpm, at a deposition rate of 1.5 A/s for Ti and 7 A/s for Au. Devices were diced to size (12 mm $\times$ 12 mm) and built in to the *in vitro* test setup using an automated dicing saw (DISCO 3220, DISCO, Tokyo Japan).

3.5.6 Rat Primary Neuron Culture

Rat primary neuronal cultures were prepared from rat pup tissue at embryonic days (E) 18 containing combined cortex, hippocampus and ventricular zone. The tissue was obtained from BrainBits (Catalog #: SDEHCV) in Hibernate-E media and used the same day for dissociation following their protocol.

Briefly, tissue was incubated in a solution of papain (BrainBits PAP) at 2 mg/mL for 30 min at 37°C and dissociated in Hibernate-E for one minute using one sterile 9" silanized Pasteur pipette with a fire-polished tip. The cell dispersion solution was centrifuged at 1100 rpm for 1 min, and the pellet was resuspended with 1 mL NbActiv1 (BrainBits NbActiv1 500 mL). The cell concentration was determined using a haemocytometer (TC20, Bio-Rad Labs, Hercules, California, USA) and neurons were plated in 12-well culture plates with 18-mm PDL-coated coverslips (GG-18-PDL, Neuvitro Corporation, Vancouver, Washington, USA) at a concentration of 1.3 million cells/well. Neurons were then incubated at 37°C, 5% CO_2, performing half media changes every 3-4 days with fresh NbActiv1 supplemented with PrimocinTM (ant-pm-1, InvivoGen, San Diego, California, USA). Cultures were incubated at 37°C, 5% CO_2 until day 10–12 and were used in DHM imaging experiments.

3.5.7 *In-vitro* electrophysiology

A stable line of neurons using the protocol listed above were cultured on 18 mm round coverslips, at a seeding density of ∼300k cells/well in a tissue-culture treated 12-well plate. Neurons were allowed to mature for 11-14 days in vitro prior to recording. Coverslips were transferred to a custom machined acrylic stage containing a bath of external solution; NaCl (140 mM), KCl (4 mM), $MgCl_2$ (2 mM), glucose (5 mM), and HEPES (10 mM) with an osmolarity of ∼290 mOsm. Patch pipettes were pulled on a pipette puller (P-97, Sutter Instruments, Novato, CA, USA) programmed to give 4-6 MΩ tips from filamented borosilicate glass (o.d. 1.5 mm, i.d. 0.86 mm) and used with an internal solution comprising of a CsF and KF base (#08 3008 and #08 3007, respectively, Nanion, Munich, Germany). A 40X water dipping lens (LUMPLFLN40XW, Olympus Corporation, Tokyo, Japan) with a numerical aperture (NA) of 0.8 was used in combination with a complementary metal oxide semiconductor (cMOS) camera (01-OPTIMOS-R-M-16-C QImaging OptiMOS, Roper

Technologies, USA) to visualize cells with Köhler or fluorescent illumination. Electrical signals were acquired using an amplifier (Axon Instruments Multiclamp 700B, Molecular Devices LLC, California, USA) and digitized (Axon Instruments Digidata 1550B, Molecular Devices LLC, California, USA) using an acquisition and control software (pClamp 11, Molecular Devices LLC, California, USA). Gap free recordings were conducted (typically holding the membrane potential at -70 mV) while delivering the ultrasound stimulus. The ultrasound delivery rig used for patch clamp experiments was the same used for imaging experiments. Briefly, waveforms were programmed using an arbitrary function generator (33600A Series, Keysight, California, USA) connected via BNC to an amplifier (TC2057574, Vox Technologies, Richardson, TX). Military communications grade BNC (Bayonet Neill–Concelman) cables (CA5512-36, Federal Custom Cable, California, USA) were used to ensure impedance matching in our systems and reduce electrical interference. The amplifier was connected to our custom-made lithium niobate transducer mounted on a dovetail sliding arm, and coupled to the bottom of the recording chamber with ultrasound gel. Recordings were carried out in response to peak pressures of 0.5 MPa as access resistance could not be maintained when high pressures were delivered. Upon successful whole-cell access, baseline gap-free recordings in current clamp trials were obtained. Access resistance during successful whole-cell recordings was maintained between 10 to 25 MΩ.

3.5.8 Statistical Analysis

The reconstructed holograms from the digital holographic microscope was exported using Koala (Lynceé-tec Inc., Lausanne, Switzerland) and analyzed using custom code written using MATLAB (Mathworks, Natlic, MA, USA) and ImageJ (National Institutes of Health, Bethesda, MD, USA). Line profiles along the length of the cell were exported using ImageJ for every frame and the mean baseline profile was calculated for each cell. The maximum deflection during the applied stimulus was then calculated for each cell by comparing the profile during the stimulus to the mean profile before the stimulus. Fig. 4.2c represents the maximum deflections of each neuron and HEK cell from the baseline during the applied stimulus. Fig. 4.2d-f represent the mean and maximum deflections when there is no ultrasound (green) and when the ultrasound stimulus is delivered (red).

3.6 Acknowledgements

This chapter, in full, is a reprint of A. Vasan et. al. (2022) "Membrane deflection results in cellular depolarization." *Advanced Science* 9.2 (2022): 2101950.. The dissertation author is the first author of this article.

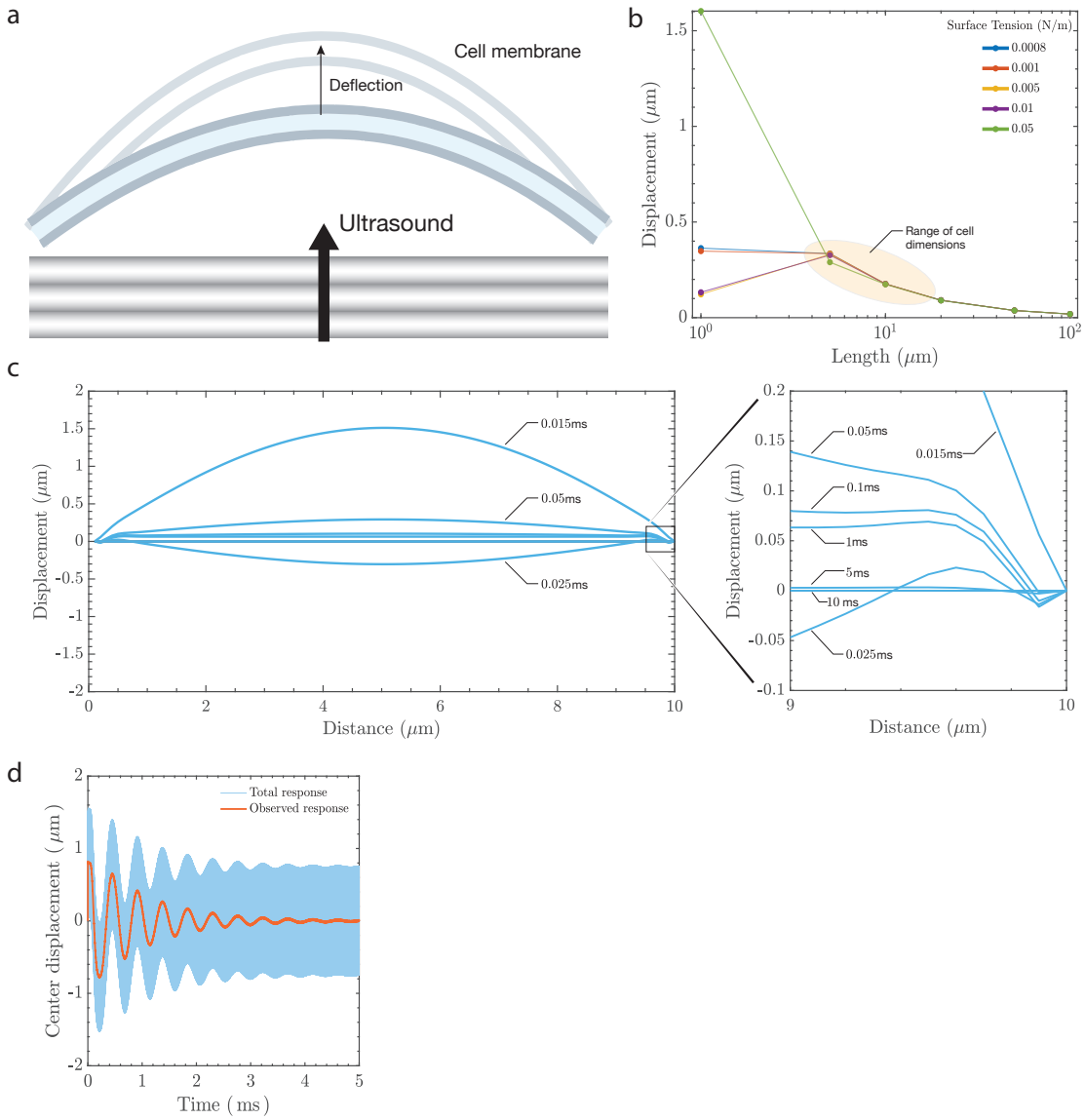

Figure 3.2: Ultrasound results in (a) membrane deflection that triggers a transmembrane electrical response. The cell membrane bilayer stretches, increasing its area, and the outer leaflet of the bilayer will likely deflect more than the inner leaflet due to the the presence of cytoskeletal components such as actin and microtubules that anchor the inner leaflet. Two of the factors that affect membrane displacement are surface tension of the lipid membrane and the length under consideration. The model (b) predicts displacements between 100–400 nm for dimensions that correspond to the size of a cell (5–20 µm) and is within the limits observed using the DHM. The response is (c) dynamic, with snapshots of the predicted deflection at different times (in ms) across a 10 µm wide membrane section that is anchored at the ends. The maximum deflection occurs when the stimulus is first provided and there is a balance between viscous dissipation and conservative effects of inertia and surface tension [*see* 4.4 in methods and section 2.2] which lead to sustained wavemodes on the membrane at the millisecond timescale (observed response). A low-pass temporal filter of the membrane's center displacement at 5 µm indicates (d) an oscillatory deflection over the stimulus duration of 5 ms.

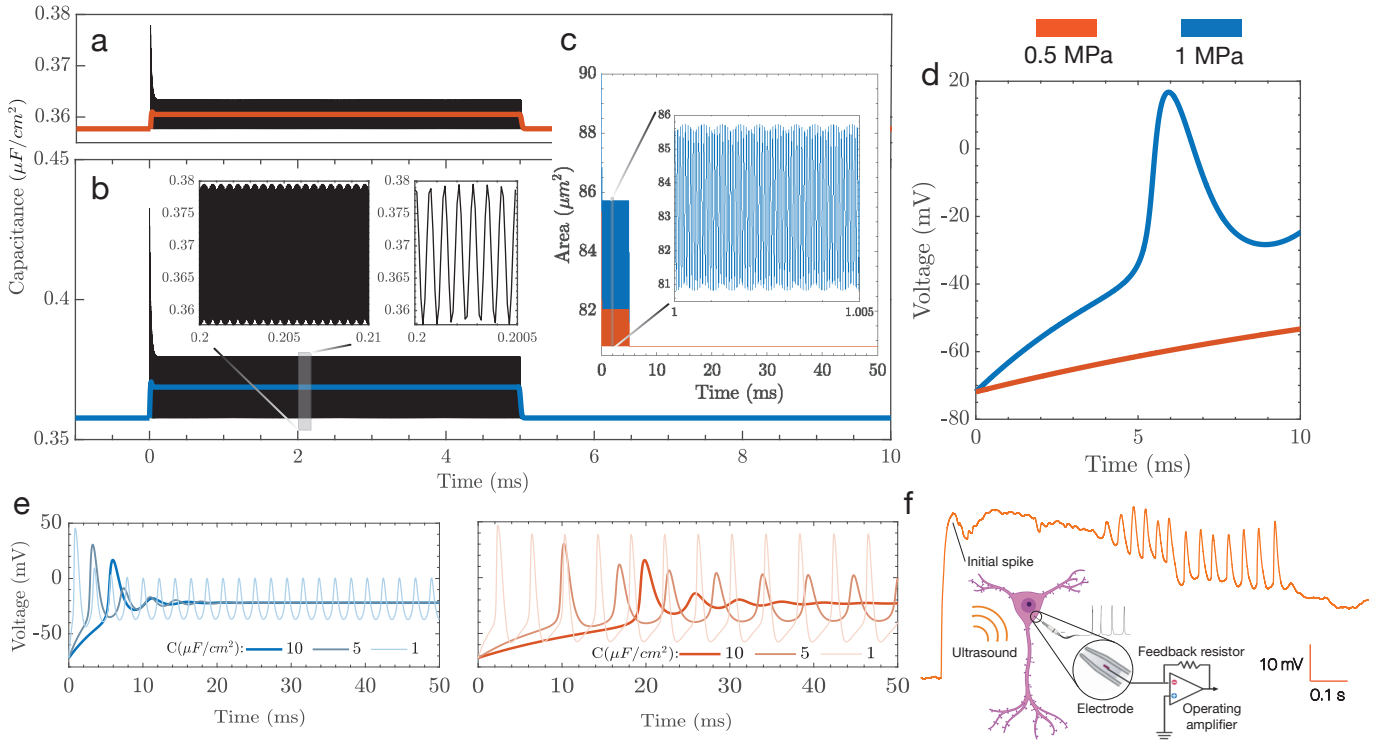

Figure 3.3: (a–e) Simulations help inform the development of stimulus parameters, in terms of time and pressure amplitude; note that throughout (a–e) 0.5 MPa stimulation is red while 1 MPa is blue. The capacitance changes are plotted over the stimulus duration (5 ms) for (a) 0.5 MPa and (b) 1 MPa with the corresponding area changes that cause (c) capacitance fluctuations. The capacitance fluctuations produce depolarization at 1 MPa, but not at 0.5 MPa, indicating (d) the presence of a pressure threshold to stimulate neurons. (e) Over a longer 50 ms stimulus, the action potential evolves quite differently over time for the two acoustic pressures. At lower pressures, longer stimuli may be necessary to produce action potentials. (f) In-vitro current clamp electrophysiology was used to verify the predictions of the model and shows that the presence of a preliminary spike followed by oscillations in voltage across the membrane.

Chapter 4

Ultrasonic interrogation of neural circuits: Non-invasive methods for probing activity

4.1 Chapter Abstract

Ultrasound has been used to modulate neural activity in rodents and primates, however combining stimuli with in vivo imaging or in freely moving animals has been challenging. Here, we design and validate two transducers to overcome these challenges in the rodent. We first use a transparent device to couple ultrasound stimuli with two-photon microscopy. Using this setup, we find that ultrasound triggers a stimulus intensity dependent activation of parvalbumin positive interneurons in the rodent visual cortex. Next, we develop a head-mounted transducer that can be combined with a fiber photometry system. This combination allowed us to monitor ultrasound-evoked responses in striatal neurons in awake and freely-moving animals. Together, these devices allow for a high resolution analysis of ultrasound-evoked biology at the level of neural circuits and for analyzing behavior in freely moving animals, critical to providing a mechanistic understanding of ultrasound neuromodulation.

4.2 Introduction

Ultrasound has been successfully used to modify targets within the mammalian brain. At high intensities, it can ablate tissues [127] for treating cancer [128] and other neurological conditions like epilepsy [129, 130]; when combined with contrast agents it can open the blood-brain-barrier [131, 132] and deliver small molecule drugs [133, 134] or viral vectors [134]. In contrast, ultrasound at lower intensities can directly modulate neuronal activity [135–137]. Moreover, ultrasound has been shown to both activate and inhibit neurons [130, 138–142], and have differential effects on excitatory and inhibitory neurons based on stimulus parameters [143]. Not surprisingly, the mechanisms underlying in vivo ultrasound-evoked neurostimulation remain unclear, but may include thermal- [144], mechanical- [145], auditory- [82, 146], or cavitation- [81] driven effects. Thus, despite the promise of fully non-invasive ultrasound-based neuromodulation, additional efforts are needed to establish the underlying mechanism, particularly within the mammalian brain.

Electrophysiology with its excellent temporal resolution is the preferred method for studying neuronal function [147]. However, using this method has limited use in vivo. While intracellular recordings can be made from a maximum of only a few individual cells [148–150]; extracellular recordings measuring activity from multiple cells lack cellular specificity [147]. Moreover, recording devices for measuring electrical signals from hundreds or thousands of neurons need to be miniaturized to reduce tissue damage [151]. In contrast, whole-brain imaging techniques like fMRI have contributed to how neuronal circuits responding to external stimuli are distributed across large brain [152, 153], these have limited spatial and temporal resolution. One solution to these problems has been to combine two-photon microscopy with fluorescent reporters, where neuronal circuits can be probed at cellular resolution in an intact brain [154, 155]. Moreover, genetically encoded calcium indicators can be targeted to specific cell populations, whose activity can then be optically monitored at cellular and even sub-cellular resolution [156–158]. While two-photon microscopy has been used to visualize ultrasound-evoked blood brain barrier opening [159, 160], it has been challenging to combine this approach with neuromodulation.

A second method to monitor fluorescent signals uses an implanted fiber optic cannula [161, 162]. Though invasive, this method (fiber photometry) is well-suited to record neural activity across cell populations in freely-moving animals [163]. In addition, fiber photometry can also be

used to record signals from multiple locations in the rodent brain [164, 165]. Moreover, the result is an aggregate of calcium changes from many neurons and cannot be easily resolved, but provides a complementary approach to microendoscopic or two-photon imaging [166]. Combining ultrasound stimulation with these two imaging methods would provide insights into the mechanisms underlying ultrasound-evoked neuromodulation.

Here, we use optically transparent piezoelectric transducers to enable two-photon imaging of neurons in the rodent visual cortex experiencing ultrasound stimuli. We also develop a new, lightweight ultrasound transducer that can be mounted on the head of a freely moving animal and integrate this device with a fiber photometry system. This setup allows us to monitor calcium signals from striatal neurons in moving animals upon ultrasound stimulation.

Results

4.2.1 Two-photon imaging of ultrasound-evoked activity in visual cortex

Conventional ultrasound transducers are bulky and heavy (> 100 g) making them unsuitable for integration with two-photon imaging. In these setups, an animal is typically head-fixed and the objective is placed within 2-3 mm of an exposed brain region leaving little room for the transducer. Moreover, the device within the path of the laser light needs to be optically transparent in order to not disrupt signal acquisition. We developed an ultrasound transducer that overcomes these spatial and optical limitations and enables easy integration into existing two-photon imaging setups (Fig. 4.1a). The device consists of a 127.86 deg Y-rotated, X-propagating lithium niobate (LN) piezoelectric transducer sputtered with 5nm Ti and 1µm Au with a transparent circular window in the electroding for imaging (see Methods for details) produced by photoresist mask and liftoff. Most researchers use 36 deg Y-rotated LN for thickness mode transducers, but in our case the 127.86 deg LN produces greater performance [13] when used at resonance as a narrowband transducer with minimal backing material. Sized at less than one-half the wavelength of the acoustic wave in the piezoelectric media, the circular window does not affect the acoustic wave generated in the substrate. We expressed the genetically encoded calcium indicator, GCaMP6s in V1 visual cortex and monitored responses of parvalbumin (PV) positive interneurons to a variety of ultrasound stimuli (Fig. 4.1b). Previous studies have shown that ultrasound stimuli ranging from 1 msec to

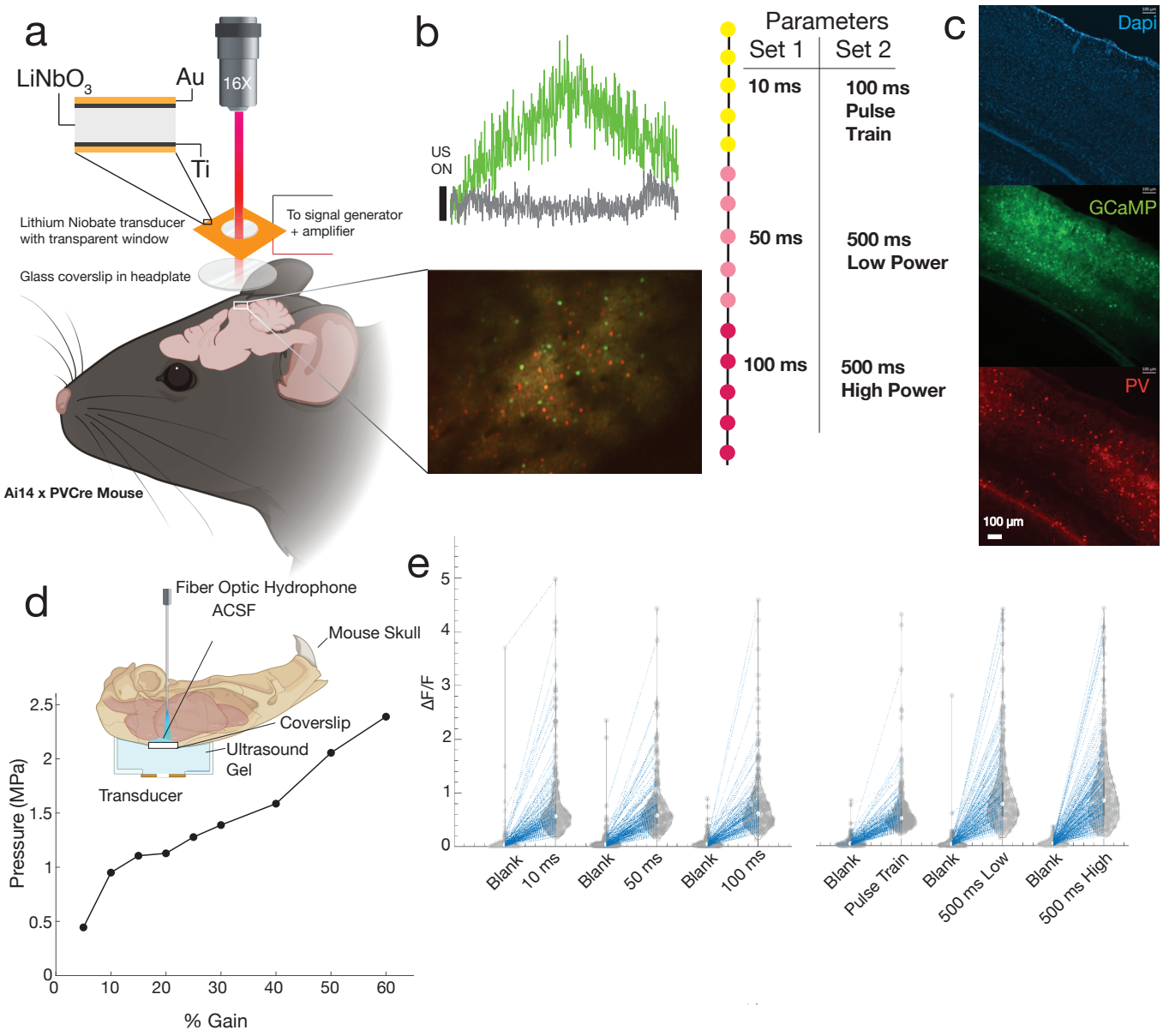

Figure 4.1: Ai14 x PV^{Cre} mice were headfixed on a stage integrated in a two-photon imaging setup with a transparent ultrasound transducer in the optical path **(a)**. A wide range of stimulus durations **(b)** were tested to check for ultrasound-evoked responses in parvalbumin and GCaMP-expressing neurons in V1 **(c)**. The transducers were characterized in an *ex vivo* preparation **(d)** to check pressure outputs in the visual cortex for varying input powers. Calcium traces from individual neurons were identified and responses from different stimulus durations (10 - 500 ms) were shown to be similar **(e)** across all animals tested (n = 3) in this study.

500 ms were needed to achieve neuromodulation in vivo [135, 167]. Consistently, we found that 10 ms to 500 ms of stimuli from a 6.93 MHz transducer was able to activate PV neurons in the rodent V1 cortex (Fig. 4.1c, 4.1d). Moreover, we found similar levels of PV neuron activation for

the various stimulus durations and pressures tested. These results show that ultrasound stimuli drives similar increases in intracellular calcium levels in PV neurons and demonstrate the utility of our transparent device in monitoring changes in fluorescence with single cell resolution within the rodent brain.

4.2.2 A new ultrasound transducer for modulating neural activity in freely moving mice

Most ultrasound applications use lead zirconate titanate (PZT) transducers, which are prone to heating and hysteresis at higher frequencies [38]. In contrast, transducers made from lithium niobate have been shown to have minimal heating and no hysteresis at frequencies typically used for neuromodulation [13, 168]. We started with a micro-miniature coaxial swivel connector (MMCX, Fig. 4.2a) and exposed the central pin and surrounding ceramic insulation using a Dremel benchtop drill (Fig. 4.2b). Next, we added a layer of backing epoxy (Epotek 302, Epoxy Technologies Inc., Billerica, USA) onto the modified connector, leaving the lead tip exposed (Fig. 4.2c). We fabricated a lithium niobate transducer was fabricated (see Methods for details) and soldered it to the device to establish an electrical contact (Fig. 4.2e). This device uses a custom-designed magnetic connector to attach to a matching plate on the animal's head. The magnetic connector is designed to slide onto the device and is anchored in place using a backing epoxy (Fig. 4.2f). The final assembly (Fig. 4.2g) mass is 0.6 g and was characterized for its pressure outputs in an ex vivo preparation as previously described (Fig. 4.2h, ([169])). Ultrasound has been shown to cause heating in target tissues and so we monitored the temperature rise in the striatum using a fiber optic hydrophone and found that this did not exceed 0.1 0C (Fig. 4.2i) during use. In addition, we found that the pressure through the intact skull was between 0.3 – 0.5 MPa (Fig. 4.2k). We also analyzed the vibrational characteristics of this device using laser Doppler vibrometry and found that the fundamental thickness mode's resonance frequency was 6.56 MHz (Fig. 4.2l). This device was then used in combination with fiber photometry probes as described in later sections for analysis of neural activity in freely moving animals.

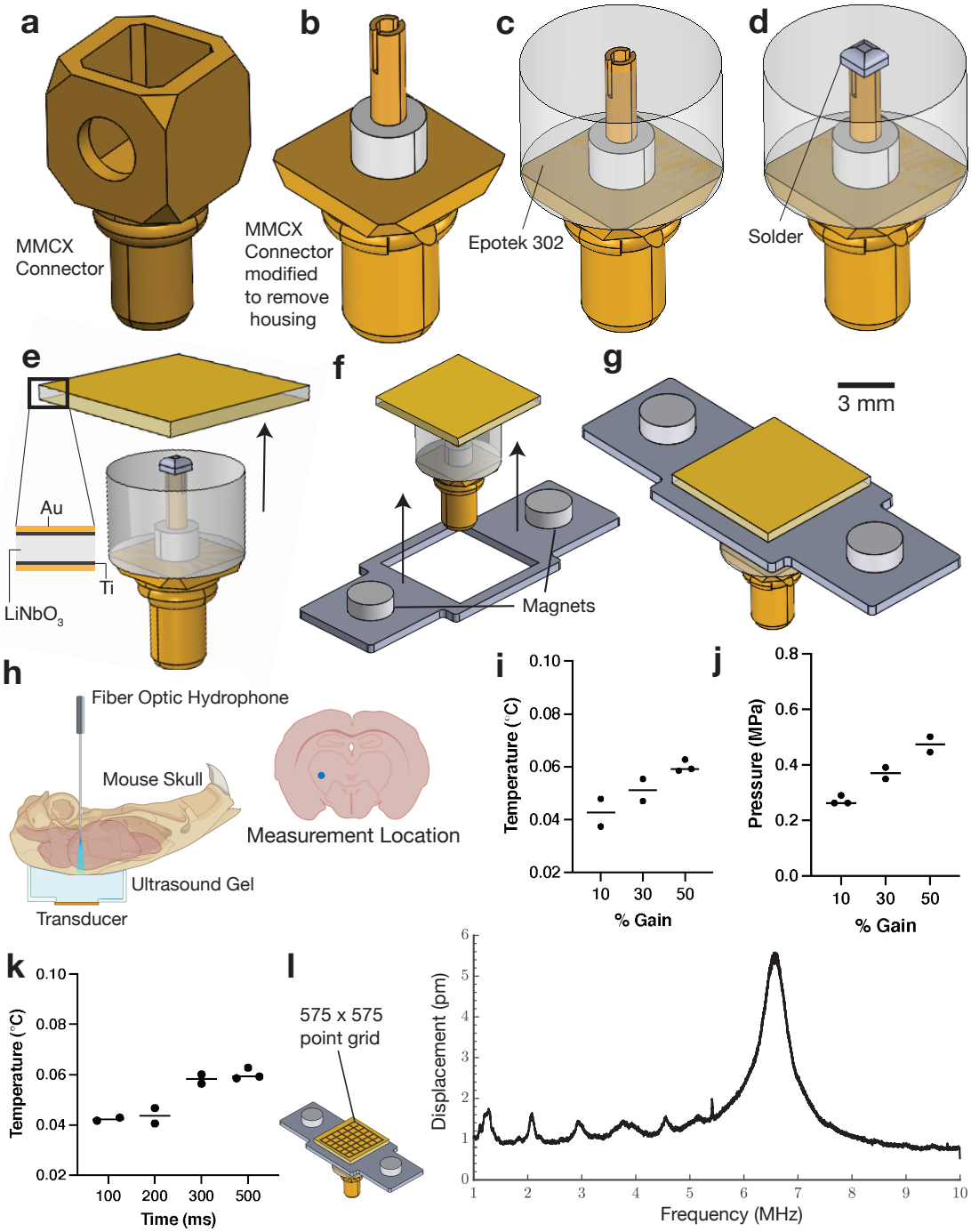

Figure 4.2: Coaxial MMCX connectors **(a)** were chosen for their size and snap-lock mechanism and modified to expose the central lead and ceramic insulation **(b)**. A backing epoxy layer is cast over the exposed connector **(c)**, leaving the tip of the lead exposed. A small bead of solder is placed on the tip of the exposed lead **(d)** and the single crystalline transducer is soldered to the exposed connector lead **(e)**. The device attaches to a headplate implanted on a mouse via a bracket with neodymium magnets **(f)**. The device assembly **(g)** is then characterized to measure pressure and temperature output in an *ex vivo* setup **(h)**. The maximum temperature rise is limited to 0.06°C for pressures of 0.55 MPa **(j)**. The temperature rise did not go past 0.06°C regardless of the time duration of stimulation tested (up to 500 ms, **(k)**). Laser doppler vibrometer scans of the device surface **(l)** were used to characterize the vibration profile of the transducer and determine the thickness mode of operation at 6.56 MHz.

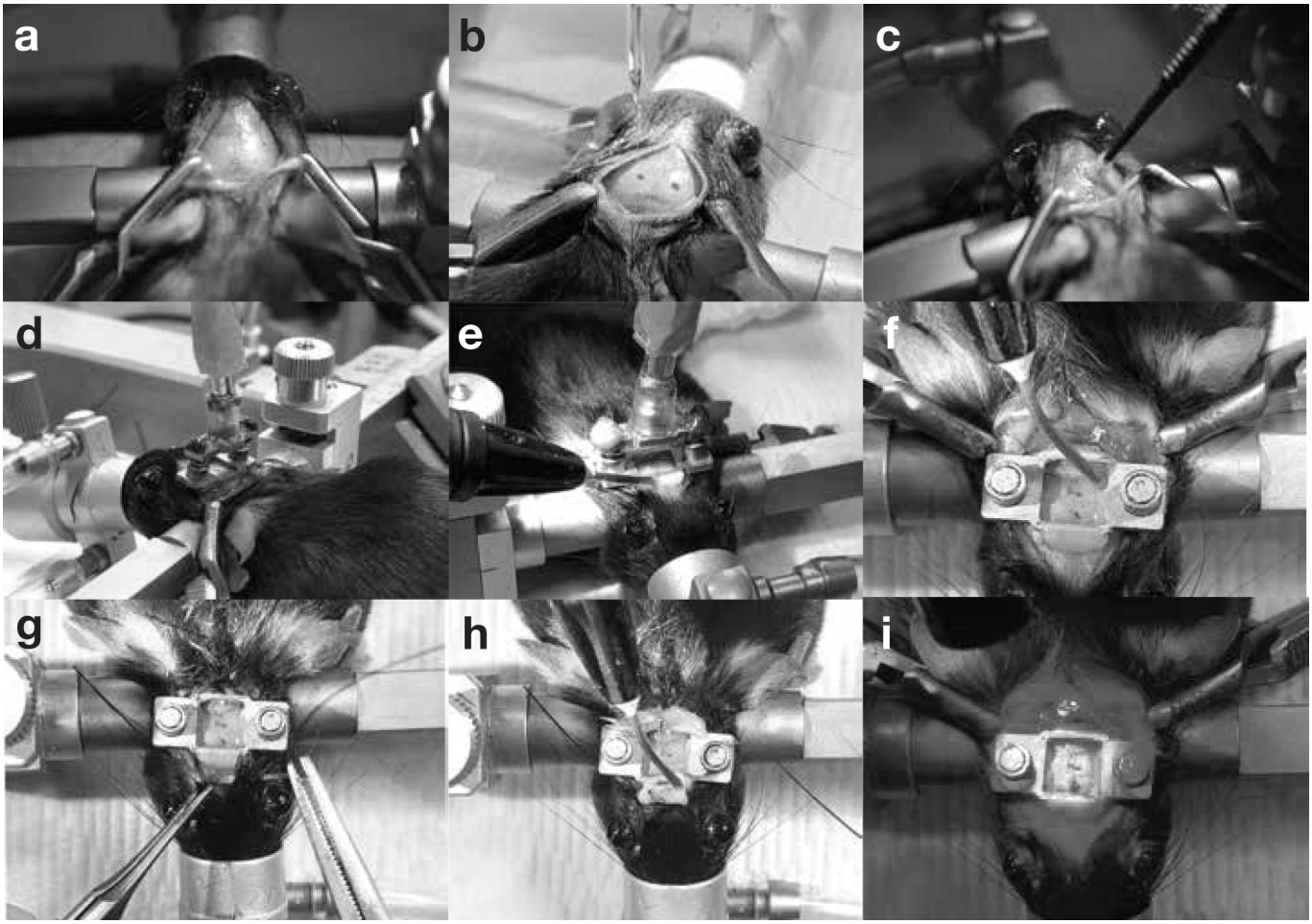

Figure 4.3: Mice are anesthetized using isoflurane and mounted on a stereotax. An incision is made to expose the skull **(a)** and the bregma and lambda structures were identified to perform virus injections **(b)**. The area was cleaned with cotton swabs **(c)** and the MMCX device-headplate assembly was lowered over the injection site **(d,e)**. The headplate was affixed using UV-curable dental cement **(f)** and additional implants (such as fiberphotometry cannulas) were implanted at this stage. The scalp was sutured **(g)** and additional dental cement was dispensed **(h)** at this stage if needed. The exposed skull **(g)** was cleaned using hydrogen peroxide and cotton swabs before returning the mouse to its cage.

4.2.3 Stereotactic placement of device

A mouse brain atlas can be used to target specific anatomical targets using stereotactic protocols [170]. We chose the dorsal striatum as the target brain region due to its stereotactic location, which permits a fiber optic cannula to be implanted without occluding the entire skull. Previous studies have shown that ultrasound-evoked neuronal responses in both cortex and hippocampus [137], but not in more ventral regions of the brain. To test whether a sparse population of neurons could be stimulated, we expressed a genetically encoded calcium indicator, GCaMP6s, in cholinergic

neurons, which are about 2% of neurons in the dorsal striatum [171]. We mounted a ChAT::CRE transgenic mouse on a stereotax under anesthesia (Fig. 4.3a) and injected a floxed virus expressing GCaMP6s (Fig. 4.3b) using a calibrated nanoliter injection system (Nanoject II). The head plate was affixed to the device and the assembly was lowered over the injection site (Fig. 4.3d). Next, the head plate was anchored in place using dental cement (Fig. 4.3e, 4.3f). We then dried the exposed area and implanted a fiber optic cannula as previously described [172, 173]. Finally, the scalp was sutured and additional ultraviolet curable dental cement was used to firmly affix the head plate (Fig. 4.3h, 4.3i). These animals was recovered for two-four weeks prior to conducting studies with the head-mounted transducer.

4.2.4 Ultrasound-evoked activation of striatum in freely moving mice

We used fiber photometry recordings to test whether transcranial ultrasound could evoke calcium activity in freely moving animals. After recovery from the protocol described above (Fig. 4.3), mice were attached to the ultrasound delivery and fiber photometry systems (Fig. 4.4a). We first confirmed that the fiber optic cannula was placed into the dorsal striatum and GCaMP6s expression was restricted to cholinergic neurons in the striatum (Fig. 4.4b). At least three of the four analyzed animals showed significant increases in cholinergic calcium activity upon ultrasound stimulation compared to sham controls (Fig. 4.4c, 4.4d). Next, we tested whether this head-mounted device impaired animal locomotion using both open field and rotor rod assays. We found that animals with the head device had no significant deficit in either distance travelled or average velocity within the first five minutes or over the course of the entire 45-minute testing period (Fig. 4.4e-i). Similarly, we found that these head-mounted mice exhibited similar dexterity in remaining on a rotating rod compared to siblings without the device (Fig. 4.4j-k). Together, these results show that the custom-designed ultrasound device is capable of delivering sufficiently powerful ultrasound to endogenously activate striatal cholinergic neurons in vivo in an awake, freely moving animal, while avoiding the hindering of the animal's movement in an open field or upon a rotating rod.

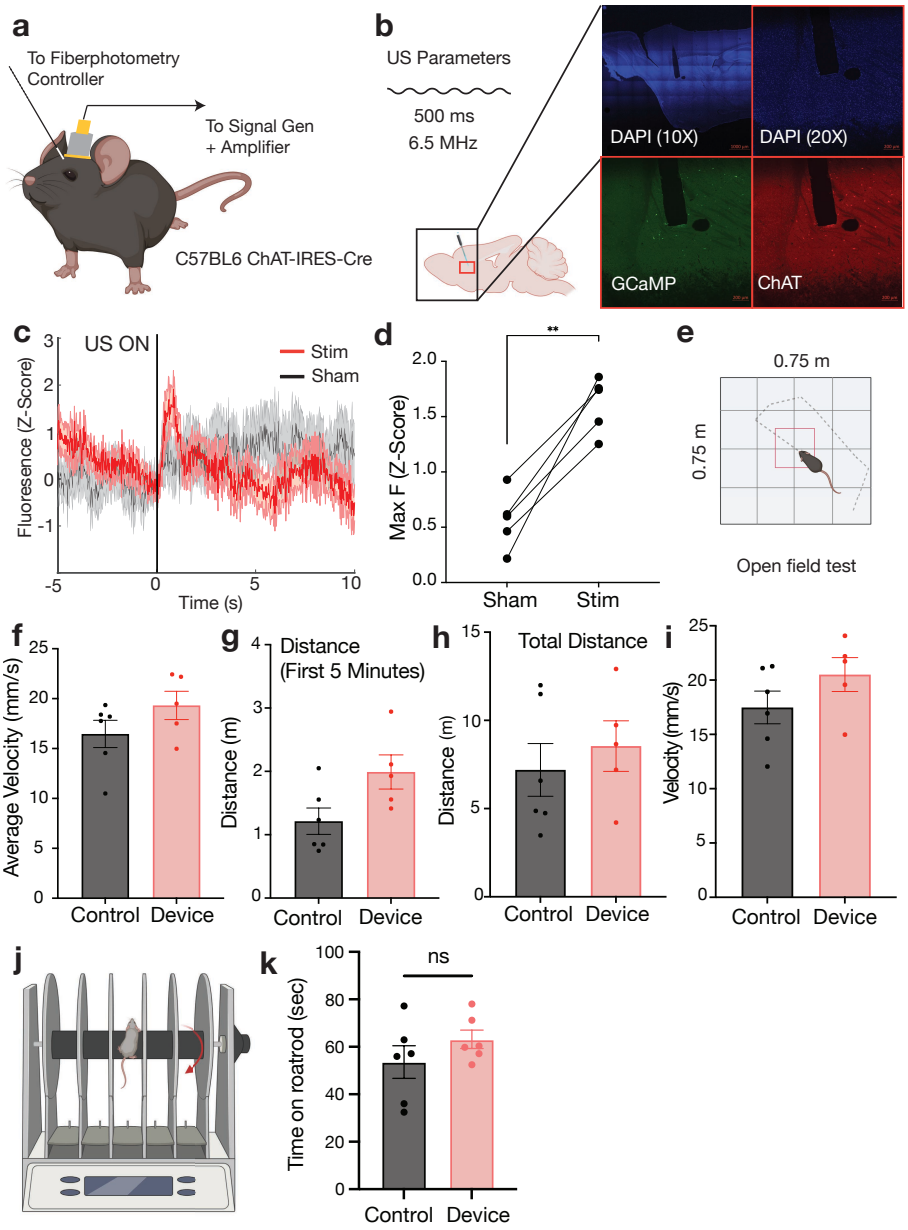

Figure 4.4: Schematic of recording setup **(a)**, with fiber photometry cannula implanted anterior to magnetic headplate holding custom built 6.56 MHz ultrasound transducer on head of ChAT-IRES-Cre mouse. Immunofluorescence confirms fiber photometry cannula (white dotted line) in dorsal striatum, as well as GCaMP6s expression in ChAT+ cells of the striatum **(b)**. Sample average trace of ultrasound ON trials (red) compared to ultrasound OFF (sham control) trials (gray) aligned to onset of ultrasound at time 0 **(c)** show increased fluorescence under stimulation. Maximum GCaMP6s fluorescence in ultrasound trials (Stim) is significantly higher than in Sham conditions across five mice, calculated in the three-second window after stimulus delivery **(d)**. Open field **(e)** and rotarod tests were conducted to assess mobility of the animal with the device. In Open Field testing **(f-i)**, mice connected to the wearable ultrasound device (red) display no reduced locomotion as measured by average velocity in the first 5 minutes, total distance covered in first five minutes, total distance covered in 45 minutes, or average velocity over 45 minutes. Mice outfitted with wearable ultrasound device (red) show no reduction in ability to stay on rotor rod (schematic, **(j)**) as measured by time spent on rotor rod over 5 trials compared to naive controls (gray) with no device **(k)**.

4.3 Discussion

We demonstrate the development of novel methods for integrating ultrasound neuromodulation tools with well-established readout techniques for neuronal activity. Specifically, we show that a transparent ultrasound transducer can be combined with a two-photon imaging system to record responses from PV neurons in a head-fixed animal. Next, we develop a new head-mounted transducer that can be combined with a fiber photometry system to stimulate striatal neurons in a freely moving animal.

We show that ultrasound stimuli ranging from 10 ms to 500 ms can activate parvalbumin positive neurons (PV) in V1 cortical area of the mouse brain, indicating a low threshold for activation of these neurons. Given that PV neurons are approximately 8% of all neurons in the mouse V1 cortical area [174, 175], we are unable to confirm whether ultrasound directly affects this calcium rise or if it acts via one of the other cell types in this brain region. However, PV neurons are critical for a number of V1-driven processes including orientation selectivity [176] and ocular dominance plasticity [177], and we suggest that ultrasound stimuli might be used to probe these process in awake, head-fixed animals. In addition, our transparent ultrasound transducer might also be combined with electrophysiological recordings to provide greater insights into the temporal relationship between ultrasound and activity of PV and other neuronal types in the mouse cortex.

We also designed, fabricated, and tested a small lightweight transducer that be mounted on the head of freely moving mice. This device can deliver stimuli with 0.3-0.5 MPa peak negative pressure in a deep brain region, the dorsal striatum. Specifically, we show that we are able to activate calcium activity in cholinergic neurons without hindering the animal's ability to explore freely or grasp a rotating rod. Moreover, the ultrasound transducer can be removed from the head plates (these are attached using a magnetic connector), allowing the animals to be returned to their home cages and be repeatedly tested, as is commonly done in most striatal-driven behaviors [178, 179]. We used fiber photometry as a readout of ultrasound-evoked neuromodulation, however, recent studies have shown that these data primarily reflect non-somatic changes in calcium and might not correspond to spiking-related activity [180]. Consistently, we suggest that our device can be used to modify neuronal calcium levels in striatal neurons. More broadly, we suggest that this device can be combined mouse genetics to probe the ultrasound and sonogenetic control of neuronal

circuits and behaviors. Collectively, our two ultrasound devices can be used to provide mechanistic insights into how ultrasound affects specific neuronal circuits and their associated behaviors.

4.4 Methods

4.4.1 Ultrasound transducers

Ultrasound transducers used in this study were single-crystal lithium niobate transducers operating in the thickness mode with lateral dimensions of 5x5 mm and thickness 500 μm. The 128YX cut of lithium niobate was used and the fabrication process involved cleaning of the wafer with acetone, isopropyl alcohol, and ultra-pure deionized (DI) water followed by sputtering both sides with an adhesion layer of 20 nm titanium followed by 1 μm gold. The deposition parameters were (with a Denton Discovery 635, Denton Vacuum LLC, New Jersey, USA) $5-10$ nm of Ti at $1.2-1.6$ A/s with the power set to 200 W, with argon as the gas in the chamber at 2.3 mT and the stage rotating at 13 RPM to ensure uniform deposition over the sample. The thickness of gold deposited was 1 μm at a rate of $7-9$ A/s.

4.4.2 Ex-vivo hydrophone measurements

Hydrophone measurements were performed with a fiber-optic hydrophone (FOHS92, Precision Acoustics, Dorchester, UK) *ex vivo*. C57BL/6 mice (JAX 000664), aged 10-14 weeks, were sacrificed and decapitated. The skin over the skull was removed, followed by removal of the lower mandible, soft palate and hard palate. Once the ventral part of the brain was exposed, the mouse head preparation was placed dorsal side down on the diffuser assembly coupled with ultrasound gel, and the hydrophone tip was lowered into the ventral portion of the brain using a micromanipulator. Animals used in this trial were group housed in an American Association for the Accreditation of Laboratory Animal Care approved vivarium on a 12 hour light/dark cycle, and all protocols were approved by the Institutional Animal Care and Use Committee of the Salk Institute for Biological Studies. Food and water were provided ad libitum, and nesting material was provided as enrichment. Mice were euthanized using CO_2 according to approved protocols before decapitation and dissection.

4.4.3 Rotarod Assay

Mouse locomotor behaviour was evaluated on a Rotor-Rod (SD Instruments, San Diego, CA). Mice underwent a single day of training at a constant speed of 3 RPM to acclimate to the Rotor-Rod. The next day, mice were placed on a rod that started at 0 RPM and gradually increased to 30 RPM over a 5 minute period. The latency to fall off the rod was collected. Each mouse underwent 4 trials daily with a 20 minute inter-trial interval in which mice were returned to their cages. The latency to fall off was averaged across the three best trials. This procedure was repeated across 5 days. The experimenter was blinded as to the identity of groups.

4.4.4 Two-photon imaging

Two-photon microscopy was performed with a customized setup incorporating a Sutter movable objective microscope (Sutter Instruments, Novato, CA) with a Ti:sapphire laser (Chameleon Ultra II, Coherent, Santa Clara, CA) at 910nm. The microscope was modified to include a resonant scanner (Cambridge Instruments, Bedford, MA) and data acquisition was controlled with a customized version of Scanbox (Neurolabware, Los Angeles, CA) and collected at 15.49 Hz per imaging plane. We used a 16x, 0.8 NA objective (Nikon Corporation, Tokyo, Japan) for imaging.

Regions of interest were automatically segmented and then manually curated using Suite2P [181]. The manual curation involved removing regions of interest that were incorrectly recognized as cells, particularly at the edges of the field of view. The change in fluoresence was computed by the following equation, where F is the average fluorescence during stimulus presentation and F_0 is the average fluoresence during the pre-stimulus period.

$$\frac{\Delta F}{F} = \frac{F - F_0}{F_0}$$

4.4.5 Viral Injections and Implants

Intracranial injections were performed in a surgery work area under asceptic conditions. Mice were anesthetized via 5% isoflurane induction and held at 1% isoflurane (Somnosuite Kent Scientific, Torrington, CT) throughout surgery on a heating pad and stereotactic frame. After shaving and sterilization, a midline incision into skin to expose the skull was made, and the skull

leveled. For cannula and headplate implantation, the skull was dried and primed with OptiBond primer (KerrDental, Orange, CA). A small craniotomy was made using a surgical drill at the appropriate coordinates. Injections into dorsal striatum were made using a Nanoject III (Drummond Scientific, Broomall, PA) via glass micropipette loaded with virus. Virus was injected at 3 nL/s with 1 s pause until total volume was injected. The micropipette was withdrawn 10 minutes after full volume of virus was injected, after which a 200 μm fiber optic cannula (Neurophotometrics, San Diego, CA) was lowered into dorsal striatum 5 μm above the injection site. Using a minimal amount of light-curable dental cement, the cannula was affixed in place to the skull to provide maximal exposed skull for subsequent ultrasound experiments. For behavior experiments, a custom-designed head plate was also affixed to the skull using dental cement just ventral to the cannula leaving the central portion of skull exposed. Following surgery, the skin was either closed where possible via suture (AD Surgical, Sunnyvale, CA) or VetBond (3M, Two Harbors, MN). Mice were injected with buprenorphine (1 mg/kg) and monitored for at least 3 days post-surgery. Injections were performed unilaterally into dorsal striatum using coordinates +1.0 AP, -2.3 ML, -3.5 DV for vertical injections and +1.7 AP, -2.3 ML, -3.5 DV for injections at 15* on AP axis when leaving more room for headplate for a total of 300 nL. AAV9 hSyn.GCaMP6s.WPRE.SV40 (Addgene #100843-AAV9) was injected into WT mice and AAV9 Syn.Flex.GCaMP6s.WPRE.SV40 (Addgene #100845-AAV9) was injected into Chat$^{IRES-Cre}$ mice.

4.4.6 Fiber photometry recordings

A commercially available fiber photometry system Neurophotometrics FP3002 was used to measure calcium activity in vivo. Briefly, recordings were done by alternating 473 nm and 415 nm excitation light at 80 Hz, for a total of 40 Hz recordings in calcium dependent GCaMP6s and isosbestic (calcium independent) channels, respectively. Excitation power was adjusted to provide 50 uW of light at the tip of the patch cord, calibrated with a fiber optic power meter (PM20A, ThorLabs, Newton, NJ). For anesthetized recordings with the larger device, mice were anesthetized and held at 1% isoflurane, adjusted as needed to maintain sedation on the stereotactic frame without abolishing all measurable brain activity. The skin over the skull was removed and the transducer coupled to the skull with ultrasound gel. For awake, behaving recordings, the mouse was anesthetized briefly to allow for careful attachment of fiber optic cable. After the head mounted

device was attached via magnets and coupled with ultrasound gel, the mouse was allowed to wake up in its home cage and ultrasound stimulations were delivered interspersed with "sham" control pulses.

4.4.7 Immunohistochemistry

Immunofluorescence was collected from free-floating 50μm sections after extended (3 day) fixation in 4% paraformaldehyde or 10% formalin for better visualization of cannula lesion. Sections were blocked at room temperature for 1 hour in blocking buffer (0.2% Triton-X and 10% donkey serum in 1x phosphate buffered saline (PBS). Up to three of the following primary antibodies were then applied for incubation in blocking buffer overnight at 4°C: chicken or rabbit polyclonal GFP (1:250 Aves GFP-1020 or ThermoFisher A6455, respectively) for labelling GCaMP6s positive neurons, goat polyclonal ChAT (1:250 EMD Millipore, AB144P) for labelling cholinergic neurons, chicken polyclonal Parvalbumin (1:250 Encor Biotech, CPCA-PvalB) for labeling PV-interneurons. Following primary antibody incubation, sections were washed three times for 10 minutes each in PBS to reduce non-specific antibody binding effects. Secondary antibodies conjugated to fluorophores 488, 594, or 647 raised in donkey or goat (1:500) were applied for three hours at room temperature in blocking buffer. Nuclei were stained with DAPI (1:1000 ThermoFisher D1306) before washing sections three times in PBS for ten minutes each. Sections were mounted on slides coverslipped with ProLong Gold Antifade Mountant (P10144, ThermoFisher, Waltham, MA) and allowed to dry for 24 hours before confocal imaging (LSM 880, Zeiss, Oberkochen, Germany).

4.5 Acknowledgements

This chapter, in full, has been submitted for publication of the material as it may appear: A. Vasan et. al. (2022) "Ultrasound devices integrating neural activity modulation with two-photon microscopy and fiber photometry " *Proceedings of the National Academy of Sciences.* The dissertation author is the first author of this article.

Chapter 5

Conclusions

The first reports of ultrasound modulating cellular activity were shown in the 1929 on cardiac tissue [79]. Advances in electrical stimulation of tissue and the subsequent invention of the pacemaker in the 1960's resulted in a proliferation of devices that relied on supplying an electrical current to cells to change their behavior. The development of the Hodgkin Huxley model of the neuron[111] around the same time also prompted a view of cellular activity being predominantly an electrical process. The field of ultrasound neuromodulation and sonogenetics has gained attention in the recent past due to potential non-invasive clinical applications they can enable. Although other non-invasive neuromodulation approaches such as transcranial magnetic stimulation exist, they are limited by poor temporal resolution. Optogenetics, a technique that combines light and genetic engineering, is limited to a depth of a few millimeters within tissue. Sonogenetics combines the advantage of non-invasive ultrasound with genetic specificity to target neural circuits. The development of sonogenetics will require building up a library of ultrasound-sensitive ion channels that respond at specific frequencies and pressure thresholds. In parallel, there will need to be developments in transducer design and a better understanding of the biophysical mechanism of action of ultrasound on cells. This will require revisiting the idea that neuronal action potentials are purely an electrical phenomenon and developing devices with novel piezoelectric materials.

The first demonstration of mechanical perturbations accompanying action potentials was observed and quantified in a series of seminal experiments conducted by Tasaki et. al. [85]. Using optical and piezoelectric sensors, they described the displacement of nerve fibers in the nanometer

range [182] that occur in phase with the generation of action potentials. The authors of this work also postulated that the electrical activity of the cell could be brought about by the addition of external stimuli, such as light or mechanical perturbations. This has since been shown to be true [183, 184] and points to the need for a thermodynamic theory of action potential generation that encompasses mechanical and chemical aspects described in past work. Some progress has been made on this front by modeling soliton propagation in lipid membranes [88, 185] but work needs to extend to populations of neurons. Developments in biophysics will need to be accompanied by novel methods of transcranial ultrasound neuromodulation in order to advance the field. Our work in chapter 3 details a plausible biophysical basis for ultrasound neuromodulation by looking into capacitance changes that occur in the membrane when an ultrasound stimulus is delivered. We have also developed high-speed imaging tools that can record this phenomenon at relevant timescales. An extension of this work could involve digital holographic imaging with simultaneous electrophysiological recordings. Combining this technique with fluorescence imaging will also enable the study of how the presence of specific sonogenetic candidates affects membrane deflection and downstream electrical activity.

Ultrasound transducers have historically used lead zirconate titanate (PZT) as a piezoelectric material due to its high coupling coefficient. The downsides with this material are a temperature rise when operated at frequencies and pressures relevant to triggering the generation of action potentials in neurons. Our work in chapter 1 and 2 address key challenges in transducer design. We use lithium niobate, a single crystalline piezoelectric material instead of conventional PZT. Lithium Niobate does not result in a temperature rise in tissue and can typically drive at higher powers than PZT. Recent developments in capacitive and piezoelectric machined ultrasonic transducers may be alternatives but have currently been limited to imaging applications. An additional limitation with these devices is that they typically need to be driven at high input voltages, limiting their ability to be miniaturized. In chapter 2, we address the issue of standing waves withing the skull cavity [33] by borrowing from classical Schröder diffuser designs commonly used in architectural acoustics. We develop a novel excimer laser manufacturing protocol to machine micro-scale pillars in glass and bond this structure directly on lithium niobate transducers. We show that these devices can be used to trigger activity in HEK cells engineered with a sonogenetic candidate and result in similar pressures in different brain regions in an *ex vivo* model.

In chapter 4, we demonstrate the development of novel methods for integrating ultrasound neuromodulation tools with well-established readout techniques for neuronal activity. We show that transparent lithium niobate transducers can be integrated into two-photon imaging systems and evoke responses in paravalbumin-expressing interneurons in the visual cortex. We show ultrasound evoked responses for a range of stimulus durations from 10 ms to 500 ms, indicating a low-threshold for activation of these neurons. We then built a transducer for transcranial ultrasound neuromodulation studies in freely-moving mice. These devices consist of an MMCX connector that has been modified to accommodate a single crystalline piezoelectric material (lithium niobate) and result in minimal heating in deep brain regions while still being able to deliver upwards of 0.5 MPa through an intact skull. We then established a simple surgical protocol that enables researchers to use these devices for long-term behavioral studies. This protocol can be concurrently executed while injecting regions of interest in the brain with fluorescent proteins or implanting fiber photometry probes. Finally, we showed the activation of deep brain regions in freely moving mice using a combination of the MMCX transducer and implanted fiber photometry probes. We show that these lightweight transducers do not hinder movement by conducting open field and rotarod assays. Collectively, these results pave the way for probing circuit-specific activity using transcranial ultrasound stimulation.

Appendix A

Medical Devices for Low and Middle Income Countries: A Review and Directions for Development

A.1 Chapter Abstract

The development of diagnostics and medical devices has historically been concentrated in high income countries, despite a significant need to expand healthcare services to low and middle income countries. Poor quality healthcare extends beyond low and middle income countries to underserved communities in developed countries. This paper reviews diseases and conditions that have not received much attention in the past despite imposing a significant burden on healthcare systems in these circumstances. We review the underlying mechanism of action of these conditions and current technology in use for diagnosis or surgical intervention. We aim to identify areas for technological development and review policy considerations that will enable real world adoption. Specifically, this review focuses on diseases prevalent in sub-Saharan Africa and south Asia: melioidosis, infant and maternal mortality, schistosomiasis, and heavy metal and pesticide poisoning. Our aim with this review is to identify problems facing the world that require the attention of the medical device community and provide recommendations for research directions for groups interested in this field.

A.2 Introduction

A formal search of peer-reviewed articles pertaining to diseases affecting low and middle income countries was performed using Google Scholar and PubMed in order to compile this qualitative systematic review. Keywords used to identify diseases and technologies included, but were not limited to, the following terms: medical devices, low-cost design, global health, low-income countries, low- and middle-income countries, point-of-care diagnostics, neglected tropical diseases, neonatal mortality. The names of specific health challenges in conjunction with other keywords were also used in the search. Identified conditions were compared based upon the number of affected people, disability adjusted life years, and current research carried out to address the condition. The diseases chosen for this review are melioidosis and neglected tropical diseases such as schistosomiasis. These two diseases combined affect over 500,000 people in south Asia and sub-Saharan Africa[186]. This is a fraction of the number of people affected by mosquito-borne diseases[187], but still presents a significant healthcare burden on developing economies. In contrast to, for example, malaria or HIV, these diseases have not received notable attention nor the development of technological solutions toward their treatment. One of the key aims of this review is to expose this unmet need. A section of this review focuses on neonatal mortality, which accounts for over 4 million deaths worldwide and is a significant economic burden due to the number of productive years of life lost[188]. Finally, a section on policy and implementation is provided to aid researchers in identifying useful areas of study.

A.3 Melioidosis

Melioidosis (Whitmore's disease) is an infection caused by the bacterium *Burkholderia pseudomallei* and is prevalent in south and east Asia and northern Australia. In major regions where the disease is endemic, the annual incidence rates are up to 50 cases per 100,000 people[189]. It has been classified as a category B bioterrorism agent by the United States and recent reports indicate that the endemic areas have expanded to southern China, Hong Kong, Taiwan and parts of the Americas[190].

Although healthcare facilities have seen significant improvements over the past few years, reports suggest that diagnosis of melioidosis is only possible in large regional referral centers. This

could lead to a delay in diagnosis and treatment, and an underestimate of the number of people infected with the disease[191]. Diagnosis of melioidosis can be complicated by the presenting symptoms and their similarity to tuberculosis: abscesses in the lungs, liver, spleen and brain stem encephalitis. The bacterium typically infects the host by inoculation onto the skin, by inhalation, or by ingestion. Inoculation onto the skin can cause subcutaneous abscesses, inhalation can cause pneumonia, and the bacterium can reach internal organs such as the spleen, liver, and the lungs through the blood. The most common presentation of melioidosis is pneumonia, with over 50% of cases either occurring through lung abscess or due to septicaemic spread. An additional challenge with melioidosis is that the bacteria, *B. pseudomallei*, is a difficult organism to kill, with studies showing that it is capable of surviving in triple distilled water for years[192]. The disease primarily occurs during the rainy season[193] and people who are in direct contact with wet soil are most vulnerable to the disease. Predispositions such as diabetes mellitus, cirrhosis, and alcoholism, or those who are immunosuppresed increase the risk of contracting the bacterium[194]. Over 50% of patients diagnosed with melioidosis already have diabetes mellitus as a predisposition[195]. This presents a major problem for south Asian countries as the number of patients living with diabetes as an underlying condition is projected to increase by 70% between 2010 and 2030[196]. An additional risk factor is the age group for contracting diabetes mellitus in these countries is 40–60, with reports showing that incidence of melioidosis peaking in this age group, and most countries of this region exhibiting aging demographics.

The recommended treatment of melioidosis involves the intravenous injection of the antibiotic ceftazimide for at least ten days[197]. The therapeutic response to the drug is slow and physicians tend to prematurely switch antibiotics in a considerable number of cases, with the assumption that the bacterium has developed antibiotic resistance. The mortality for a two week administration of the drug is 18%[195]. Although there have been developments over the past 30 years with multiple clinical trials[198–200] in treating melioidosis, the cost of the antibiotics are still high (from US$70–$150 a day[201]), imposing a significant economic burden on developing countries. Simpson, et al., [202] comment on the price of drug regimens used to treat the disease and cite lack of financial support from pharmaceutical companies for diseases prevalent in rural areas as one of the challenges in developing treatment and diagnostic solutions. Melioidosis has been described as “the great imitator” of other tropical diseases such as malaria, typhoid fever, leptospirosis,

and tuberculosis[203]. The varying clinical manifestations of the disease and the multiple affected organs often lead to an incorrect diagnosis. Delayed identification results in the administration of antibiotics that are usually unsuitable to treat melioidosis, which has led to high mortality rates as indicated by multiple studies[203, 204]. It is critical that rapid diagnostic solutions are developed to reduce mortality rates. The most widely used method to detect *B. pseudomallei* is culturing in a modified Ashdown medium with colistin[205], but even this technique may yield inaccurate results, especially in non-endemic areas where the clinical suspicion is low. In cases where there is a positive culture, it may be difficult for commercial systems to differentiate between *B. pseudomallei* and phenotypically similar species such as *Burkholderia thailandensis*[206]. Recent reports highlight not only the limitations of bacterial gene amplification and detection, but also the development of new screening and amplification techniques[207]. Since the sequencing of the complete genome of *B. pseudomallei*[208], several quantitative polymerase chain reaction (PCR) assays have been developed to identify the species[209]. However, it is still a challenge to identify primers that can differentiate *B. pseudomallei* from closely related species.

Clinical laboratories have recently started adopting matrix assisted laser desorption/ionization mass spectrometry systems (MALDI) for the identification of bacterium[210–213], with modest clinical success alongside reports that suggest the databases used mass spectrometry require expansion to accurately identify *B. pseudomallei*. This technique shows great potential to be used as a rapid identification technique but has the limitation of requiring skilled personnel, expensive equipment, and the infrastructure to support them. Low-cost molecular profiling and analysis has been a challenge, and advancements in this field would have a significant beneficial impact on healthcare outcomes in endemic areas. Surface acoustic wave (SAW)-based atomization has been proposed to simplify the sample extraction and filtration process[214]. High-frequency SAW-based atomization was used for the formation of micrometer scale droplets of cell lysate, and the purification step was achieved by loading the sample on a porous membrane placed in the direction of propagation of the surface acoustic waves.

Since the main cause of melioidosis spread is through soil during the rainy season, analyzing soil for the presence of *B. pseudomallei* would prevent infection and hospitalization. Environmental samples are difficult to purify via PCR due to the typical presence of a diverse species of bacteria and fungi. Development of better enrichment and purification techniques would enable an increase

in the number of relevant DNA templates for amplification to occur. An alternative to sampling environmental specimens is the analysis of relevant clinical samples—blood and sputum[215, 216]. The sensitivity of PCR-based techniques is high for sputum and pus, but, by contrast the sensitivity for blood samples is quite low[217, 218].

There may be as many as 165,000 cases of melioidosis every year with an estimated 89,000 deaths[219]. The most commonly used technique for identification, bacterial culture, is 100% specific but has low sensitivity. Slow or incorrect diagnosis results in a significant burden on healthcare systems and can be fatal. MALDI-TOF mass spectrometry is increasingly being used as a rapid and accurate technique to identify isolates[220, 221], though significant challenges to its adoption remain but likely can be addressed by further research in this field.

A.4 Heavy metal and organophosphate contamination of water

This section details the risks associated with poisoning due to metals, such as lead and cadmium, and associated detection techniques. Additionally, we consider the effects and detection of environmental pollutants arising from intensive agricultural and industrial practices. Evidence of the toxicity of lead has been documented in studies conducted as early as 1914[222] and studies demonstrating the adverse effects of lead on attention, childhood development, and neurological disorders were established in the 1970's[223]. Lead poisoning has been shown to impair cognitive ability and social function[224].

The toxic properties of lead are partially due to its ability to compete with calcium at a cellular level, for neuronal signalling[225] and in inhibiting calcium influx into cells[226]. The neurological effects are due to its inhibitory impact on stimulated neurotransmitter release[227, 228]. At high doses, lead can inhibit myelin formation and compromises the integrity of the blood brain barrier. Children are more sensitive to lead than adults due to increased hand-to-mouth activity and increased absorption in the gut. The acceptable thresholds for lead in blood have drastically changed since the 1960's in the United States, from 60 μg/dℓ to essentially recognizing that there is no safe level of lead exposure, with amounts under 5 μg/dℓ having been shown to adversely impact learning [229]. Significant reduction in lead exposure in the U.S. has been achieved by eliminating lead in gasoline and paint, but lead contamination of water remains a problem without

a commensurate level of attention [230]. The decision in 2014 by the city of Flint to change its primary source of water saw lead levels in water rise to as much as 1000 μg/dℓ in some cases[231], with lasting healthcare implications. The only medical treatment for lead exposure is chelation[232], but chelating drugs may not be available in low and middle income countries (LMIC) and in lower income regions of even wealthy countries. In any case, they are not very useful to treat chronic exposure.

Another heavy metal that has adverse health effects is cadmium, commonly used in the electronics industry in batteries and circuit boards. Chronic exposure to cadmium results in accumulation in the kidneys that eventually leads to renal damage[233]. Cadmium can also be absorbed by plants more readily than other heavy metals, presenting another mode of uptake in regions contaminated with industrial waste. The number of people worldwide affected by heavy metal poisoning is difficult to estimate due to the varying sources of poisoning but, given that incidents like the one in Flint that occurred in a developed country with safeguards in place to prevent lead poisoning, there is a need to estimate atmospheric and water-based heavy metal exposure risks across the world.

The daily per-capita supply of calories has increased by over 30% over the last 50 years[234], and as this demand increases, there has been a push towards maximizing agricultural productivity. Increasing agricultural yield has been possible, in part, by the increased use of pesticides. The food and agriculture organization of the United Nations defines pesticides as growth regulators and include substances that can prevent harm to crop during or after harvest[235]. Exposure to pesticides may occur through direct means through occupational exposure or via indirect means through drinking water, dust and food. The World Health Organization (WHO) estimates that 3 million severe pesticide poisonings occur annually and that at least 300,000 people die as a result of exposure, with 99% of these cases being from LMIC's[236]. The effects of pesticide exposure are wide ranging: chronic diseases such as cancer and developmental disorders[237], immunosuppression, hormone disruption, diminished intelligence, and reproductive abnormalities[238]. Of the various classes of pesticides in use today, organophosphate pesticides have been shown to cause substantial morbidity and mortality[239] but still account for over 25% of fertilizer produced[240, 241]. Organophosphates are readily absorbed through the skin, the gastrointestinal and respiratory tracts. The mechanism of action is by inhibition of acetylcholnesterase, which promotes the production of the neurotransmitter

acetylcholine[242]. Overstimulation of nerves due to excess acetylcholine results in autonomic dysfunction, involuntary motor movements, and respiratory depression. Long-term exposure has been shown to result in carcinogenicity[243]. Many farmers in developing countries are exposed to pesticides due to unsafe storage and handling practices, a lack of protective equipment during spraying, or chronic exposure to contaminated soil and water. Although there have been attempts to implement safe handling practices[244] and reduce pesticide use, there is a need to develop protective equipment that can be deployed in developing countries to prevent exposure alongside devices that can detect the presence of harmful pesticides in the local environment.

There is a furthermore a need to monitor the presence of heavy metals and organophosphates in water supplies and in soil, particularly in regions of significant industrial or agricultural output. Paper-based microfluidics was first reported by George Whitesides' group[245] and has the advantage of being inexpensive, readily available, and can wick biological fluids without active pumping. A recent point-of-care paper diagnostic assay for the detection of lead and mercury in water was developed by Lewis, et al.[246]. The device consists of hydrophobic regions that define where the fluid travels through capillary action. The assay is designed in such a way that the time taken for the fluid to travel from one part of the chip to another is indicative of the concentration of the analyte. This is accomplished by the use of glucose oxidase or streptavidin which inhibit flow depending on analyte concentration. It has not been determined if time-based assays provide quantitative results for a range of users. More sensitive tests to detect the presence of lead in drinking water have been developed, with one group reporting a four-fold increase in sensitivity over conventional lateral flow assays[247]. The increased sensitivity was achieved by conjugating gold nanoparticles to a lead-specific monoclonal antibody (Anti-Pb(II)-ITCBE). Organophosphate detection schemes have been considered due to their historical use as chemical warfare agents[248], though there has been a lack of development in the detection of trace amounts of organophosphates, despite knowledge they pose a significant health risk.

A.5 Neonatal mortality

As of 2005, about four million babies die in the neonatal period (the first four weeks of life) and a similar number of babies are stillborn[251]. A majority of these deaths are in low-income and

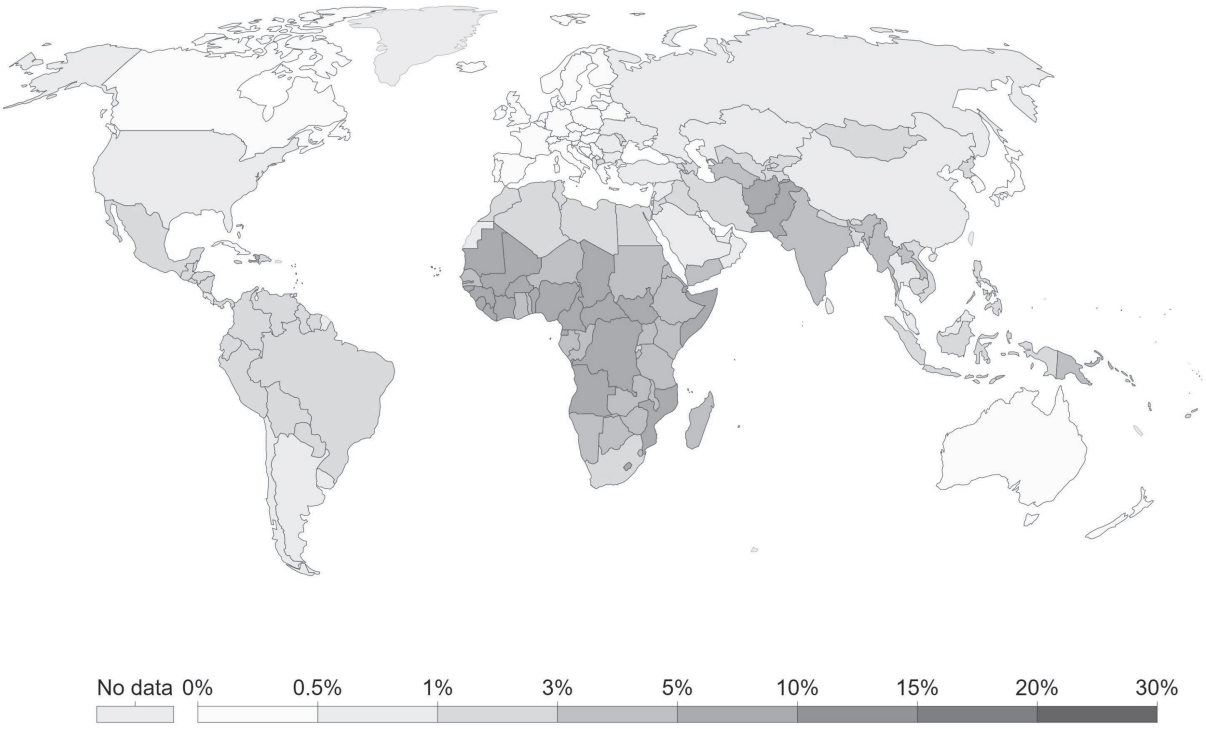

Figure A.1: Infant mortality rates in 2017.[249, 250]. Neonatal mortality is double the global average in sub-Saharan Africa.

middle-income countries in Africa and southeast Asia[252] as illustrated in Fig. A.1. Some estimates show that 38% of all deaths in children under the age of five occur within the first month of life[252]. Assessment of the cause of death is difficult due to a lack of data collection in LMIC's, but estimates indicate that complications arising from asphyxia, severe infections, and preterm births being the main causes of death[251]. The WHO defines birth asphyxia as the clinical description of a newborn that fails to initiate or maintain regular breathing at birth[253]. This term applies to a clinical condition and is not a specific cause of death. Advanced resuscitation is needed for less than 1% of babies at birth and babies that typically require advanced resuscitation by intubation typically require a neonatal ICU to recover[254, 255]. These are typically not available in regional hospitals in LMIC's. Basic resuscitation, however, which only requires bag and mask type ventilators are easy to implement for cases where intrapartum breathing assistance is required. Published guidelines vary on when to provide resuscitation[256], but the WHO recommends resuscitation in cases where the baby does not cry, breathe at all, or is gasping for 30 seconds[253]. It is crucial that these guidelines become widely known, as there is potential for adverse affects such as upper airway damage if respiratory support is provided to healthy babies[257]. Existing devices in use in low-resource settings include mucus extractors with one-way valves and rubber bulb suction devices. The key downside of these devices is that they present an infection hazard for both the neonate and the healthcare provider[258], alongside the potential risk of hypothermia in prolonged resuscitation of a neonate[259, 260], and asphyxia. However, asphyxia may be overcome with expanded care and improved healthcare provider training, but it is crucial that clear protocols for resuscitation be established first.

Congenital abnormalities[251] likewise receive less attention than other medical conditions, especially given that they account for 7% of all neonatal deaths. One of the most common abnormalities in neonates is *spina bifida*, which results from the failure of fusion of the caudal neural tube. A large percentage of cases can be prevented by folic acid supplementation as long as the condition is diagnosed[261]. The underlying cause of the condition is not known but it has been established that women with pregestational diabetes or a high body mass index are at an increased risk of having a child with spina bifida. The protein α-fetoprotein (AFP) and ultrasound can each be used to identify fetuses that have the condition[262]. Point-of-care testing of AFP would enable screening and potential early detection of spina bifida and allow the patient to seek further medical

care in a primary setting. The typical values in maternal serum are under 100 ng/mℓ until 13–18 weeks of gestation[263]. A quantum-dot based sensor for the detection of AFP has been reported by Yang, et al. [264], with sensitivities to 1 ng/mℓ. This test however, relies on comparing the relative fluorescence intensities of the sample with a control, and can be difficult to interpret in the absence of optics and skilled personnel. The WHO compendium of medical devices and technologies for low-resource settings lists two ultrasound scanners, which are priced at US$24,000 and US$7,500 [265], still a significant cost in comparison to the annual budget of many hospitals in low resource settings[266].

Ultrasound is otherwise commonly used to diagnose congenital structural defects during pregnancy. One such condition typically diagnosed using fetal ultrasound is hydrocephalus, a condition where fluid accumulates in the ventricles within the brain. The treatment for this condition involves the implant of a shunt that drains away excess cerebrospinal fluid into the abdominal cavity. The problem with this procedure irrespective of the setting—whether in an LMIC or a high-income country—is that implanted shunts fail due to an obstruction caused by glial and inflammatory cells[267]. A comparison between an inexpensive shunt developed and used in Africa and one currently in use in the United States to treat the condition showed that there was no significant difference in clinical outcomes[268]. The failure rate in the first two years for implanted ventriculoperitoneal shunts remains high, at over 40%[269], indicating that there is a need to evaluate failure due to occlusion in greater detail.

A.6 Neglected tropical diseases

Neglected tropical diseases (NTD) are a group of thirteen bacterial and parasitic infections that affect around 2.7 billion people worldwide[271] as illustrated in Fig. A.2. They are highly prevalent in sub-Saharan Africa and south Asia, where over 70% of the population lives on less than $2 a day[272]. These diseases make it difficult for people affected by them to rise out of poverty as their effects can be chronic or, in some cases, fatal. Schistosomiasis is such an NTD, affecting 192 million people in sub-Saharan Africa alone, accounting for 93% of the world's cases, and associated with increased HIV transmission[273]. About 75% of the population of sub-Saharan Africa lives near bodies of water that have been contaminated with schistosomiasis hosts[274], with those living

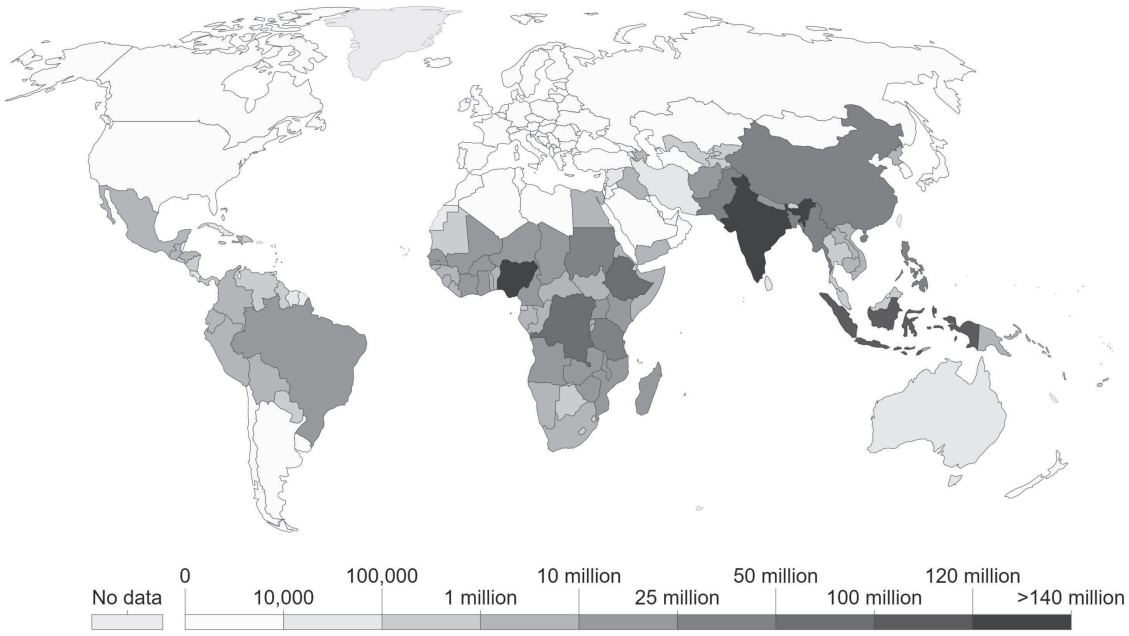

Figure A.2: Number of people requiring interventions for neglected tropical diseases in 2015. These data is a subset of the number of people at risk for NTDs[270].

near dam reservoirs at higher risk[275]. The population most affected by schistosomiasis is children and young adults.

Schistosomiasis can be caused by two strains of bacterium, one of which affects the urinary tract and the second infecting the intestine. *Schistosoma haematobium* is one of the leading causes for urinary tract infections, and around 150,000 deaths annually[276]. *Schistosoma mansoni* causes bowel ulceration and an estimated 130,000 deaths[277]. Adult male and female worms can live in the human host for an average of ten years and the disease spreads by the transmission of eggs to an intermediate snail host typically found in water bodies. The worms feed on glucose present in blood and erythrocytes and excrete waste into the blood stream. Biomarkers present in waste may serve as a target for detecting schistosomiaisis. The primary treatment for the disease is the drug praziquantel, which is only effective against mature worms[278]. Prolonged treatment for 3–6 weeks is required to completely cure the disease. Although this drug is being employed in the field to treat schistosomiasis, the mechanism of action is still unknown and side effects include abdominal pain and passage of blood in the stool[279]. The current diagnostic standard for schistosomiasis is the presence of viable eggs in urine or fecal matter, but the test has a low sensitivity[280]. The three recommended detection techniques by the WHO are microscopy, a urine-based dipstick assay[281], and the Kato-Katz fecal examination[282]. The Kato-Katz method was developed in the 1970's and uses a cardboard cutout over a glass slide and microscopy to easily count the number of eggs in a sample and quantify the number of eggs per unit weight but this technique, like the others recommended by the WHO, lack sensitivity.

A point-of-care lateral flow assay to detect the presence of circulating cathodic antigen was developed[283], addressing the sensitivity limitations of the Kato-Katz technique, but only for *Schistosoma mansoni*. It did no better than the Kato-Katz technique when used for stool samples. Recent reports on diagnosis of the disease have called for better diagnostic tools[284], one of which is PET (positron emission tomography) imaging. This group made use of glucose intake of the worms *in vivo* to detect and quantify their presence using a PET scanner. With groups starting to develop handheld PET scanners[285], this might present a novel research direction for groups looking to develop diagnostic technologies. PCR-based techniques have also been developed to analyze cell-free parasite DNA in human plasma[286], and the development of microfluidic PCR based systems[287] for schistosomiasis could lead to improved detection.

Control measures against the disease include preventative therapy using praziquantel[288], issued by schools screening and treating children for this and other diseases. An additional screening technique that has been attempted in the past is to monitor and eliminate snails that serve as intermediate hosts. The WHO in 2012 pledged to control the morbidity caused by the disease by 2020 and eliminate it as a public health problem by 2025, leading to an increased effort in diagnosing and educating the communities most affected by the the disease. This has stimulated increased funding and opportunities for novel interventions.

A.7 Policy and implementation

There have been significant improvements in healthcare outcomes over the past few decades due to a combination of efforts by public and private organizations, and technological advancements in diagnostics and surgical devices. Despite this, there are some limitations to adoption and implementation of technology.

In some cases, the underlying disease or condition may not have a device or diagnostic solution. This is common in the case of neglected tropical diseases that are a significant health burden but have seen insufficient investment from the private sector. A point of care monoclonal antibody based dipstick for urinary schistosomiasis was developed by a Ghanian group in 2004[289] but has not been commercialized[290].

The technology may exist, but other problems such as distribution or energy required to power the devices may not exist[291]. Oxytocin is used to reduce the risk of post-partum haemorrhage but requires refrigeration, unavailable throughout the day in resource-limited settings. Advances in packaging that could extend the shelf life of drugs and vaccines would expand access to available care in these cases.

In the case of diagnostics, a more sensitive and specific test may exist but there could be reluctance to adopt it or mistrust in the results it produces due to past misdiagnosis with old technology. Rapid diagnostic tests for malaria have been shown to have superior sensitivity and specificity than the current gold standard for malaria detection, microscopy[292]. But a study found that doctors prescribed anti-malarial drugs—even in the case of a negative test result[293, 294]. Skilled healthcare is crucial to improve surgical outcomes. For example, access to skilled surgeons

for delivery is as low as 40% in sub-Saharan Africa and less than 30% in south Asia[295].

Designing medical devices for LMIC's presents unique challenges not seen in developed markets. The WHO estimates that 70% of medical equipment coming from developed countries does not work in hospitals in developing countries[253, 296] due to lack of trained personnel, limitations with infrastructure, and the lack of spare parts or support for equipment.

It is evident from these examples that research and development of novel diagnostic tools and devices alone is insufficient for adoption. In the context of the conditions presented in this paper, there is a need to develop an effective way to screen for schistosomiasis and melioidosis. The spread of melioidosis starts through soil in the rainy season and the presence of schistosomiasis can easily be detected in fecal matter. A technique to purify samples coupled with existing point-of-care diagnostics would stop the spread of the disease at the source. This can be extended to detect the presence of environmental contaminants such as organophophates and heavy metals. An increase in sensitivity can be achieved if adequate processing is done prior to point-of-care diagnosis. The UN's fourth millennium development goal called for a two-third reduction in neonatal mortality by 2015. Although there has been significant progress towards this goal, there are still four million neonatal deaths every year, predominantly in south Asia and Africa. Developing medical devices specifically for neonatal care and not having to repurpose devices made for adults would enable easier surgical procedures. Better detection schemes for diseases such as spina bifida or hydrocephalus using low-cost ultrasound transducers would prepare doctors better for surgery. It is critical to rethink what low-cost means for such applications, especially considering the annual budget of hospitals in LMIC's. Frugal technologies that can be used repeatedly, can withstand environmental conditions and can be used easily by healthcare workers in target countries should be prioritized.

A.8 Acknowledgement

This chapter, in full, is a reprint of in full, is a reprint of Aditya Vasan and James Friend (2020) "Medical Devices for Low-and Middle-Income Countries: A Review and Directions for Development" *Journal of Medical Devices* 125(20), 205108. The dissertation author is the first author of this article.

Appendix B

MADVent: A low-cost ventilator for patients with COVID-19

B.1 Chapter Abstract

The COVID-19 pandemic has produced critical shortages of ventilators worldwide. There is an unmet need for a rapidly deployable, emergency-use ventilator that retains sufficient functionality to serve patients with severely compromised lung function. Anticipating further waves of COVID-19 infections prior to vaccine development, we have developed and validated a simple, portable, low-cost ventilator that can be rapidly manufactured with minimal susceptibility to supply chain disruptions. This ventilator avoids the safety issues and technical limitations inherent to existing solutions to the current ventilator shortage. Herein, we describe the development and validation of a single-mode continuous, mandatory, closed-loop pressure-controlled time-terminated emergency ventilator. Validation was carried out with certified test lungs at a wide range of compliances, pressures, volumes and resistances to meet U.S. Food and Drug Administration standards of safety and efficacy, and an Emergency Use Authorization is in review for this system. Robust safety controls and alarms complement ventilatory capabilities designed to manage COVID-19 patients with severe Acute Respiratory Distress Syndrome. This novel emergency ventilator design could abrogate the need for rationing ventilators based upon imperfect ethical standards, or resorting to controversial practices such as splitting one ventilator to serve multiple patients. All design

and validation information is provided to facilitate ventilator production even in resource-limited settings from parts likely to remain available despite the current public health emergency.

B.2 Introduction

A key challenge in the battle against the disease caused by the novel coronavirus SARS-CoV-2, COVID-19, is a potential worldwide shortage of mechanical ventilators. The required number of ventilators is projected to significantly exceed capacity, based on the number of patients expected to contract the disease in the United States and the percentage of these likely to require assisted ventilation [297–300]. Adding to this burden is the fact that COVID-19 patients who develop acute respiratory distress syndrome (ARDS) often require prolonged mechanical ventilation [301–304]. Physicians around the world have been forced to make difficult triage decisions on which patients to treat and which to let go of due to inadequate number of ventilators [305, 306]. Adding to the challenges of increasing number of devices, is the complexity and expense of traditional ICU ventilators further aggravated by the breakdown of regular supply chains as a consequence of the pandemic. [307–309]

A pandemic caused by a potentially lethal and easily transmissible [310] viral pathogen like SARS-CoV-2 requires rapid, focused effort in either obtaining or manufacturing sufficient medical equipment to save lives despite the disruption of normal supply chains, difficult working conditions, and regulatory restrictions reasonably imposed in normal times that nonetheless jeopardize progress during a state of emergency. In response to the anticipated COVID-19 crisis, we formed the University of California San Diego Acute Ventilation Rapid Response Taskforce (AVERT) to develop a ventilator with functionality sufficient to safely treat COVID-19 patients with ARDS, while simultaneously shortening ventilator production time and cost to make ventilators available when and where they are needed.

The ventilator design focuses on safe operation and reliable production while addressing the specific needs of COVID-19 patients with ARDS: minimizing part count, cost, and complexity; reducing or eliminating reliance on scarce parts and resources; ensuring viable implementation in different healthcare systems across the world; and seeking simple assembly, testing, and use procedures by healthcare personnel with limited experience in ventilation and no experience with

this type of ventilator system [311].

Modern ICU ventilators provide complex control and intricate feedback loops of a wide variety of respiratory parameters and ventilation modalities. Their operation requires highly specialized staff [312]. Regulatory requirements are understandably high, and pandemic crisis-driven emergency orders of ventilators to medical device manufacturers are difficult to fulfill due to the failure of supply lines and the difficulty in rapidly ramping up production of these technically advanced ventilators. In the meantime, lives are at risk. While several emergency ventilators are commercially available, most do not meet the medical requirements of the complex ARDS-like pneumonia associated with COVID-19 which requires pulmonary protective ventilation with careful control of pressure and volume as compliance of the infected lung tissue can rapidly decrease, placing the patient at elevated risk of barotrauma and further lung injury. We are left with an unmet need for COVID-19 pneumonia-appropriate, rapidly deployable, comparatively simple emergency-use ventilators.

Based on published literature and clinical experience, we determined the following ventilation features to be essential for safe use in patients in this crisis: pressure control mode of ventilation, respiratory rate, inspiratory time, and forward-compatibility with external modular components such as adjustable positive end expiratory pressure (PEEP) valves. [313–315] In addition, basic alarms indicating high and low pressure and volume are necessary to notify the healthcare provider when desired parameters are not being met or if there is a significant problem with the system (e.g. electrical circuit failure). Many modern ventilators can sense and synchronize to patient initiated breaths to provide the most comfortable form of ventilation in a minimally sedated patient. However, we did not include a synchronized mode of ventilation in the design of this ventilator, recognizing that patients with COVID-19 and severe ARDS will require sedation and possibly pharmacologic paralysis to facilitate optimal ventilation. [316, 317] The advantages of this approach include simplified ventilator settings and simplified troubleshooting with a single-mode continuous, mandatory, closed-loop pressure-controlled time-terminated ventilator (from now on referred to simply as pressure-controlled). This approach provides predictable delivery of ventilated breaths, and streamlined device production. Further design choices were based on the dual goals of safe, effective ventilation and quick production as detailed in the next section.

Ventilators in clinical use are regularly calibrated using lung simulators to comply with U.S. Food and Drug Administration (FDA) standards of safety and efficacy. All devices described in

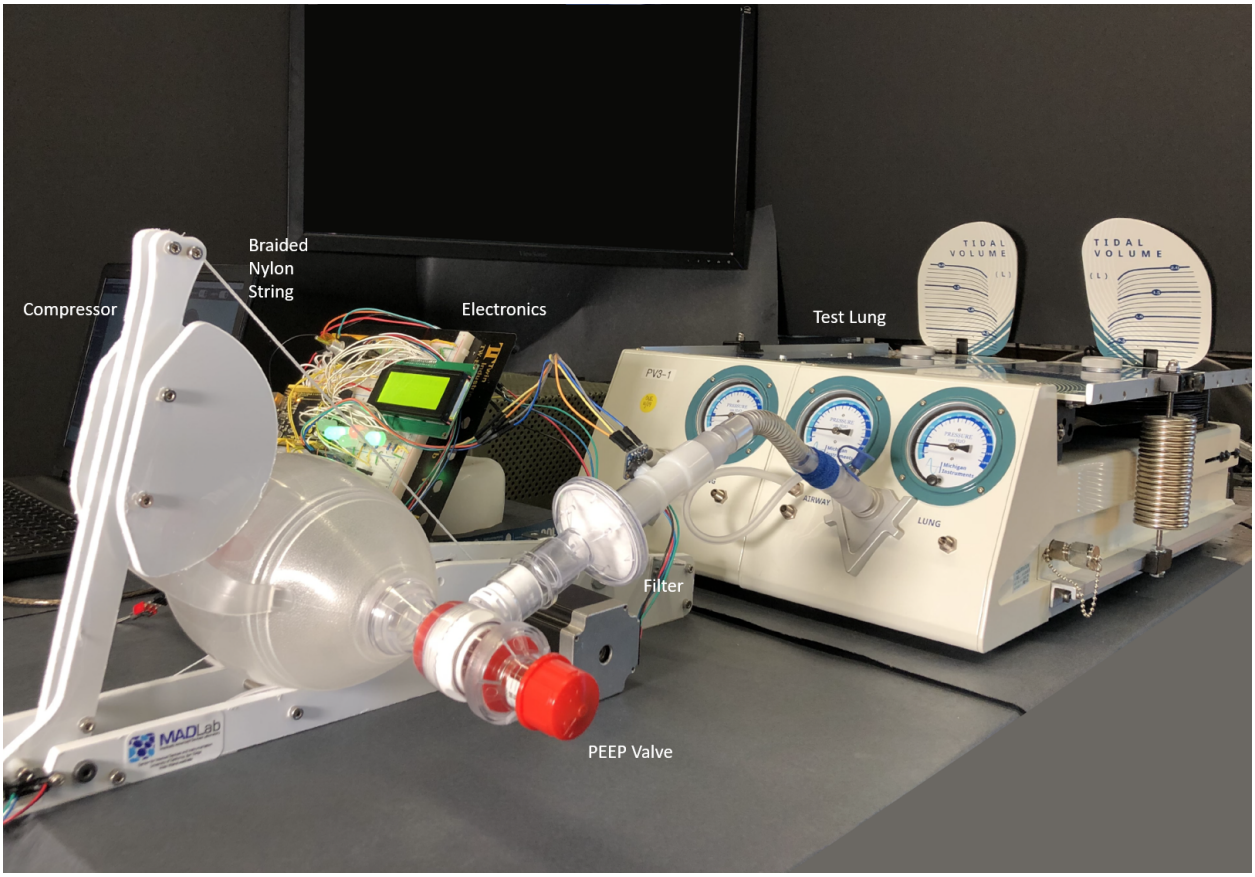

Figure B.1: Testing of the system was performed on the lung simulator. All parameters were tested to their stated limits (over 200 individual experiments) and according to International Standards Organization (ISO) standards for pressure controlled ventilation. Notice that the dead space is kept to a minimum by reducing the length of tube between the bag and the lung simulator; this configuration was reproducible with a full-sized simulator manikin and a standard adjustable overbed hospital bedside table. The system shown here is an early prototype with exposed electronics, but is to be supplied with housings as depicted in Fig. B.2.

this manuscript were tested and verified with such a lung simulator (Dual Adult Test Lung, ISO 13485 certified; Michigan Instruments, 4717 Talon Court SE Grand Rapids, MI 49512 USA) with the associated data visualization software at the University of California San Diego. Our bedrock of safety is the provision to test every one of our devices using this human ventilation simulator, a physical device designed to emulate human respiration with time-stamped data capture to determine the safety and efficacy of the manufactured ventilators.

All models, print files, simulation data, and all other data obtained have been included either in this manuscript or in the Supplementary Information with the recognition that the situation faced

by the medical community is unprecedented and will require a coordinated effort once the design has undergone peer-review by members of the clinical community and Emergency Use Authorization (EUA) by the FDA [318], which we have applied for at the time of writing. Our engineering and clinical teams have closely collaborated to develop a *safe* design that can be quickly manufactured in large numbers in resource-limited settings from parts readily available despite the current public health emergency. We have designed the system to be able to incorporate additional features as necessary, including other mandatory ventilation modes.

B.3 Design of an automated self-inflating bag-based ventilator: MADVent Mark V

Mechanical ventilation typically requires pressure or volume-based control of inspiration at a defined rate [313, 319]. Given the relative ubiquity and simplicity of pressure transducers as compared to flow sensors, the pressure-controlled mode of ventilation was determined to be both safe and best suited to this current project. This has proven fortuitous since, though both volume and pressure limits are included in ARDS recommendations, [315] there are data to support the pressure control mode as being particularly safe in ARDS therapy. [314]

Typically, automatic pressure-controlled ventilation relies on either an impeller motor that pressurizes air within the ventilator or a reticulated, regulated high-pressure source from the healthcare environment. Volume-controlled ventilation relies on the compression of a bag or bellows by a known volume. In order to be truly controlled, each of these methods must measure the pressure or volume—sometimes both—and use this information to appropriately adjust the actuation in a feedback loop. Measuring pressure at the output of the ventilator is far more straightforward, less expensive, and less susceptible to calibration and algorithmic errors than measuring volume. Accurate flow sensors for mechanical ventilation are expensive [320], susceptible to supply chain disruptions, and conversion of their output into volumetric flow rate is difficult [321] with complex algorithms required to deal with the challenges [322]. Air flow is typically integrated over time to estimate the volume of air passed through a ventilator, and the volume-flow relationship is complicated by sensor accuracy [323]; lung compliance [324]; humidity, compression, and temperature [325]; and leaks in the system.

Manual ventilation—and automated ventilators from the past—make use of a bag with valves to ventilate a patient's lungs with mechanical compression and release of the bag. Safe ventilation, however demands care in mechanical compression and release beyond simply compressing a bag. For our ventilator, we adopted a self-inflating bag-based mechanical ventilation system, combining its intrinsic simplicity with instrumented sensing of the pressure produced by the system to continuously control the ventilator in a closed feedback loop, eschewing air flow sensors in favor of calibrated knowledge of how the bag volume varies with mechanical compression. This allows the ventilator to reach precise pressure targets within a prescribed inspiratory time while setting safety alarmed thresholds on the volume delivered per breath in an inexpensive and rapidly devised design.

Rather than reinventing the bag and valving system, we have elected to utilize a self-inflating manual resuscitator bag (SPUR II, Ambu Inc, Copenhagen, Denmark) already in common worldwide use in hospitals and other emergency care settings. These self-inflating bag systems have been designed to deliver the proper range of tidal volumes with simple manual compression, do not require an pressurized gas source, and have the appropriate valves and standard connections to ventilate patients. Other manual resuscitator bags of similar size are compatible with the MADVent system, but may require calibration for safe use of all ventilatory alarms and features. These resuscitator bags are compatible with external PEEP valves that both add no dead space to the system and are essential for the care of patients with COVID-19 and ARDS. They also have built-in ports for supplemental oxygen administration and pressure monitoring. Two pressure sensors were used to measure ambient and in-line pressure (BMP180, Bosch, Schillerhöhe, Germany) but these can be replaced by a single differential pressure sensor (SSCMRRN060MDSA5, Honeywell Inc, North Carolina, USA) that can be mounted on a printed circuit board (PCB). The differential pressure sensor can be connected to the inspiratory line either at the mouthpiece or at the outlet of the bag. The mouthpiece placement option may be preferable for patients requiring very low tidal volumes or with especially poor gas exchange, for whom reducing dead space is crucial. In either case, the sensor is able to provide pressure measurement for the entire breath cycle: inhalation, exhalation, and the idle time between breaths.

The bag is mounted into a frame under a lever arm that is subsequently used to compress the bag, as shown in Fig. B.2. The entire ventilator structure, including the bag mounting frame and arm, can be rapidly laser cut from polyoxymethylene (acetal) in 15 min, and assembled using readily

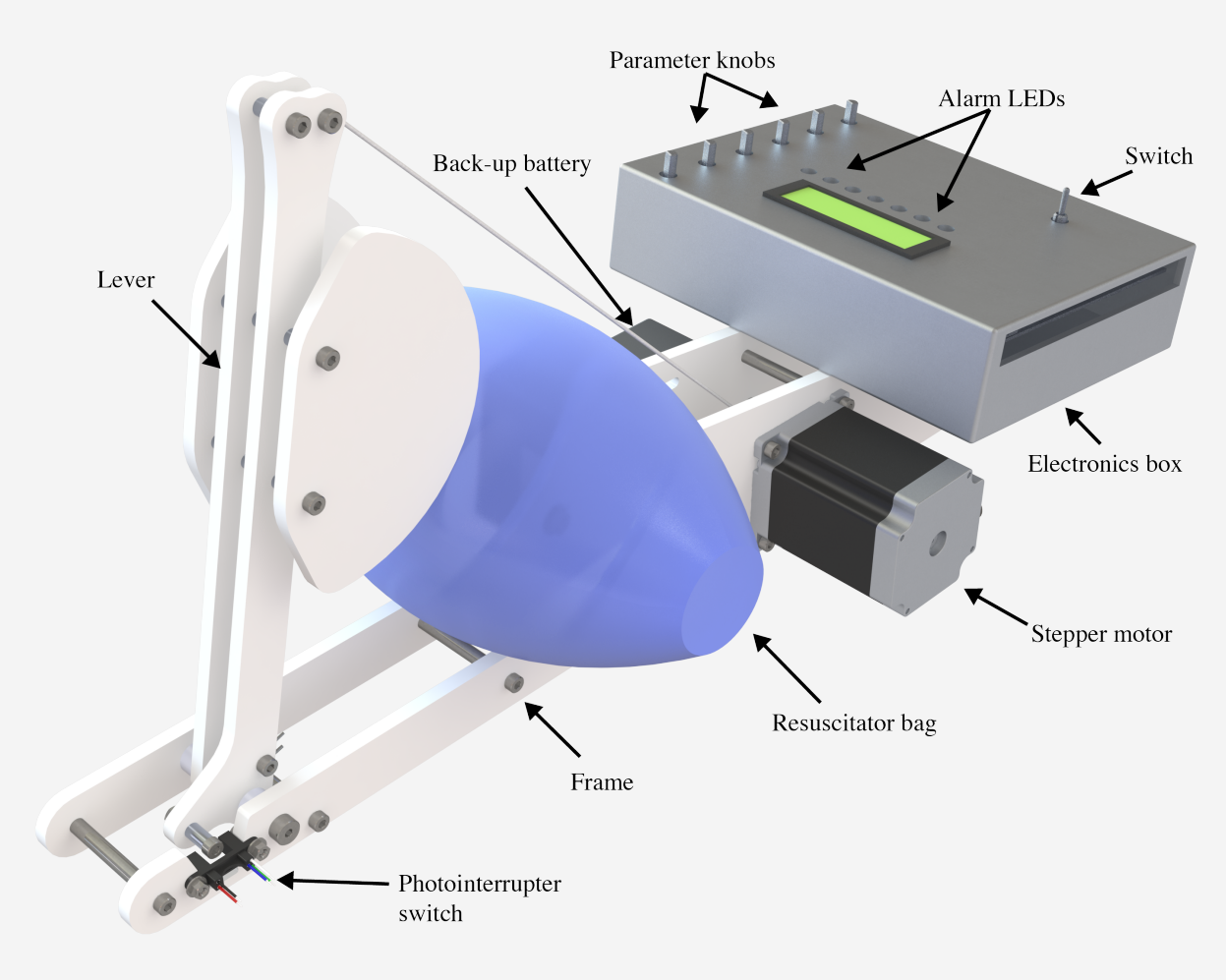

Figure B.2: Render of the final version of MADVent, with an electronics enclosure. The enclosure has an interface for the healthcare provider to adjust various ventilation settings such as target pressure, inspiratory time, respiratory rate and alarm thresholds. An LCD screen displays ventilation parameters in real time. LED's and a built in alarm alert the healthcare provider in the event of an emergency.

available hardware. An alternate material choice is polycarbonate, which has superior resistance to commonly used hospital disinfectants such as hydrogen peroxide and sodium hypochlorite (bleach). Complete design files are provided for the reader (see Supplementary Information). Two convex compressor extensions are mounted on the lever arm and press into contact with the bag held in place by corresponding concave surfaces via hook-and-loop (Velcro) fixtures on the fixed frame of the ventilator, ensuring its stability and maximizing the possible compression volume of the bag. The hook-and-loop attachment facilitates quick and simple bag removal in the event the healthcare provider needs to manually ventilate the patient or the bag needs to be exchanged.

Rather than rely on gear or cam mechanisms to translate the rotational motion of a control motor to a rectilinear motion for bag compression [326, 327], we use the bag compression arm as a lever to provide substantial mechanical advantage from the motor. Geared and cam mechanisms are subject to wear, have backlash, add cost and complexity, and tend to be noisy, a significant issue in the critical care setting. Our approach permits simple direct motor drive via a lanyard attached to the top end of the lever arm and wrapped around a spool attached to the motor's shaft. Lengthening the lever arm or placing the bag closer to the pivot point increases the mechanical advantage.

A stepper motor with 1.89 N-m of holding torque and a maximum rotation speed of 180 rpm (QSH5718-76-28-189, NEMA 23, Trinamic Motion Control GmbH, Hamburg, Germany) was chosen (*see* Supplementary Information for details) in order to supply the rotation power and control necessary to implement a pressure control feedback loop and likewise produce sufficient rotation speed to enable rapid breath cycling. A microstepping commutation scheme was chosen for quiet operation, precision, and the avoidance of resonances. Stepper motors are brushless and therefore can fail only by failure of the bearings or the insulation of the electrical wire within. They feature a mean-time-between-failure (MTBF) of at least 10,000 hours, over a year of continuous operation, and so should not fail in this application for an anticipated four-week lifetime. Supplies of these motors are unlikely to be affected by the pandemic, as they feature in diverse applications from 3D printing to robotics, consumer devices, automobiles, and furniture. The lever arm hinges around a shoulder screw, a type of machine screw characterized by a constant diameter raised portion which is commonly used for simple pivot points, and its lateral movement along this screw is limited by spacers. A torsional spring is mounted at the hinge in order to aid in the return of the lever arm to

its zero position at the end of each stroke, as verified for each cycle by a photointerrupter switch (C14D32P-A3, CUI Devices, Lake Oswego, OR USA). An electronics box is secured to the frame opposite the lever hinge. The system is powered by a universal, medical grade (UL/ISO 60601) 12 VDC wall adapter (90–240 VAC input, SWM30-12-NV-P5, CUI Devices), but a rechargeable lead-acid back-up battery (BP1.2-12-T1, B B Battery, Commerce, CA USA) capable of powering the system for at least 20 minutes is also installed and automatically begins supplying power when needed.

The healthcare provider is able to directly set the following six parameters via control knobs on the system: respiratory rate, peak inspiratory pressure (PIP), inspiratory time, high-pressure alarm threshold, low-volume alarm threshold, and high-volume alarm threshold. The system is capable of delivering between 10 and 35 breaths per minute (bpm), peak inspiratory pressures between 10 and 35 cm H_2O, and inspiratory times between 1 s and 3 s. Volume alarms may be set between 200 cc and 1000 cc. The set values of each parameter are displayed on a liquid crystal display (LCD) screen. Seven light emitting diodes (LEDs) are provided to individually indicate to a clinician the nature of an alarm condition. These include alarms for the high and the low-volume thresholds, as already mentioned, and alarms for mechanical failure, overheating, pressure sensor disconnection or failure, wall power disconnection, and low battery. In urgent situations such as a low or high-volume ventilation condition, a loud buzzer will also alert clinicians. If conflicting or otherwise incompatible parameters are entered, then the relevant parameters flash on the screen and the system will begin ventilation and an alarm will sound immediately. This condition has been programmed to occur in three cases: when the low-volume alarm threshold is higher than the high-volume alarm threshold, when the set peak pressure is higher than the high-pressure alarm threshold and when the user set inspiratory time is more than 75% of the inspiratory time calculated from the user set respiratory rate.

After the parameters have been set, the system waits for activation via a toggle switch before initiating ventilation. During inspiration, the motor rotates an amount proportional to the difference between the intended pressure and the current measured pressure at each time-step. The intended pressure at each time-step is determined by a monotonically increasing function between $p(t = 0) = 0$ and $p(t = t_i) = p_p$, where p is pressure, t is time, p_p is the peak pressure set by the provider, t_i is the inspiratory time set by the provider. Once the peak pressure or the inspiratory time has

been reached, the motor reverses direction at a set speed until it reaches the zero position, which is defined by the compressor arm photointerrupter switch and confirmed by the motor encoder. The system then enters a waiting period calculated according to the set respiratory rate and inspiratory time before beginning the next breath cycle.

If, at any point during the control loop, a single breath cycle generates a volume below the low-volume alarm threshold, then that alarm is triggered. The system identifies the volume expelled in each breath via an encoder fixed to the motor shaft that reports exactly how much the shaft has rotated. A low volume may indicate significantly lower compliance in the patient or an endotracheal tube obstruction. Similarly, if a single breath's volume exceeds the high-volume alarm threshold, then that alarm is triggered, and may indicate a patient becoming disconnected from circuit or another source of a leak in the system. Alarms for pressure are triggered directly from the pressure sensor and similarly can identify issues with lung compliance and circuit integrity.

B.4 Results

To confirm the ventilator's operating and alarm capabilities, it was tested on a lung simulator. Under pressure-control ventilation, the high-volume, low-volume, and high-pressure alarms were all successfully triggered when their alarm set points were crossed, as illustrated in Fig. B.3. For a pressure-controlled system, a high-volume alarm could be triggered by too large of a ΔP (Δpressure = PIP - PEEP), an increase in the patient's compliance, or an accidental disconnect/leak in the inspiratory circuit. This was experimentally demonstrated by slowly increasing the ΔP through PEEP reduction in Fig. B.3A. A low-volume alarm state could be induced by a blockage in the inspiratory circuit, a decrease in the patient's compliance, or too small of a ΔP set by the healthcare provider. This alarm was demonstrated in our system by gradually increasing the PEEP during operation, which gradually lowered the ΔP, and ultimately dropped the tidal volume below the set alarm threshold (Fig. B.3B). The high pressure alarm may be elicited by a patient coughing or "fighting" the ventilator, simulated in our demonstration in Fig. B.3C, potentially indicating insufficient sedation or as a sign of circuit obstruction (along with the low-volume alarm).

In addition to alarms for pressure, the system is equipped with temperature sensors that are mounted on the stepper motor and the motor controller, in order to continually monitor temperature

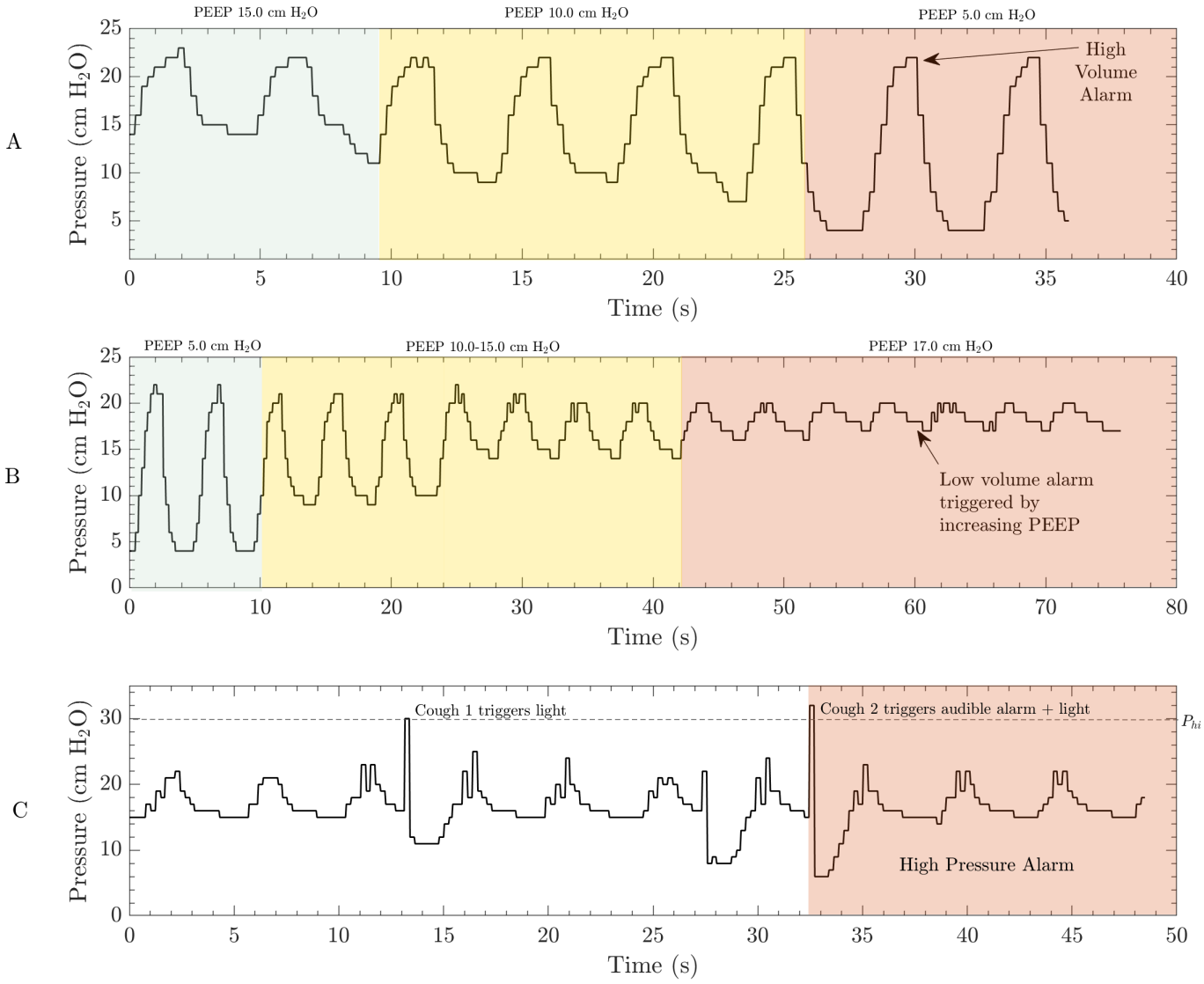

Figure B.3: The MADVent Mark V has alarms for high and low volume that may be set between 200 and 1000 cc. In this example, the system was run at a rate of 13 breaths per minute, a PEEP value of 15 cm H_2O and the compliance on the lung simulator was initially set to 0.03 cc/ cm H_2O. A) The high-volume alarm threshold was set to 500 cc for the first case. PEEP was decreased from 15 cm H_2O to 5 cm H_2O in order to increase the tidal volume delivered to the lung simulator. A high-volume alarm was triggered when the calculated tidal volume exceed the limit set by the healthcare provider. A relevant clinical scenario in this case would be a leak in the inspiratory line leading to an increase in volume delivered without the target pressure being reached. B) The low-volume alarm is triggered once the calculated volume drops below the lower limit set by the healthcare provider. This was simulated by increasing the PEEP up to 17 cm H_2O. A relevant clinical scenario for this case would be the inspiratory line being kinked. C) The high-pressure scenario was simulated by interrupting the expansion of the lung simulator during inspiration to simulate a patient coughing. The high-pressure alarm was set off when the pressure exceeded the set value of 30 cm H_2O.

and alert the healthcare provider if the measured motor temperature exceeds 65°C; these mechanical components are far removed from the ventilatory circuit. An encoder mounted on the shaft and an photointerrupter switch attached to the lever arm serve to detect mechanical faults that may occur during operation.

Though we made the decision to omit flow sensors due to their expense [320] and complexity [328], we still require an accurate prediction of the tidal volume in order to safely provide high and low volume alarms. This is achieved by monitoring the compression of the bag. The volume delivered by compressing the bag is directly proportional to the decrease in cross sectional area, A_i, of the bag as it is compressed by the lever. Thus, if we can relate A_i to the rotation of the motor, then we can predict the tidal volume, V_{tidal}, since we are controlling the rotation of the motor shaft. An exercise in trigonometry provided in the Supplementary Information reveals the relationship between the rotation of the motor shaft, ϕ and the tidal volume produced by the bag, V_{tidal}. This relationship, $V_{\text{tidal}}(\phi)$, is validated in Fig. B.4.

We performed experiments across the full range of ventilation capabilities with four independent parameters, compliance, PEEP, inspiratory time, and peak pressure, and two dependent measurements, tidal volume and motor rotation. Figure B.4 shows that these potentially confounding variables do not have a large effect on the relationship between volume and motor rotation. A quadratic curve was fit to the data (with a coefficient of determination of $R^2 = 0.953$) in order to validate our model. The model generally predicts larger volumes as expected since it does not account for the compliance of the lung and thus should match the higher range of data points. The model assumes two rigid bodies are intersecting, but in reality the lever is rigid while the bag is elastic. As the bag is compressed its shape changes, which accounts for the relative linearity of the fit curve compared with the model.

The volume-rotation relationship described by our model is embedded in the ventilation code so that the volume alarms are triggered correctly without a flow sensor, accurate to a mean value of 5%. It is important to note that manual resuscitation bags with different structure/geometry than the one used in this calibration (Ambu SPUR II, Ambu Inc, Copenhagen, Denmark) will not have identical volume-rotation relationships, $V_{\text{tidal}}(\phi)$, and volume-related alarms will therefore be less accurate without another calibration. We expect this effect to be small since adult-sized, self-inflating resuscitation bags have similar geometries and total volumes. Recall these bags are all

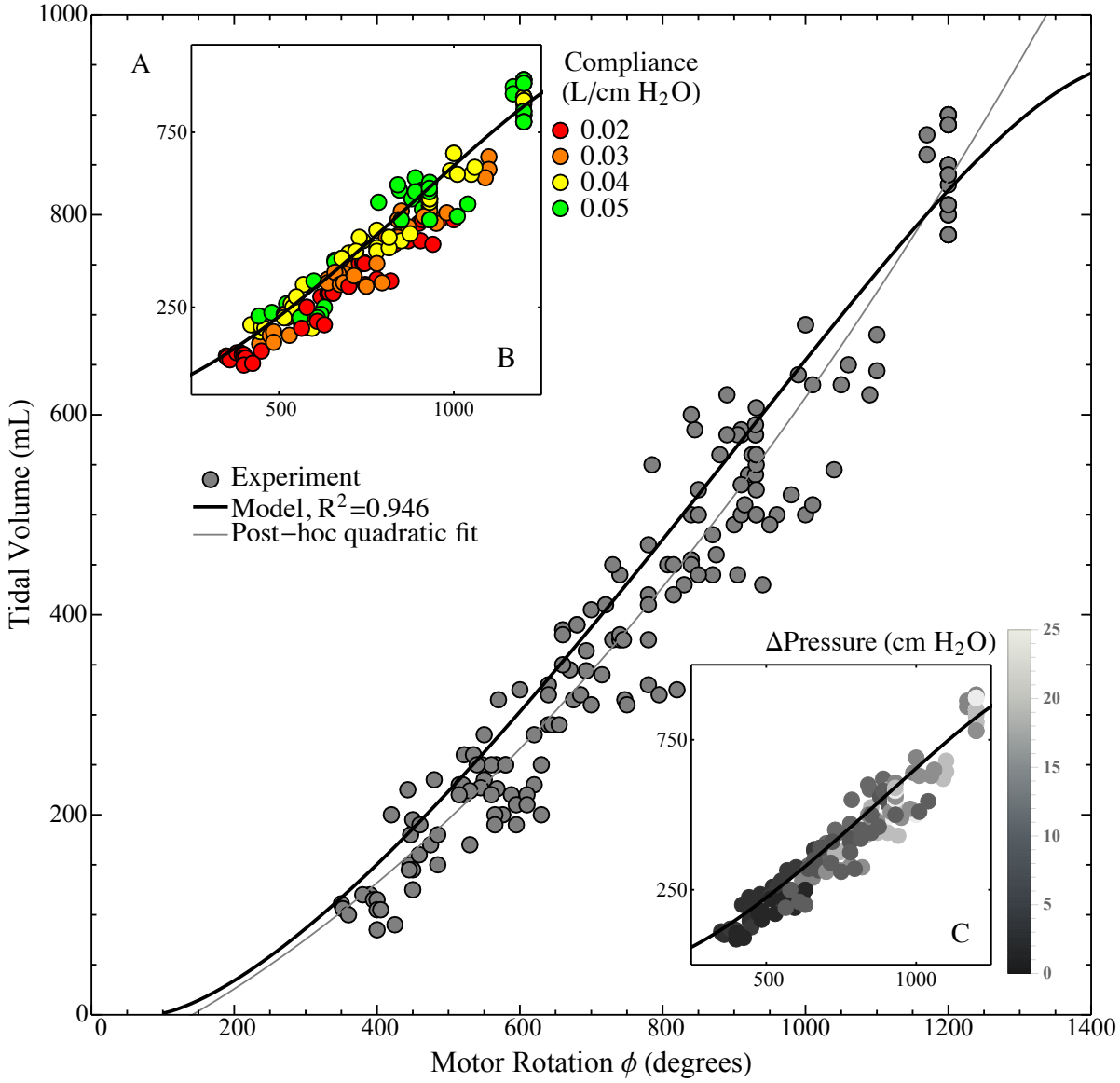

Figure B.4: Tidal volume is related to the rotation of the motor via compression of the bag, as indicated (A) by the experimental results compared with a model $V_{\text{tidal}} = V_{\text{tidal}}(\phi)$ constructed from the geometry (see Supplementary Information for the full derivation). Furthermore, a post-hoc quadratic curve fit ($3.47 \times 10^{-4}\phi^2 + 0.322\phi - 52.5$ with $R^2 = 0.953$) is provided showing a slightly improved fit, indicating that a quadratic function can adequately represent the tidal volume as a function of the angle ϕ. In B, the volume corresponding to a given motor rotation is seen to increase with compliance—accounting for the spread in the data along with experimental error. In C, the difference between peak pressure and PEEP is seen to increase along the model, as expected due to the ideal gas law.

Table B.1: Suitable MADVent Mark V operating parameter ranges

Operating Parameter	**Tested Range**
Target Inspiratory Pressure	10 – 35 cm H_2O
Tidal Volume (V_T)	200 – 1000 $m\ell$
Respiratory rate (RR)	6 – 35 bpm
Inspiratory time	1 – 3.0 sec
Low-pressure alarm threshold	0 – 20 cm H_2O
High-pressure alarm threshold	30 – 50 cm H_2O
High-volume alarm threshold	200 – 1000 $m\ell$
Low-volume alarm threshold	200 – 1000 $m\ell$

designed for the same purpose and are interchangeably used by hospital personnel.

The overall range of parameters at which the system is capable of operating is listed in Table B.1, which align with the specifications recommended for ARDS patients [313–315]. In addition to the testing reported in Fig. B.4, we also performed tests according to ISO standards (see Supplementary Information), which dictate airway resistance values.

The hardware on the system allows for a volume-driven approach to ventilation in addition to pressure-controlled ventilation with continuous feedback. Tests were conducted to characterize the system operating in this mode, but a proper continuous feedback volume-control system would require an in-line flow sensor, adding to the cost and complexity of the system. However, we did test the system as a volume-driven ventilator and the results are included in Fig. B.5. This mode was solely for evaluation purposes and will not be available to the healthcare provider. The volume-driven mode includes user-defined limits for low and high pressure. Baseline conditions were set to 5.0 cm H_2O PEEP, a respiratory rate of 14 breaths per minute, and an initial compliance of 0.03 $\ell/(cm\ H_2O)$. Figure B.5A illustrates a drastic change in compliance resulting in the trigger of a high-pressure alarm. Examples where a high-pressure alarm would be triggered are a blockage in the endotracheal tube, drastic change in patient lung compliance, or bronchospasm. The alarm was programmed to trigger upon two consecutive high pressure events, after which the system will release the bag compression arm and commence a new respiration cycle at lower tidal volumes but increased rate in order to meet the minute ventilation set by the healthcare provider. In the event of an accidental disconnection of the endotracheal tube or other significant leak in the system, a low-pressure alarm will be triggered as illustrated in Fig. B.5B. Kinking of the endotracheal tube or a sudden change in resistance can lead to a high-pressure alarm as plotted in Fig. B.5C.

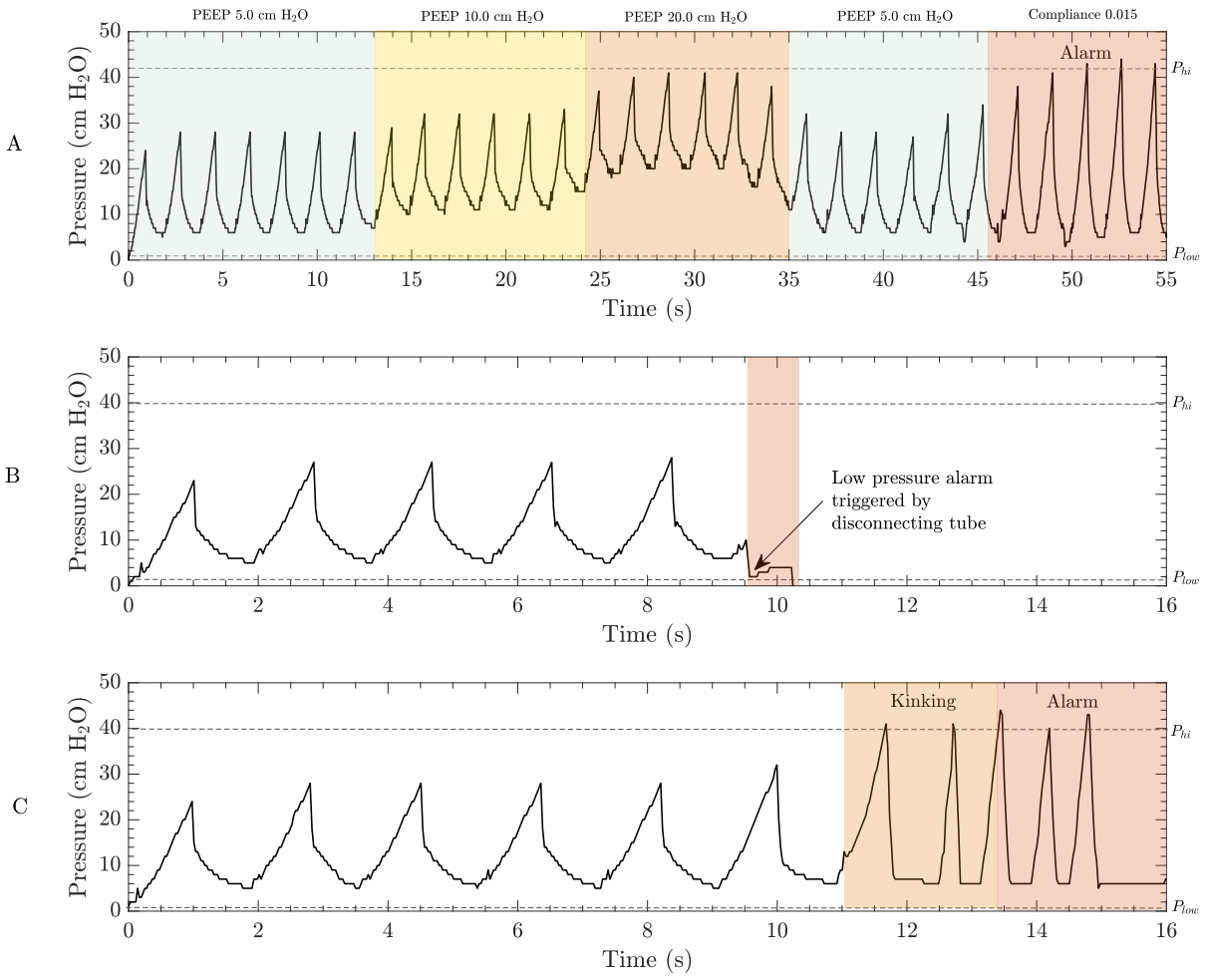

Figure B.5: The volume-driven version of the MADVent comes with alarms for high and low pressure that can be set between 0 and 50 cm H_2O defined by the caregiver. The system was initially set at a rate of 34 breaths per minute, a PEEP value of 5 cm H_2O was chosen and compliance on the lung simulator set to 0.03 $\ell/(cm\ H_2O)$. A) The low and high-pressure alarm thresholds were set to 2 cm H_2O and 42 cm H_2O respectively. PEEP values were increased from 5 cm H_2O to 20 cm H_2O and lowered back down to 5.0 cm H_2O to ensure that the in-line pressure sensor could detect and display changes in pressure values. A high-pressure condition was simulated by decreasing patient lung compliance. The system triggered an alarm once the pressure went above 42 cm H_2O. B) The low-pressure alarm is triggered once the in-line pressure value drops below the lower limit. A low-pressure situation was simulated by disconnecting the endotracheal tube to trigger an alarm which results in the system immediately stopping. C) In the event that the tubing is kinked or there is a blockage in the endotracheal tube, the pressure starts to rise until the upper threshold is reached. This triggers a high-pressure alarm and causes the system to resume ventilation at a lower volume, but at an increased rate according to the set minute ventilation.

B.5 Discussion

A number of solutions have been proposed to address the anticipated shortage of traditional ventilators during the COVID-19 outbreak [329, 330], including other low-cost ventilators [331, 332]. Splitting one ventilator among two or more patients, re-purposing continuous positive airway pressure (CPAP) machines, placing large orders for existing high cost commercial ventilators, and bringing retired ventilators out of storage are some of the proposed solutions to meet the demand for reliable ventilators. Although there have been several cases [329, 333] of healthcare workers around the world splitting ventilators for shared use among two or more patients, this method still requires further testing to better ensure safety of all patients on the shared circuit [330]. Placing large orders for ventilators has put a strain on supply chains, many of which are located in countries that are severely affected by the pandemic. Bringing retired ventilators out of storage and re-purposing CPAP machines could have unintended consequences due to component failures and a lack of testing for off-label use.

There are currently multiple groups working in parallel to develop ventilation solutions with the similar goal of providing care to patients with COVID-19. Notable devices are the Puritan Bennett^{TM} 560 (PB560) developed by Medtronic and released under a temporary license to the public, the E-Vent in development at the Massachusetts Institute of Technology [326], and the Coventor developed at the University of Minnesota [327]. The PB560 is a fully functioned portable ventilator system, and with its functions come increased cost and increased complexity, both of which are issues when ventilators need to be produced quickly and in great quantity, especially with over-burdened supply lines in times of crisis. The MADVent, E-Vent, and Coventor ventilators are all less expensive and simpler to manufacture than the PB560.

The following information on the MIT E-Vent is representative of the publicly available information at the time of this publication's writing, but may not remain accurate as their development process continues [326, 327]. The MIT E-Vent is described as a volume-control system with the option of being triggered by spontaneous respirations. The question of calibration is mentioned in the MIT E-Vent's results summary [334], but follow-up data releases do not mention this, although their implementation of a spirometer to measure flow does partially address this. The E-Vent does have the advantage of multiple rounds of testing in a porcine model in addition to a robust team of

volunteers working on its development [334].

Although the Coventor [327] recently received FDA Emergency Use Authorization, details on controls, features, patient safety, and clinician controls are not publicly available. It is not clear what degree of patient monitoring is possible with the Coventor, what respiratory parameters can be adjusted, or the presence and function of alarms based on publicly available information. At the time of this publication, it is estimated that the MADVent Mark V will cost around $250. This is likely less than the E-Vent, whose publicly cited costs vary between $150-$500 and lack recent robust citation, and certainly less than the publicly disclosed $1000 cost of the Coventor ($150 advertised component-only cost) [326, 327]. The MIT E-vent and the MADVent have similar alarm and failure mode functions, but little is currently known about the Coventor's function or safety features.

Compared to these other low-resource ventilator examples, the UCSD MADVent Mark V is the only device offering pressure-controlled ventilation. Despite the relative simplicity of our mechanical system, the electronics of the system allow clinicians wide-ranging control over ventilation characteristics and alarms. A conclusion on which device is most appropriate or effective in the current crisis cannot be responsibly made until all devices under consideration have publicly available testing, calibration, and safety monitoring information. Low-cost, scalable ventilator technologies such as this may also have applications for use in rural environments, low-resource environments, natural disaster response, and other mass casualty scenarios.[335, 336]

The MADVent Mark V pressure-controlled ventilator works by compressing a self-inflating bag-valve resuscitator until a target inspiratory pressure is reached. The peak pressure is set by the healthcare provider. An in-line pressure sensor continually monitors pressure and provides feedback to control a lever arm that compresses the self-inflating bag until the set peak pressure is attained. The system reaches the peak pressure at the inspiratory time per the set respiratory rate, both as selected by the healthcare provider, and serving to define the remaining expiratory time and idle time between breaths. We prefer this pressure-controlled version of the MADVent as it is continually regulated by means of a feedback loop between the pressure sensor and the motor, in order to accommodate changes in lung compliance and enable finer control over the delivery of mechanical ventilation. Though we have chosen the pressure-controlled version for our final configuration, the hardware on the system is also capable of supporting a volume-driven ventilation system that relies on compressing the bag by a specific amount corresponding to the volume set

by the healthcare provider (Fig. B.5). This version would also monitor in-line pressure during the breath cycle using the same sensors as the pressure-controlled version. Here, we make the distinction between pressure-controlled and volume-driven approaches by pointing out there is no continuous feedback from any sensed tidal volume delivered to the patient and the compression of the bag, because there is no integrated flow sensor for this purpose. On the other hand, if it is determined that breath triggering is a necessary feature, the MADVent Mark V already has the hardware in place to provide this feature. This would allow the ventilator to be used in patients with lower levels of sedation and who are capable of initiating breaths but require the support of a ventilator.

One well-known limitation of using bipolar stepper motors in any application is the high current they require when operating at low speeds. As the motor pauses for a period of time at each step in order to provide slow rotation, it could theoretically lead to high power consumption and overheating. However, this difficulty was foreseen, and both pulse-width modulation (PWM) and current limiting was programmed into the controller to eliminate it. Pulse-width modulation lowers the effective voltage drop across the motor for longer step times, in turn lowering the current draw of the motor. A motor controller was chosen that is capable of significantly higher current than the programmed limit current, preventing the motor controller from overheating. The robust motor controller set up and software limiting, combined with a power supply capable of no more than 3 A of constant draw, comprehensively limits possible thermal issues. As an added measure of safety, the temperature of the motor and circuits are continually monitored using temperature sensors and a visual alarm indicator is displayed in the event of the system overheating. The rotational position of the motor and the arm are tracked during operation to ensure mechanical integrity during operation. The limitations of individual ventilator components were identified and thorough testing performed to ensure no mechanical or electrical problems during operation. A full list of all potential errors and the systems we have in place to mitigate these risks are included in the Supplementary Information.

Patients with COVID-19 and ARDS can require mechanical ventilation for over two weeks[337, 338]. All electrical components in the system were chosen to provide reliable continuous operation for such patients over weeks of use. The mechanical components chosen are all capable of withstanding the standard operational load due to the weight of the motor and that of the battery. The components of the ventilator were placed to balance the system across the width and length of the frame, and

to provide easy access for maintenance and disinfection. The materials of the ventilator may be sanitized with conventional disinfectants such as 0.5% hydrogen peroxide, 0.5% sodium hypochlorite (bleach), and 70% ethanol. As part of the design we attempted to integrate as many standard hospital items as possible. These items, such as the bag-valve resuscitator and PEEP valve, are staples of the hospital environment and have already undergone rigorous testing for safety, longevity, and compatibility with conventional disinfectants.

B.6 Conclusions

The lack of adequate ventilatory support has already caused preventable deaths in the first few months of the COVID-19 pandemic and more can be expected unless ventilators can quickly be provided to areas overburdened with COVID-19 patients. The MADVent is capable of safely meeting the diverse ventilation requirements of COVID-19 patients because its parameters are adjustable over the broad ranges necessary for ARDS patients. The combination of off-the-shelf components and laser-cut parts in addition to our choice of mechanically driven pressure control makes our design both low cost and rapidly manufacturable. The essential qualities of safety, effectiveness, low cost, and rapid manufacturablity make it a feasible option for scaled production and use in current and future health crises.

The MADVent Mark V ventilator generates a pressure curve up to a set level in a prescribed rise time. A widely available resuscitator bag is used to drive flow with a simple mechanical system controlled by a widely available stepper motor, controller, and system-on-a-chip computer. Standard control of PEEP is provided with a disposable off-the-shelf valve. Volume and pressure alarms are provided for safety and additional alarms provided for electronics temperature and device failure detection ensure that healthcare providers will be informed if this life support system shows signs of failure. Tidal volumes and pressure waveforms were tested and verified on a lung simulator, confirming the prototype is effective over the intended operating range.

As we continue to refine the design of the MADVent, we intend to add additional features to bring our low-cost ventilator even closer to the expansive capabilities of standard ICU mechanical ventilators, though still at a reduced cost, to facilitate broader adoption. Much of the high cost associated with modern ventilators is a consequence of thorough adherence to safety regulations

and ensuring the manufacturer is responsive to patient outcomes per FDA requirements. Our ventilator is not a substitute for these well-designed and produced systems. Instead, our system—like many other recent low-cost ventilators arising in this emergency—is a ventilator of last resort during a pandemic or mass casualty event. The design focuses upon patient safety, simplicity of manufacturing, and modularity. The system, in its current state of development, can easily accommodate new modules that enable more sophisticated features, such as flow monitoring, which can enable additional ventilation modes and provide healthcare operators more information regarding a patient's breathing.

B.7 Acknowledgement

This chapter, in full, is a reprint of A. Vasan et. al. (2020) "MADVent: A low-cost ventilator for patients with COVID-19." *Medical devices and sensors* 3.4 (2020): e10106. The dissertation author is the first author of this article.

Appendix C

Supplementary information for chapter 3

Whole cell current clamp electrophysiology: additional results

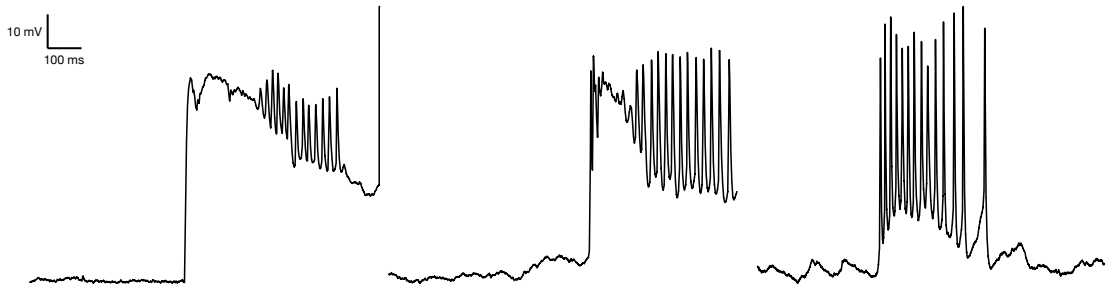

Figure C.1: Current clamp electrophysiology data on neurons subjected to ultrasound stimuli.

Whole cell current clamp electrophysiology performed on rat primary neurons shows rapid oscillations of voltage corresponding to the onset of the ultrasound stimulus (Fig. C.1).

Centered-difference scheme for deflection verification

A centered difference scheme may also be employed for discretizing the temporal and spatial derivatives of the partial differential equation governing membrane deflection:

$$\frac{\partial^2 u}{\partial t^2} = \frac{u_i^{n+1} - 2u_i^n + u_i^{n-1}}{h^2}, \tag{C.1a}$$

$$\frac{\partial^2 u}{\partial x^2} = \frac{u_{i+1}^n - 2u_i^n + u_{i-1}^n}{k^2}, \tag{C.1b}$$

$$\frac{\partial^3 u_z}{\partial x^2 \partial t} = \frac{u_{i+1}^n - u_{i+1}^{n-1} - 2(u_i^n - u_i^{n-1}) + u_i^n - u_{i-1}^{n-1}}{hk^2}. \tag{C.1c}$$

The displacement of the membrane may be determined by iterating with these finite difference equations.

Deflection due to cavitation-based models

Our model predicts deflection due to ultrasound and in later sections, we demonstrate how deflection results in the generation of action potentials. This is in contrast to other proposed mechanisms for cellular activity mediated by ultrasound, for example, by cavitation [81]. Cavitation may either be inertial, where there is rapid collapse, or stable, where there are steady pulsations. Given the range of ultrasound parameters that may induce a neuronal response, there are major limitations with a cavitation based approach for explaining the observed bioeffects as cavitation is less likely to occur at higher frequencies of operation. In addition to the particular frequency used for stimulation, another important factor is the nature of the waveform of acoustic excitation, as highlighted by Apfel *et al.* [339]. The range of pressures used for ultrasound stimulation are well below cavitation thresholds in the media of interest: tissue. This is critical as the displacement of the membrane at sub-cavitation pressures may be approximated by the perturbation in the fluid due to the ultrasound field alone.

In order to investigate any potential cavitation-based phenomenon, we considered the Rayleigh-Plesset equation and simulated the oscillation of a nanometer scale bubble. The smaller the bubble, the higher its resonance frequency and faster its response to an applied acoustic field. If the frequency of the applied field is less than the natural frequency of the bubble, the bubble

may respond to tension in the fluid field thereby causing it to expand. When the field exerts a compressional event, the bubble collapses and results in a transient cavitation event. There are three possibilities: the bubble is large and has a slow response time to a compressional field, the bubble is very small and growth is inhibited by surface tension, or there is an intermediate size for the given acoustic field parameters that undergoes transient cavitation. The Blake threshold [340] establishes a lower limit for bubble radius, above which transient behavior is possible. This threshold is established by using the quasi-static assumption for pressure within the bubble and the liquid outside it,

$$p_L = \left(P_0 + \frac{2\sigma}{R_0}\right)\left(\frac{R_0}{R}\right)^{3\kappa} - \frac{2\sigma}{R} \tag{C.2}$$

where $\kappa = 1$ for the isothermal case. Differentiating the above with respect to R establishes the lower limit for transient cavitation. Assuming a 5 nm bubble, the critical radius is found to be 6.23 nm. Neppiras and Noltingk [341] established an upper threshold for bubble size, corresponding to a particular frequency above which transient cavitation conditions are not realized. This is given by

$$\rho\omega^2 R_0^2 = 3\gamma\left(P_a + \frac{2\sigma}{R_0}\right) - \frac{2\sigma}{R_0} \tag{C.3}$$

where ρ is the liquid density and γ is the ratio of specific heats for the gas within the bubble. Assuming a frequency of 7 MHz, the upper threshold is found to be 0.1 µm. One of the theories for ultrasound mediated neuromodulation [81] suggests a cavitation based phenomenon governing the generation of action potentials due to stable cavitation of dissolved gas in between the lipid bilayer. The lipid bilayer is approximately 7 nm thick [342] and considering the limits established with the above thresholds, stable cavitaion may be possible for a bubble enclosed within the leaflets. Forced oscillations of a bubble for small amplitudes is best described by the Rayleigh-Plesset equation,

$$\frac{d^2R}{dt^2} + \frac{3}{2R}\left(\frac{dR}{dt}\right)^2 = \frac{1}{\rho}\left\{\left(P_0 + \frac{2\sigma}{R_0} - P_v\right)\left(\frac{R_0}{R}\right)^{3\kappa} + P_v - \frac{2\sigma}{R} - \frac{4\eta}{R}\frac{dR}{dt} - P_0 - P(t)\right\} \tag{C.4}$$

where η is the viscosity of the surrounding fluid and $P(t)$ is the sinusoidal pressure variation due to the ultrasound field. Applying the Rayleigh-Plesset equation to a bubble with diameter on the

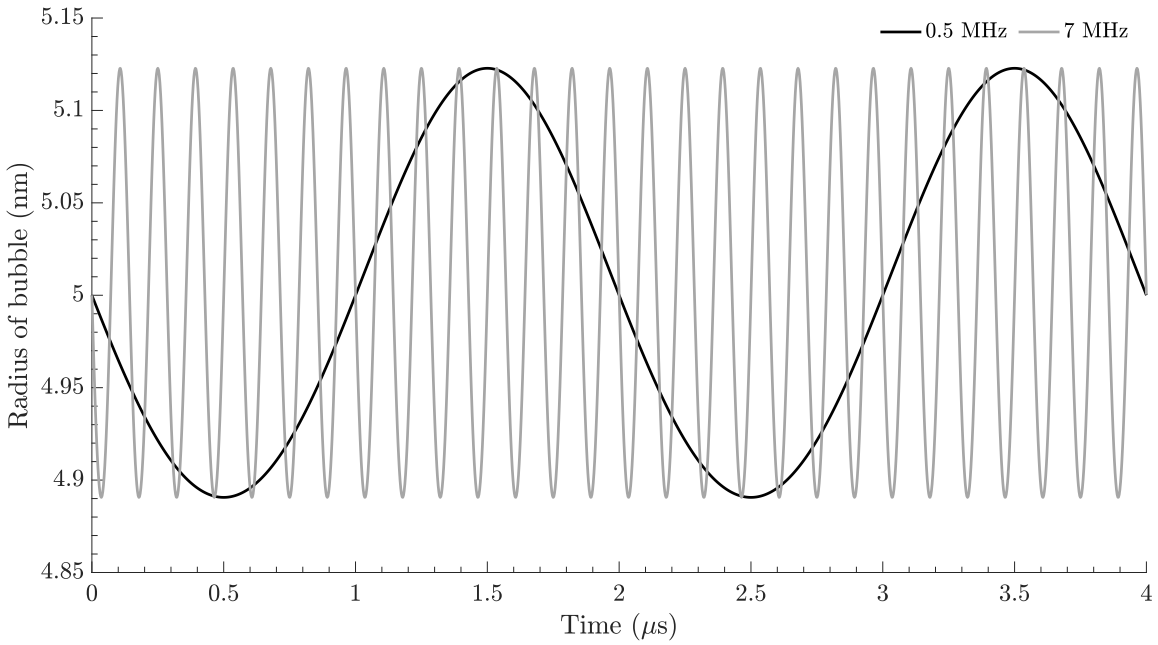

Figure C.2: Sub nanometer oscillations of a bubble due to pressures at the mechanical index limit, showing that cavitation-based phenomenon are likely not responsible for generating membrane deflection.

order of magnitude of the thickness of the bilayer results in deflections on the order of $\pm 0.08\,\text{nm}$.

For a bubble diameter of 5 nm under the influence of a 1 MPa sinusoidal pressure field, the maximum change in radius is $\pm 0.08\,\text{nm}$ from the initial diameter, comparable to Brownian thermal motion of lipids in the bilayer. This holds true even at lower stimulation frequencies, for example 0.5 MHz at a pressure of 1.35 MPa (corresponding to an MI of 1.9) results in a deflection of $\pm 0.1\,\text{nm}$.

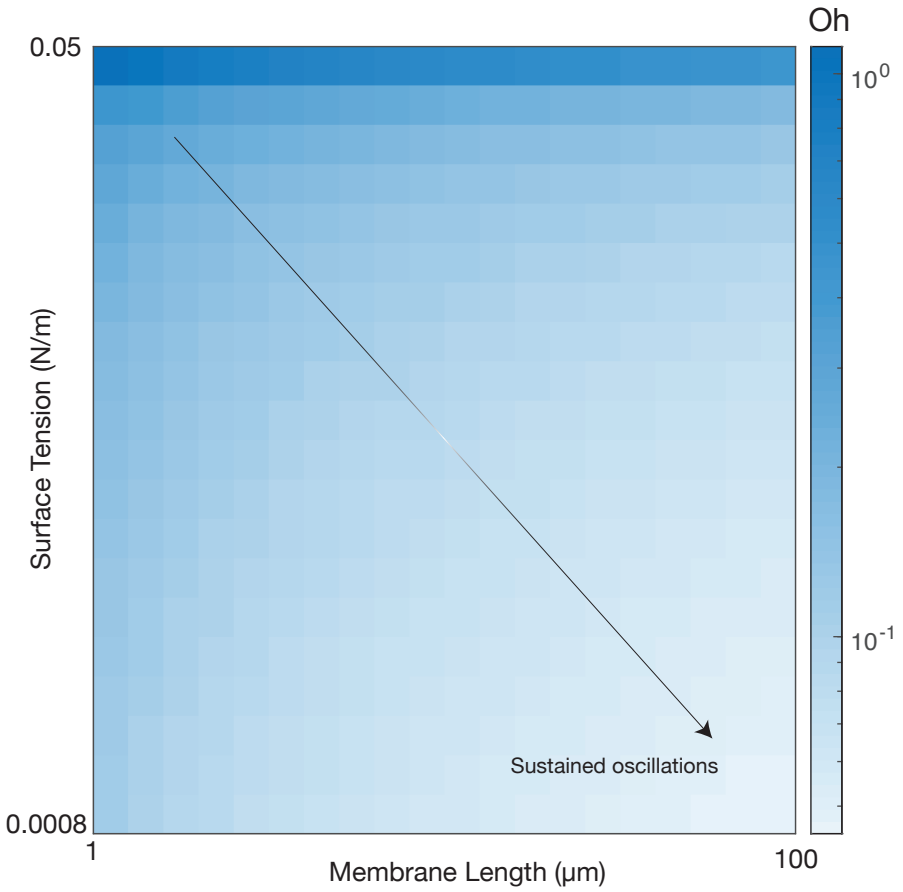

Figure C.3: The Oh number relates viscous forces to inertial and surface tension forces. In this case, the viscosity and the density are assumed constant. Increased forces result in damped oscillation on the membrane. Changes in surface tension and membrane length determine if the membrane may sustain oscillations.

Bibliography

[1] R. W. Wood, A. L. Loomis, {XXXVIII}.The physical and biological effects of high-frequency sound-waves of great intensity, The London, Edinburgh, and Dublin Philosophical Magazine and Journal of Science 4 (22) (1927) 417–436.

[2] A. Dalmoro, A. A. Barba, G. Lamberti, M. D'Amore, Intensifying the microencapsulation process: Ultrasonic atomization as an innovative approach, European Journal of Pharmaceutics and Biopharmaceutics 80 (3) (2012) 471–477.

[3] K. Namiyama, H. Nakamura, K. Kokubo, D. Hosogai, Development of ultrasonic atomizer and its application to SI engines, SAE Transactions (1989) 701–711.

[4] A. Qi, L. Y. Yeo, J. R. Friend, Interfacial destabilization and atomization driven by surface acoustic waves, Physics of Fluids 20 (7) (2008) 74103.

[5] J. Wang, H. Hu, A. Ye, J. Chen, P. Zhang, Experimental investigation of surface acoustic wave atomization, Sensors and Actuators A: Physical 238 (2016) 1–7.

[6] A. James, B. Vukasinovic, M. K. Smith, A. Glezer, Vibration-induced drop atomization and bursting, Journal of Fluid Mechanics 476 (2003) 1–28.

[7] C. A. Randall, N. Kim, J.-P. Kucera, W. Cao, T. R. Shrout, Intrinsic and extrinsic size effects in fine-grained morphotropic-phase-boundary lead zirconate titanate ceramics, Journal of the American Ceramic Society 81 (3) (1998) 677–688.

[8] S. C. Tsai, S. K. Lin, R. W. Mao, C. S. Tsai, Ejection of uniform micrometer-sized droplets from {Faraday} waves on a millimeter-sized water drop, Physical Review Letters 108 (15) (2012) 154501.

[9] Y.-R. Jeng, C.-C. Su, G.-H. Feng, Y.-Y. Peng, G.-P. Chien, A PZT-driven atomizer based on a vibrating flexible membrane and a micro-machined trumpet-shaped nozzle array, Microsystem Technologies 15 (6) (2009) 865–873.

[10] D. Lupascu, J. Rödel, Fatigue in bulk lead zirconate titanate actuator materials, Advanced Engineering Materials 7 (10) (2005) 882–898.

[11] A. Kawamata, H. Hosaka, T. Morita, Non-hysteresis and perfect linear piezoelectric performance of a multilayered lithium niobate actuator, Sensors and Actuators A: Physical 135 (2) (2007) 782–786.

[12] A. Qi, L. Yeo, J. Friend, J. Ho, The Extraction Of Liquid, Protein Molecules and Yeast Cells From Paper Through Surface Acoustic Wave Atomization, Lab on a Chip 10 (4) (2010) 470–476.

[13] S. Collignon, O. Manor, J. Friend, Improving and predicting fluid atomization via hysteresis-free thickness vibration of lithium niobate, Advanced Functional Materials 28 (8) (2018) 1704359.

[14] A. W. Lawson, The vibration of piezoelectric plates, Physical Review 62 (1-2) (1942) 71.

[15] Y. Fukushima, O. Nishizawa, H. Sato, A performance study of a laser doppler vibrometer for measuring waveforms from piezoelectric transducers, IEEE Transactions on Ultrasonics, Ferroelectrics, and Frequency Control 56 (7) (2009) 1442–1450.

[16] S. T. Thoroddsen, T. G. Etoh, K. Takehara, High-speed imaging of drops and bubbles, Annual Reviews in Fluid Mechanics 40 (2008) 257–285.

[17] A. J. Yule, Y. Al-Suleimani, On droplet formation from capillary waves on a vibrating surface, Proceedings of the Royal Society of London. Series A: Mathematical, Physical and Engineering Sciences 456 (1997) (2000) 1069–1085.

[18] E. D. Hirleman, Modeling of multiple scattering effects in Fraunhofer diffraction particle size analysis, in: Optical Particle Sizing, Springer, 1988, pp. 159–175.

[19] M. R. Schroeder, Binaural dissimilarity and optimum ceilings for concert halls: More lateral sound diffusion, Journal of the Acoustical Society of America 65 (4) (1979) 958–963.

[20] M. R. Schröder, Diffuse sound reflection by maximum- length sequences, Journal of the Acoustical Society of America 57 (1) (1975) 149–150.

[21] Y. Zhu, X. Fan, B. Liang, J. Cheng, Y. Jing, Ultrathin acoustic metasurface-based schroeder diffuser, Phys. Rev. X 7 (2017) 021034. doi:10.1103/PhysRevX.7.021034.
URL https://link.aps.org/doi/10.1103/PhysRevX.7.021034

[22] J. Huang, P. E. Dupont, A. Undurti, J. K. Triedman, R. O. Cleveland, Producing diffuse ultrasound reflections from medical instruments using a quadratic residue diffuser, Ultrasound in Medicine & Biology 32 (5) (2006) 721–727.

[23] J. Behrens, S. Langelier, A. R. Rezk, G. Lindner, L. Y. Yeo, J. R. Friend, Microscale anechoic architecture: acoustic diffusers for ultra low power microparticle separation via traveling surface acoustic waves, Lab on a Chip 15 (1) (2015) 43–46.

[24] K. Melde, A. G. Mark, T. Qiu, P. Fischer, Holograms for acoustics, Nature 537 (7621) (2016) 518–522.

[25] S. Jiménez-Gambín, N. Jiménez, J. M. Benlloch, F. Camarena, Holograms to focus arbitrary ultrasonic fields through the skull, Physical Review Applied 12 (1) (2019) 014016.

[26] P. N. Wells, Ultrasound imaging, Physics in Medicine & Biology 51 (13) (2006) R83.

[27] M. Kinoshita, N. McDannold, F. A. Jolesz, K. Hynynen, Noninvasive localized delivery of herceptin to the mouse brain by MRI-guided focused ultrasound-induced blood–brain barrier disruption, Proceedings of the National Academy of Sciences 103 (31) (2006) 11719–11723.

[28] D. K. Piech, B. C. Johnson, K. Shen, M. M. Ghanbari, K. Y. Li, R. M. Neely, J. E. Kay, J. M. Carmena, M. M. Maharbiz, R. Muller, A wireless millimetre-scale implantable neural stimulator with ultrasonically powered bidirectional communication, Nature Biomedical Engineering 4 (2) (2020) 207–222.

[29] Y. Tufail, A. Yoshihiro, S. Pati, M. M. Li, W. J. Tyler, Ultrasonic neuromodulation by brain stimulation with transcranial ultrasound, Nature Protocols 6 (9) (2011) 1453–1470.

[30] S. Wang, X. Guo, W. Xiu, Y. Liu, L. Ren, H. Xiao, F. Yang, Y. Gao, C. Xu, L. Wang, Accelerating thrombolysis using a precision and clot-penetrating drug delivery strategy by nanoparticle-shelled microbubbles, Science Advances 6 (31) (2020).

[31] K. Hynynen, R. M. Jones, Image-guided ultrasound phased arrays are a disruptive technology for non-invasive therapy, Physics in Medicine & Biology 61 (17) (2016) R206.

[32] G. Li, W. Qiu, Z. Zhang, Q. Jiang, M. Su, R. Cai, Y. Li, F. Cai, Z. Deng, D. Xu, H. Zhang, H. Zheng, Noninvasive ultrasonic neuromodulation in freely moving mice, IEEE Transactions on Biomedical Engineering 66 (1) (2019) 217–224. doi:10.1109/TBME.2018.2821201.

[33] J. Song, A. Pulkkinen, Y. Huang, K. Hynynen, Investigation of standing-wave formation in a human skull for a clinical prototype of a large-aperture, transcranial MR-guided focused ultrasound (mrgfus) phased array: an experimental and simulation study, IEEE Transactions on Biomedical Engineering 59 (2) (2011) 435–444.

[34] R. D. Airan, K. B. Pauly, Hearing out ultrasound neuromodulation, Neuron 98 (5) (2018) 875–877.

[35] T. Azuma, K.-i. Kawabata, S.-i. Umemura, M. Ogihara, J. Kubota, A. Sasaki, H. Furuhata, Bubble generation by standing wave in water surrounded by cranium with transcranial ultrasonic beam, Japanese Journal of Applied Physics 44 (6S) (2005) 4625.

[36] M. Daffertshofer, A. Gass, P. Ringleb, M. Sitzer, U. Sliwka, T. Els, O. Sedlaczek, W. J. Koroshetz, M. G. Hennerici, Transcranial low-frequency ultrasound-mediated thrombolysis in brain ischemia: increased risk of hemorrhage with combined ultrasound and tissue plasminogen activator: results of a phase II clinical trial, Stroke 36 (7) (2005) 1441–1446.

[37] C. Baron, J.-F. Aubry, M. Tanter, S. Meairs, M. Fink, Simulation of intracranial acoustic fields in clinical trials of sonothrombolysis, Ultrasound in Medicine & Biology 35 (7) (2009) 1148–1158.

[38] M. Morozov, D. Damjanovic, N. Setter, The nonlinearity and subswitching hysteresis in hard and soft PZT, Journal of the European Ceramic Society 25 (12) (2005) 2483–2486.

[39] S. Ibsen, A. Tong, C. Schutt, S. Esener, S. H. Chalasani, Sonogenetics is a non-invasive approach to activating neurons in caenorhabditis elegans, Nature Communications 6 (1) (2015) 1–12.

[40] M. Duque, C. A. Lee-Kubli, Y. Tufail, U. Magaram, J. M. Lopez, E. Edsinger, A. Vasan, R. Shiao, C. Weiss, J. Friend, S. H. Chalasani, Targeted millisecond-scale activation of cells using non-invasive sonogenetics, bioRxiv (2020). doi:10.1101/2020.10.14.338699.
URL https://www.biorxiv.org/content/early/2020/10/15/2020.10.14.338699

[41] A. Vasan, J. Orosco, U. Magaram, M. Duque, C. Weiss, Y. Tufail, S. H. Chalasani, J. Friend, Ultrasound mediated cellular deflection results in cellular depolarization, Advanced Science Accepted 27 September (2021).

[42] K. Reinhold, A. D. Lien, M. Scanziani, Distinct recurrent versus afferent dynamics in cortical visual processing, Nature Neuroscience 18 (12) (2015) 1789–1797.

[43] K. K. Sellers, D. V. Bennett, A. Hutt, J. H. Williams, F. Fröhlich, Awake vs. anesthetized: layer-specific sensory processing in visual cortex and functional connectivity between cortical areas, Journal of Neurophysiology 113 (10) (2015) 3798–3815.

[44] P. Muralt, N. Ledermann, J. Paborowski, A. Barzegar, S. Gentil, B. Belgacem, S. Petitgrand, A. Bosseboeuf, N. Setter, Piezoelectric micromachined ultrasonic transducers based on PZT thin films, IEEE Transactions on Ultrasonics, Ferroelectrics, and Frequency Control 52 (12) (2005) 2276–2288.

[45] Y. Hou, J.-S. Kim, S. Ashkenazi, S.-W. Huang, L. J. Guo, M. O'Donnell, Broadband all-optical ultrasound transducers, Applied Physics Letters 91 (7) (2007) 073507.

[46] D. R. Namjoshi, W. H. Cheng, K. A. McInnes, K. M. Martens, M. Carr, A. Wilkinson, J. Fan, J. Robert, A. Hayat, P. A. Cripton, C. L. Wellington, Merging pathology with biomechanics using chimera (closed-head impact model of engineered rotational acceleration): a novel, surgery-free model of traumatic brain injury, Molecular Neurodegeneration 9 (1) (2014) 55.

[47] H. Wang, Y. Ma, H. Yang, H. Jiang, Y. Ding, H. Xie, MEMS ultrasound transducers for endoscopic photoacoustic imaging applications, Micromachines 11 (10) (2020) 928.

[48] R. Turyn, The correlation function of a sequence of roots of 1 (corresp.), IEEE Transactions on Information Theory 13 (3) (1967) 524–525.

[49] H. Kuttruff, Sound absorption by pseudostochastic diffusers (Schroeder diffusers), Applied Acoustics 42 (3) (1994) 215–231.

[50] R. L. King, J. R. Brown, W. T. Newsome, K. B. Pauly, Effective parameters for ultrasound-induced in vivo neurostimulation, Ultrasound in Medicine & Biology 39 (2) (2013) 312–331.

[51] R. J. Wood, The challenge of manufacturing between macro and micro: Classic ways of folding paper into dynamic shapes–origami, pop-up books–inspire methods to engineer millimeter-scale machines, American Scientist 102 (2) (2014) 124–132.

[52] P. Morris, A. Hurrell, A. Shaw, E. Zhang, P. Beard, A Fabry–Pérot fiber-optic ultrasonic hydrophone for the simultaneous measurement of temperature and acoustic pressure, The Journal of the Acoustical Society of America 125 (6) (2009) 3611–3622.

[53] T.-W. Chen, T. J. Wardill, Y. Sun, S. R. Pulver, S. L. Renninger, A. Baohan, E. R. Schreiter, R. A. Kerr, M. B. Orger, V. Jayaraman, et al., Ultrasensitive fluorescent proteins for imaging neuronal activity, Nature 499 (7458) (2013) 295–300.

[54] D. P. Darrow, Focused ultrasound for neuromodulation, Neurotherapeutics 16 (1) (2019) 88–99.

[55] J. Ye, S. Tang, L. Meng, X. Li, X. Wen, S. Chen, L. Niu, X. Li, W. Qiu, H. Hu, et al., Ultrasonic control of neural activity through activation of the mechanosensitive channel MscL, Nano Letters 18 (7) (2018) 4148–4155.

[56] J. Kubanek, J. Shi, J. Marsh, D. Chen, C. Deng, J. Cui, Ultrasound modulates ion channel currents, Scientific Reports 6 (1) (2016) 1–14.

[57] Z. Qiu, J. Guo, S. Kala, J. Zhu, Q. Xian, W. Qiu, G. Li, T. Zhu, L. Meng, R. Zhang, et al., The mechanosensitive ion channel piezo1 significantly mediates in vitro ultrasonic stimulation of neurons, iScience 21 (2019) 448–457.

[58] L. A. Gimeno, E. Martin, O. Wright, B. E. Treeby, Experimental assessment of skull aberration and transmission loss at 270 kHz for focused ultrasound stimulation of the primary visual cortex, in: 2019 IEEE International Ultrasonics Symposium (IUS), IEEE, 2019, pp. 556–559.

[59] S. M. Langelier, L. Y. Yeo, J. Friend, UV epoxy bonding for enhanced SAW transmission and microscale acoustofluidic integration, Lab on a Chip 12 (16) (2012) 2970–2976.

[60] H. S. Mayberg, A. M. Lozano, V. Voon, H. E. McNeely, D. Seminowicz, C. Hamani, J. M. Schwalb, S. H. Kennedy, Deep brain stimulation for treatment-resistant depression, Neuron 45 (5) (2005) 651–660.

[61] J. M. Bronstein, M. Tagliati, R. L. Alterman, A. M. Lozano, J. Volkmann, A. Stefani, F. B. Horak, M. S. Okun, K. D. Foote, P. Krack, et al., Deep brain stimulation for parkinson disease: an expert consensus and review of key issues, Archives of Neurology 68 (2) (2011) 165–165.

[62] D. A. Groves, V. J. Brown, Vagal nerve stimulation: a review of its applications and potential mechanisms that mediate its clinical effects, Neuroscience & Biobehavioral Reviews 29 (3) (2005) 493–500.

[63] J. De Kroon, J. Van der Lee, M. J. IJzerman, G. Lankhorst, Therapeutic electrical stimulation to improve motor control and functional abilities of the upper extremity after stroke: a systematic review, Clinical Rehabilitation 16 (4) (2002) 350–360.

[64] M. Ranjan, A. Boutet, S. Bhatia, A. Wilfong, W. Hader, M. R. Lee, A. R. Rezai, P. D. Adelson, Neuromodulation beyond neurostimulation for epilepsy: Scope for focused ultrasound, Expert Review of Neurotherapeutics 19 (10) (2019) 937–943.

[65] B. Y. Chow, E. S. Boyden, Optogenetics and translational medicine, Science Translational Medicine 5 (177) (2013) 177ps5–177ps5.

[66] J. G. English, B. L. Roth, Chemogenetics—a transformational and translational platform, JAMA Neurology 72 (11) (2015) 1361–1366.

[67] V. Busskamp, S. Picaud, J.-A. Sahel, B. Roska, Optogenetic therapy for retinitis pigmentosa, Gene Therapy 19 (2) (2012) 169.

[68] L. Fenno, O. Yizhar, K. Deisseroth, The development and application of optogenetics, Annual Review of Neuroscience 34 (2011).

[69] H. H. Yoon, J. H. Park, Y. H. Kim, J. Min, E. Hwang, C. J. Lee, J.-K. Francis Suh, O. Hwang, S. R. Jeon, Optogenetic inactivation of the subthalamic nucleus improves forelimb akinesia in a rat model of parkinson disease, Neurosurgery 74 (5) (2014) 533–541.

[70] W. M. Grill, S. E. Norman, R. V. Bellamkonda, Implanted neural interfaces: biochallenges and engineered solutions, Annual Review of Biomedical Engineering 11 (2009) 1–24.

[71] J. W. Salatino, K. A. Ludwig, T. D. Y. Kozai, E. K. Purcell, Glial responses to implanted electrodes in the brain, Nature Biomedical Engineering 1 (11) (2017) 862–877.

[72] A. S. Tolias, F. Sultan, M. Augath, A. Oeltermann, E. J. Tehovnik, P. H. Schiller, N. K. Logothetis, Mapping cortical activity elicited with electrical microstimulation using FMRI in the macaque, Neuron 48 (6) (2005) 901–911.

[73] T. Wagner, A. Valero-Cabre, A. Pascual-Leone, Noninvasive human brain stimulation, Annual Reviews of Biomedical Engineering 9 (2007) 527–565.

[74] A. T. Barker, The history and basic principles of magnetic nerve stimulation, Electroencephalogr Clin Neurophysiol Suppl. 51 (1999) 3–21.

[75] E. S. Boyden, F. Zhang, E. Bamberg, G. Nagel, K. Deisseroth, Millisecond-timescale, genetically targeted optical control of neural activity, Nature Neuroscience 8 (9) (2005) 1263–1268.

[76] P. Aldrin-Kirk, T. Björklund, Practical considerations for the use of dreadd and other chemogenetic receptors to regulate neuronal activity in the mammalian brain, in: Viral Vectors for Gene Therapy, Springer, 2019, pp. 59–87.

[77] J. O. Szablowski, A. Bar-Zion, M. G. Shapiro, Achieving spatial and molecular specificity with ultrasound-targeted biomolecular nanotherapeutics, Accounts of Chemical Research 52 (9) (2019) 2427–2434.

[78] J. Blackmore, S. Shrivastava, J. Sallet, C. R. Butler, R. O. Cleveland, Ultrasound neuromodulation: A review of results, mechanisms and safety, Ultrasound in Medicine & Biology 45 (7) (2019) 1509–1536.

[79] E. N. Harvey, The effect of high frequency sound waves on heart muscle and other irritable tissues, American Journal of Physiology-Legacy Content 91 (1) (1929) 284–290.

[80] T. Yang, J. Chen, B. Yan, D. Zhou, Transcranial ultrasound stimulation: a possible therapeutic approach to epilepsy, Medical Hypotheses 76 (3) (2011) 381–383.

[81] M. Plaksin, S. Shoham, E. Kimmel, Intramembrane cavitation as a predictive bio-piezoelectric mechanism for ultrasonic brain stimulation, Physical Review X 4 (1) (2014) 011004.

[82] H. Guo, M. Hamilton II, S. J. Offutt, C. D. Gloeckner, T. Li, Y. Kim, W. Legon, J. K. Alford, H. H. Lim, Ultrasound produces extensive brain activation via a cochlear pathway, Neuron 98 (5) (2018) 1020–1030.

[83] F. Di Giacinto, M. De Spirito, G. Maulucci, Low-intensity ultrasound induces thermodynamic phase separation of cell membranes through a nucleation–condensation process, Ultrasound in Medicine & Biology 45 (5) (2019) 1143–1150.

[84] M. L. Prieto, Ö. Oralkan, B. T. Khuri-Yakub, M. C. Maduke, Dynamic response of model lipid membranes to ultrasonic radiation force, PLoS One 8 (10) (2013) e77115.

[85] K. Iwasa, I. Tasaki, R. C. Gibbons, Swelling of nerve fibers associated with action potentials, Science 210 (4467) (1980) 338–339.

[86] Z. Gil, S. D. Silberberg, K. L. Magleby, Voltage-induced membrane displacement in patch pipettes activates mechanosensitive channels, Proceedings of the National Academy of Sciences 96 (25) (1999) 14594–14599.

[87] S. A. Lee, H. A. Kamimura, M. T. Burgess, E. E. Konofagou, Displacement imaging for focused ultrasound peripheral nerve neuromodulation, IEEE Transactions on Medical Imaging 39 (11) (2020) 3391–3402.

[88] T. Heimburg, A. D. Jackson, On soliton propagation in biomembranes and nerves, Proceedings of the National Academy of Sciences 102 (28) (2005) 9790–9795.

[89] M. Krieg, G. Fläschner, D. Alsteens, B. M. Gaub, W. H. Roos, G. J. L. Wuite, H. E. Gaub, C. Gerber, Y. F. Dufrêne, D. J. Müller, Atomic force microscopy-based mechanobiology, Nature Reviews Physics 1 (1) (2019) 41–57.

[90] B. M. Gaub, K. C. Kasuba, E. Mace, T. Strittmatter, P. R. Laskowski, S. A. Geissler, A. Hierlemann, M. Fussenegger, B. Roska, D. J. Müller, Neurons differentiate magnitude and location of mechanical stimuli, Proceedings of the National Academy of Sciences 117 (2) (2020) 848–856.

[91] P. L. Frederix, P. D. Bosshart, A. Engel, Atomic force microscopy of biological membranes, Biophysical Journal 96 (2) (2009) 329–338.

[92] H. M. Nussenzveig, Cell membrane biophysics with optical tweezers, European Biophysics Journal 47 (5) (2018) 499–514.

[93] B. Javidi, A. Markman, S. Rawat, T. O'Connor, A. Anand, B. Andemariam, Sickle cell disease diagnosis based on spatio-temporal cell dynamics analysis using 3d printed shearing digital holographic microscopy, Optics Express 26 (10) (2018) 13614–13627.

[94] F. Zernike, Phase contrast, a new method for the microscopic observation of transparent objects part II, Physica 9 (10) (1942) 974–986.

[95] R. Allen, G. David, The Zeiss-Nomarski differential interference equipment for transmitted-light microscopy, Zeitschrift für Wissenschaftliche Mikroskopie und Mikroskopische Technik 69 (4) (1969) 193–221.

[96] B. Rappaz, P. Marquet, E. Cuche, Y. Emery, C. Depeursinge, P. J. Magistretti, Measurement of the integral refractive index and dynamic cell morphometry of living cells with digital holographic microscopy, Optics Express 13 (23) (2005) 9361–9373.

[97] U. Schnars, W. P. Jüptner, Digital recording and numerical reconstruction of holograms, Measurement Science and Technology 13 (9) (2002) R85.

[98] F. Dubois, L. Joannes, J.-C. Legros, Improved three-dimensional imaging with a digital holography microscope with a source of partial spatial coherence, Applied Optics 38 (34) (1999) 7085–7094.

[99] A. Stadelmaier, J. H. Massig, Compensation of lens aberrations in digital holography, Optics Letters 25 (22) (2000) 1630–1632.

[100] R. L. King, J. R. Brown, W. T. Newsome, K. B. Pauly, Effective parameters for ultrasound-induced in vivo neurostimulation., Ultrasound in Medicine & Biology 39 (2) (2013) 312–331.

[101] G. Kim, P. Kosterin, A. Obaid, B. Salzberg, A mechanical spike accompanies the action potential in mammalian nerve terminals, Biophysical Journal 92 (9) (2007) 3122–3129.

[102] A. Teti, Regulation of cellular functions by extracellular matrix., Journal of the American Society of Nephrology 2 (10) (1992) S83.

[103] M. Israelowitz, B. Weyand, S. Rizvi, P. M. Vogt, H. P. von Schroeder, Development of a laminar flow bioreactor by computational fluid dynamics, Journal of Healthcare Engineering 3 (3) (2012) 455–476.

[104] Y. Guyot, F. Luyten, J. Schrooten, I. Papantoniou, L. Geris, A three-dimensional computational fluid dynamics model of shear stress distribution during neotissue growth in a perfusion bioreactor, Biotechnology and Bioengineering 112 (12) (2015) 2591–2600.

[105] C. K. Holland, R. E. Apfel, An improved theory for the prediction of microcavitation thresholds, IEEE Transactions on Ultrasonics, Ferroelectrics, and Frequency Control 36 (2) (1989) 204–208.

[106] C. C. Church, C. Labuda, K. Nightingale, A theoretical study of inertial cavitation from acoustic radiation force impulse imaging and implications for the mechanical index, Ultrasound in Medicine and Biology 41 (2) (2015) 472–485.

[107] American Institute of Ultrasound in Medicine, Statement on mammalian biological effects in tissues without gas bodies (March 2015).

[108] C. Yan, A. Li, B. Zhang, W. Ding, Q. Luo, H. Gong, Automated and accurate detection of soma location and surface morphology in large-scale 3d neuron images, PLoS One 8 (4) (2013) e62579.

[109] A. Blumlein, N. Williams, J. J. McManus, The mechanical properties of individual cell spheroids, Scientific Reports 7 (1) (2017) 1–10.

[110] C. D. Cox, N. Bavi, B. Martinac, Origin of the force: the force-from-lipids principle applied to piezo channels, in: Current Topics in Membranes, Vol. 79, Elsevier, 2017, pp. 59–96.

[111] A. L. Hodgkin, A. F. Huxley, A quantitative description of membrane current and its application to conduction and excitation in nerve, The Journal of Physiology 117 (4) (1952) 500–544.

[112] L. Abbott, T. B. Kepler, Model neurons: from hodgkin-huxley to hopfield, in: Statistical mechanics of neural networks, Springer, 1990, pp. 5–18.

[113] G. Eyal, M. B. Verhoog, G. Testa-Silva, Y. Deitcher, J. C. Lodder, R. Benavides-Piccione, J. Morales, J. DeFelipe, C. P. de Kock, H. D. Mansvelder, et al., Unique membrane properties and enhanced signal processing in human neocortical neurons, eLife 5 (2016) e16553.

[114] H. Chen, D. Garcia-Gonzalez, A. Jérusalem, Computational model of the mechanoelectrophysiological coupling in axons with application to neuromodulation, Physical Review E 99 (3) (2019) 032406.

[115] L. D. Mosgaard, K. A. Zecchi, T. Heimburg, Mechano-capacitive properties of polarized membranes, Soft Matter 11 (40) (2015) 7899–7910.

[116] B. Martinac, J. Adler, C. Kung, Mechanosensitive ion channels of E. coli activated by amphipaths, Nature 348 (6298) (1990) 261.

[117] K. Hayakawa, H. Tatsumi, M. Sokabe, Actin stress fibers transmit and focus force to activate mechanosensitive channels, Journal of Cell Science 121 (4) (2008) 496–503.

[118] J. Guo, F. Sachs, F. Meng, Fluorescence-based force/tension sensors: a novel tool to visualize mechanical forces in structural proteins in live cells, Antioxidants & Redox Signaling 20 (6) (2014) 986–999.

[119] Z. Fan, H. Liu, M. Mayer, C. X. Deng, Spatiotemporally controlled single cell sonoporation, Proceedings of the National Academy of Sciences of the United States of America 109 (41) (2012) 16486–16491.

[120] P. S. Balasubramanian, A. Singh, C. Xu, A. Lal, Ghz ultrasonic chip-scale device induces ion channel stimulation in human neural cells, Scientific Reports 10 (1) (2020) 3075.

[121] Z. Lin, W. Zhou, X. Huang, K. Wang, J. Tang, L. Niu, L. Meng, H. Zheng, On-chip ultrasound modulation of pyramidal neuronal activity in hippocampal slices, Advanced Biosystems 2 (8) (2018) 1800041.

[122] Lyncée-tec, Specifications of high-speed digital holographic imaging system, https://www.lynceetec.com/high-speed-dhm/#tab-3 (2020).

[123] F. Jähnig, What is the surface tension of a lipid bilayer membrane?, Biophysical Journal 71 (3) (1996) 1348–1349.

[124] N. Riley, Steady streaming, Annual Review of Fluid Mechanics 33 (1) (2001) 43–65.

[125] W.-T. Huang, D. Levitt, Theoretical calculation of the dielectric constant of a bilayer membrane, Biophysical Journal 17 (2) (1977) 111–128.

[126] A. Vasan, W. Connacher, J. Friend, Fabrication and characterization of thickness mode piezoelectric devices for atomization and acoustofluidics, Journal of Visualized Experiments (2020). doi:10.3791/61015.
URL https://www.jove.com/t/61015

[127] W. J. Fry, F. Fry, J. Barnard, R. Krumins, J. Brennan, Ultrasonic lesions in the mammalian central nervous system, Science 122 (3168) (1955) 517–518.

[128] E. Martin, B. Werner, R. Bauer, K. van Leyen, D. Coluccia, J. Fandino, Clinical neurological hifu applications: The zurich experience, Translational Cancer Research 3 (5) (2014) 449–458.

[129] N. Lipsman, T. G. Mainprize, M. L. Schwartz, K. Hynynen, A. M. Lozano, Intracranial applications of magnetic resonance-guided focused ultrasound, Neurotherapeutics 11 (3) (2014) 593–605.

[130] T. R. Wang, R. Dallapiazza, W. J. Elias, Neurological applications of transcranial high intensity focused ultrasound, International Journal of Hyperthermia 31 (3) (2015) 285–291.

[131] K. Hynynen, N. McDannold, N. A. Sheikov, F. A. Jolesz, N. Vykhodtseva, Local and reversible blood–brain barrier disruption by noninvasive focused ultrasound at frequencies suitable for trans-skull sonications, Neuroimage 24 (1) (2005) 12–20.

[132] N. McDannold, C. D. Arvanitis, N. Vykhodtseva, M. S. Livingstone, Temporary disruption of the blood–brain barrier by use of ultrasound and microbubbles: Safety and efficacy evaluation in rhesus macaquesblood–brain barrier disruption via focused ultrasound, Cancer Research 72 (14) (2012) 3652–3663.

[133] L. H. Treat, N. McDannold, N. Vykhodtseva, Y. Zhang, K. Tam, K. Hynynen, Targeted delivery of doxorubicin to the rat brain at therapeutic levels using mri-guided focused ultrasound, International Journal of Cancer 121 (4) (2007) 901–907.

[134] A. Alonso, E. Reinz, B. Leuchs, J. Kleinschmidt, M. Fatar, B. Geers, I. Lentacker, M. G. Hennerici, S. C. De Smedt, S. Meairs, Focal delivery of aav2/1-transgenes into the rat brain by localized ultrasound-induced blood-brain-barrier opening, Molecular Therapy-Nucleic Acids 2 (2013) e73.

[135] M. L. Khraiche, W. B. Phillips, N. Jackson, J. Muthuswamy, Ultrasound induced increase in excitability of single neurons, in: 2008 30th Annual International Conference of the IEEE Engineering in Medicine and Biology Society, IEEE, 2008, pp. 4246–4249.

[136] W. J. Tyler, Y. Tufail, M. Finsterwald, M. L. Tauchmann, E. J. Olson, C. Majestic, Remote excitation of neuronal circuits using low-intensity, low-frequency ultrasound, PloS One 3 (10) (2008) e3511.

[137] Y. Tufail, A. Matyushov, N. Baldwin, M. L. Tauchmann, J. Georges, A. Yoshihiro, S. I. H. Tillery, W. J. Tyler, Transcranial pulsed ultrasound stimulates intact brain circuits, Neuron 66 (5) (2010) 681–694.

[138] W. Lee, H. Kim, Y. Jung, I.-U. Song, Y. A. Chung, S.-S. Yoo, Image-guided transcranial focused ultrasound stimulates human primary somatosensory cortex, Scientific reports 5 (1) (2015) 1–10.

[139] W. Lee, H.-C. Kim, Y. Jung, Y. A. Chung, I.-U. Song, J.-H. Lee, S.-S. Yoo, Transcranial focused ultrasound stimulation of human primary visual cortex, Scientific Reports 6 (1) (2016) 1–12.

[140] M. R. Bachtold, P. C. Rinaldi, J. P. Jones, F. Reines, L. R. Price, Focused ultrasound modifications of neural circuit activity in a mammalian brain, Ultrasound in Medicine & Biology 24 (4) (1998) 557–565.

[141] W. Legon, P. Bansal, R. Tyshynsky, L. Ai, J. K. Mueller, Transcranial focused ultrasound neuromodulation of the human primary motor cortex, Scientific Reports 8 (1) (2018) 1–14.

[142] H. Guo, S. J. Offutt, M. Hamilton II, Y. Kim, C. D. Gloeckner, D. P. Zachs, J. K. Alford, H. H. Lim, Ultrasound does not activate but can inhibit in vivo mammalian nerves across a wide range of parameters, Scientific Reports 12 (1) (2022) 1–14.

[143] K. Yu, X. Niu, E. Krook-Magnuson, B. He, Intrinsic functional neuron-type selectivity of transcranial focused ultrasound neuromodulation, Nature Communications 12 (1) (2021) 1–17.

[144] W. D. O'Brien Jr, Ultrasound–biophysics mechanisms, Progress in Biophysics and Molecular Biology 93 (1-3) (2007) 212–255.

[145] W. J. Tyler, Noninvasive neuromodulation with ultrasound? a continuum mechanics hypothesis, The Neuroscientist 17 (1) (2011) 25–36.

[146] T. Sato, M. G. Shapiro, D. Y. Tsao, Ultrasonic neuromodulation causes widespread cortical activation via an indirect auditory mechanism, Neuron 98 (5) (2018) 1031–1041.

[147] G. Buzsáki, C. A. Anastassiou, C. Koch, The origin of extracellular fields and currents—eeg, ecog, lfp and spikes, Nature Reviews Neuroscience 13 (6) (2012) 407–420.

[148] S. Chauvette, M. Volgushev, I. Timofeev, Origin of active states in local neocortical networks during slow sleep oscillation, Cerebral Cortex 20 (11) (2010) 2660–2674.

[149] T. W. Margrie, M. Brecht, B. Sakmann, In vivo, low-resistance, whole-cell recordings from neurons in the anaesthetized and awake mammalian brain, Pflügers Archiv 444 (4) (2002) 491–498.

[150] C. C. Petersen, T. T. Hahn, M. Mehta, A. Grinvald, B. Sakmann, Interaction of sensory responses with spontaneous depolarization in layer 2/3 barrel cortex, Proceedings of the National Academy of Sciences 100 (23) (2003) 13638–13643.

[151] T.-i. Kim, J. G. McCall, Y. H. Jung, X. Huang, E. R. Siuda, Y. Li, J. Song, Y. M. Song, H. A. Pao, R.-H. Kim, et al., Injectable, cellular-scale optoelectronics with applications for wireless optogenetics, Science 340 (6129) (2013) 211–216.

[152] R. C. Craddock, S. Jbabdi, C.-G. Yan, J. T. Vogelstein, F. X. Castellanos, A. Di Martino, C. Kelly, K. Heberlein, S. Colcombe, M. P. Milham, Imaging human connectomes at the macroscale, Nature methods 10 (6) (2013) 524–539.

[153] D. C. Van Essen, S. M. Smith, D. M. Barch, T. E. Behrens, E. Yacoub, K. Ugurbil, W.-M. H. Consortium, et al., The wu-minn human connectome project: an overview, Neuroimage 80 (2013) 62–79.

[154] C. Grienberger, A. Konnerth, Imaging calcium in neurons, Neuron 73 (5) (2012) 862–885.

[155] B. F. Grewe, F. Helmchen, Optical probing of neuronal ensemble activity, Current opinion in neurobiology 19 (5) (2009) 520–529.

[156] F. Helmchen, W. Denk, Deep tissue two-photon microscopy, Nature methods 2 (12) (2005) 932–940.

[157] W. Göbel, B. M. Kampa, F. Helmchen, Imaging cellular network dynamics in three dimensions using fast 3d laser scanning, Nature methods 4 (1) (2007) 73–79.

[158] K. Svoboda, R. Yasuda, Principles of two-photon excitation microscopy and its applications to neuroscience, Neuron 50 (6) (2006) 823–839.

[159] E. E. Cho, J. Drazic, M. Ganguly, B. Stefanovic, K. Hynynen, Two-photon fluorescence microscopy study of cerebrovascular dynamics in ultrasound-induced blood—brain barrier opening, Journal of Cerebral Blood Flow & Metabolism 31 (9) (2011) 1852–1862.

[160] A. Y. Shih, J. D. Driscoll, P. J. Drew, N. Nishimura, C. B. Schaffer, D. Kleinfeld, Two-photon microscopy as a tool to study blood flow and neurovascular coupling in the rodent brain, Journal of Cerebral Blood Flow & Metabolism 32 (7) (2012) 1277–1309.

[161] H. Adelsberger, O. Garaschuk, A. Konnerth, Cortical calcium waves in resting newborn mice, Nature neuroscience 8 (8) (2005) 988–990.

[162] M. Schoen, H. Asoglu, H. F. Bauer, H.-P. Müller, A. Abaei, A. K. Sauer, R. Zhang, T.-j. Song, J. Bockmann, J. Kassubek, et al., Shank3 transgenic and prenatal zinc-deficient autism mouse models show convergent and individual alterations of brain structures in mri, Frontiers in Neural Circuits (2019) 6.

[163] E. Martianova, S. Aronson, C. D. Proulx, Multi-fiber photometry to record neural activity in freely-moving animals, JoVE (Journal of Visualized Experiments) (152) (2019) e60278.

[164] C. K. Kim, S. J. Yang, N. Pichamoorthy, N. P. Young, I. Kauvar, J. H. Jennings, T. N. Lerner, A. Berndt, S. Y. Lee, C. Ramakrishnan, et al., Simultaneous fast measurement of circuit dynamics at multiple sites across the mammalian brain, Nature methods 13 (4) (2016) 325–328.

[165] Y. Sych, M. Chernysheva, L. T. Sumanovski, F. Helmchen, High-density multi-fiber photometry for studying large-scale brain circuit dynamics, Nature methods 16 (6) (2019) 553–560.

[166] J. H. Jennings, R. L. Ung, S. L. Resendez, A. M. Stamatakis, J. G. Taylor, J. Huang, K. Veleta, P. A. Kantak, M. Aita, K. Shilling-Scrivo, et al., Visualizing hypothalamic network dynamics for appetitive and consummatory behaviors, Cell 160 (3) (2015) 516–527.

[167] J. Blackmore, S. Shrivastava, J. Sallet, C. R. Butler, R. O. Cleveland, Ultrasound neuromodulation: a review of results, mechanisms and safety, Ultrasound in medicine & biology 45 (7) (2019) 1509–1536.

[168] K. Nakamura, H. Shimizu, Hysteresis-free piezoelectric actuators using linbo3 plates with a ferroelectric inversion layer, Ferroelectrics 93 (1) (1989) 211–216.

[169] A. Vasan, F. Allein, M. Duque, U. Magaram, N. Boechler, S. H. Chalasani, J. Friend, Microscale concert hall acoustics to produce uniform ultrasound stimulation for targeted sonogenetics in hstrpa1-transfected cells, Advanced NanoBiomed Research 2 (5) (2022) 2100135.

[170] H. W. Dong, The Allen reference atlas: A digital color brain atlas of the C57Bl/6J male mouse., John Wiley & Sons Inc, 2008.

[171] F.-M. Zhou, C. J. Wilson, J. A. Dani, Cholinergic interneuron characteristics and nicotinic properties in the striatum, Journal of neurobiology 53 (4) (2002) 590–605.

[172] A. Dong, K. He, B. Dudok, J. S. Farrell, W. Guan, D. J. Liput, H. L. Puhl, R. Cai, H. Wang, J. Duan, et al., A fluorescent sensor for spatiotemporally resolved imaging of endocannabinoid dynamics in vivo, Nature biotechnology 40 (5) (2022) 787–798.

[173] N. G. Hollon, E. W. Williams, C. D. Howard, H. Li, T. I. Traut, X. Jin, Nigrostriatal dopamine signals sequence-specific action-outcome prediction errors, Current Biology 31 (23) (2021) 5350–5363.

[174] B. Rudy, G. Fishell, S. Lee, J. Hjerling-Leffler, Three groups of interneurons account for nearly 100% of neocortical gabaergic neurons, Developmental neurobiology 71 (1) (2011) 45–61.

[175] S. B. Hofer, H. Ko, B. Pichler, J. Vogelstein, H. Ros, H. Zeng, E. Lein, N. A. Lesica, T. D. Mrsic-Flogel, Differential connectivity and response dynamics of excitatory and inhibitory neurons in visual cortex, Nature neuroscience 14 (8) (2011) 1045–1052.

[176] C. A. Runyan, M. Sur, Response selectivity is correlated to dendritic structure in parvalbumin-expressing inhibitory neurons in visual cortex, Journal of Neuroscience 33 (28) (2013) 11724–11733.

[177] S. J. Kuhlman, N. D. Olivas, E. Tring, T. Ikrar, X. Xu, J. T. Trachtenberg, A disinhibitory microcircuit initiates critical-period plasticity in the visual cortex, Nature 501 (7468) (2013) 543–546.

[178] D. M. Lipton, B. J. Gonzales, A. Citri, Dorsal striatal circuits for habits, compulsions and addictions, Frontiers in Systems Neuroscience 13 (2019) 28.

[179] B. W. Balleine, M. R. Delgado, O. Hikosaka, The role of the dorsal striatum in reward and decision-making, Journal of Neuroscience 27 (31) (2007) 8161–8165.

[180] A. A. Legaria, B. A. Matikainen-Ankney, B. Yang, B. Ahanonu, J. A. Licholai, J. G. Parker, A. V. Kravitz, Fiber photometry in striatum reflects primarily nonsomatic changes in calcium, Nature neuroscience 25 (9) (2022) 1124–1128.

[181] M. Pachitariu, C. Stringer, M. Dipoppa, S. Schröder, L. F. Rossi, H. Dalgleish, M. Carandini, K. D. Harris, Suite2p: beyond 10,000 neurons with standard two-photon microscopy, BioRxiv (2017) 061507.

[182] I. Tasaki, Rapid structural changes in nerve fibers and cells associated with their excitation processes, The Japanese journal of physiology 49 (2) (1999) 125–138.

[183] M. G. Shapiro, K. Homma, S. Villarreal, C.-P. Richter, F. Bezanilla, Infrared light excites cells by changing their electrical capacitance, Nature communications 3 (1) (2012) 1–11.

[184] A. Vasan, J. Orosco, U. Magaram, M. Duque, C. Weiss, Y. Tufail, S. H. Chalasani, J. Friend, Ultrasound mediated cellular deflection results in cellular depolarization, Advanced Science 9 (2) (2022) 2101950.

[185] S. Shrivastava, M. F. Schneider, Evidence for two-dimensional solitary sound waves in a lipid controlled interface and its implications for biological signalling, Journal of The Royal Society Interface 11 (97) (2014) 20140098.

[186] D. P. McManus, D. W. Dunne, M. Sacko, J. Utzinger, B. J. Vennervald, X.-N. Zhou, Schistosomiasis (primer), Nature Reviews: Disease Primers (2018).

[187] A. Trampuz, M. Jereb, I. Muzlovic, R. M. Prabhu, Clinical review: Severe malaria, Critical Care 7 (4) (2003) 315.

[188] T. Adam, S. S. Lim, S. Mehta, Z. A. Bhutta, H. Fogstad, M. Mathai, J. Zupan, G. L. Darmstadt, Cost effectiveness analysis of strategies for maternal and neonatal health in developing countries, BMJ 331 (7525) (2005) 1107.

[189] W. J. Wiersinga, B. J. Currie, S. J. Peacock, Melioidosis, New England Journal of Medicine 367 (11) (2012) 1035–1044.

[190] B. J. Currie, D. A. Dance, A. C. Cheng, The global distribution of burkholderia pseudomallei and melioidosis: an update, Transactions of the Royal Society of Tropical Medicine and Hygiene 102 (Supplement_1) (2008) S1–S4.

[191] D. Dance, Melioidosis: the tip of the iceberg?, Clinical Microbiology Reviews 4 (1) (1991) 52–60.

[192] V. Wuthiekanun, M. D. Smith, N. J. White, Survival of burkholderia pseudomallei in the absence of nutrients, Transactions of the Royal Society of Tropical Medicine and Hygiene 89 (5) (1995) 491–491.

[193] A. C. Cheng, B. J. Currie, Melioidosis: epidemiology, pathophysiology, and management, Clinical Microbiology Reviews 18 (2) (2005) 383–416.

[194] Y. Suputtamongkol, W. Chaowagul, P. Chetchotisakd, N. Lertpatanasuwun, S. Intaranongpai, T. Ruchutrakool, D. Budhsarawong, P. Mootsikapun, V. Wuthiekanun, N. Teerawatasook, A. Lulitanond, Risk factors for melioidosis and bacteremic melioidosis, Clinical Infectious Diseases 29 (2) (1999) 408–413.

[195] N. White, Melioidosis, The Lancet 361 (9370) (2003) 1715–1722.

[196] S. Wild, G. Roglic, A. Green, R. Sicree, H. King, Global prevalence of diabetes: estimates for the year 2000 and projections for 2030, Diabetes Care 27 (5) (2004) 1047–1053.

[197] P. Chetchotisakd, S. Porramatikul, P. Mootsikapun, S. Anunnatsiri, B. Thinkhamrop, Randomized, double-blind, controlled study of cefoperazone-sulbactam plus cotrimoxazole versus ceftazidime plus cotrimoxazole for the treatment of severe melioidosis, Clinical Infectious Diseases 33 (1) (2001) 29–34.

[198] N. White, W. Chaowagul, V. Wuthiekanun, D. Dance, Y. Wattanagoon, N. Pitakwatchara, Halving of mortality of severe melioidosis by ceftazidime, The Lancet 334 (8665) (1989) 697–701.

[199] M. Sookpranee, P. Boonma, W. Susaengrat, K. Bhuripanyo, S. Punyagupta, Multicenter prospective randomized trial comparing ceftazidime plus co-trimoxazole with chloramphenicol plus doxycycline and co-trimoxazole for treatment of severe melioidosis., Antimicrobial Agents and Chemotherapy 36 (1) (1992) 158–162.

[200] Y. Suputtamongkol, A. Rajchanuwong, W. Chaowagul, D. Dance, M. Smith, V. Wuthiekanun, A. Walsh, S. Pukrittayakamee, N. White, Ceftazidime vs. amoxicillin/clavulanate in the treatment of severe melioidosis, Clinical Infectious Diseases 19 (5) (1994) 846–853.

[201] M. Samuel, T. Ti, Interventions for treating melioidosis, Cochrane Database of Systematic Reviews (4) (2002).

[202] A. J. Simpson, Y. Suputtamongkol, M. D. Smith, B. J. Angus, A. Rajanuwong, V. Wuthiekanun, P. A. Howe, A. L. Walsh, W. Chaowagul, N. J. White, Comparison of imipenem and ceftazidime as therapy for severe melioidosis, Clinical Infectious Diseases 29 (2) (1999) 381–387.

[203] A. Leelarasamee, S. Bovornkitti, Melioidosis: review and update, Reviews of Infectious Diseases 11 (3) (1989) 413–425.

[204] S. Puthucheary, N. Parasakthi, M. Lee, Septicaemic melioidosis: a review of 50 cases from malaysia, Transactions of the Royal Society of Tropical Medicine and Hygiene 86 (6) (1992) 683–685.

[205] A. R. Hoffmaster, D. AuCoin, P. Baccam, H. C. Baggett, R. Baird, S. Bhengsri, D. D. Blaney, P. J. Brett, T. J. Brooks, K. A. Brown, N. Chantratita, A. C. Cheng, D. A. Dance, S. Decuypere, D. Defenbaugh, J. E. Gee, R. Houghton, P. Jorakate, G. Lertmemongkolchai, D. Limmathurotsakul, T. L. Merlin, C. Mukhopadhyay, R. Norton, S. J. Peacock, D. B. Rolim, A. J. Simpson, I. Steinmetz, R. A. Stoddard, M. M. Stokes, D. Sue, A. Tuanyok, T. Whistler, V. Wuthiekanun, H. T. Walke, Melioidosis diagnostic workshop, 2013, Emerging Infectious Diseases 21 (2) (2015).

[206] T. J. Inglis, A. Merritt, G. Chidlow, M. Aravena-Roman, G. Harnett, Comparison of diagnostic laboratory methods for identification of burkholderia pseudomallei, Journal of Clinical Microbiology 43 (5) (2005) 2201–2206.

[207] P. C. Woo, G. K. Woo, S. K. Lau, S. S. Wong, K.-y. Yuen, Single gene target bacterial identification: groel gene sequencing for discriminating clinical isolates of burkholderia pseudomallei and burkholderia thailandensis, Diagnostic Microbiology and Infectious Disease 44 (2) (2002) 143–149.

[208] M. T. Holden, R. W. Titball, S. J. Peacock, A. M. Cerdeno-Tarraga, T. Atkins, L. C. Crossman, T. Pitt, C. Churcher, K. Mungall, S. D. Bentley, M. Sebaihia, N. R. Thomson, N. Bason, I. R. Beacham, K. Brooks, K. A. Brown, N. F. Brown, G. L. Challis, I. Cherevach, T. Chillingworth, A. Cronin, B. Crossett, P. Davis, D. DeShazer, T. Feltwell, A. Fraser, Z. Hance, H. Hauser, S. Holroyd, K. Jagels, K. E. Keith, M. Maddison, S. Moule, C. Price, M. A. Quail, E. Rabbinowitsch, K. Rutherford, M. Sanders, M. Simmonds, S. Songsivilai, K. Stevens, S. Tumapa, M. Vesaratchavest, S. Whitehead, C. Yeats, B. G. Barrell, P. C. Oyston, J. Parkhill, Genomic plasticity of the causative agent of melioidosis, burkholderia pseudomallei, Proceedings of the National Academy of Sciences 101 (39) (2004) 14240–14245.

[209] A. Karger, R. Stock, M. Ziller, M. C. Elschner, B. Bettin, F. Melzer, T. Maier, M. Kostrzewa, H. C. Scholz, H. Neubauer, H. Tomaso, Pcr-based methodologies used to detect and differentiate the burkholderia pseudomallei complex: B. pseudomallei, b. mallei, and b. thailandensis, Current Issues in Molecular Biology 16 (2) (2014) 23–54.

[210] S. K. Lau, C. S. Lam, A. H. Ngan, W.-N. Chow, A. K. Wu, D. N. Tsang, W. Cindy, T.-L. Que, B. S. Tang, P. C. Woo, Matrix-assisted laser desorption ionization time-of-flight mass spectrometry for rapid identification of mold and yeast cultures of penicillium marneffei, BMC Microbiology 16 (1) (2016) 36.

[211] S. A. Cunningham, R. Patel, Importance of using bruker's security-relevant library for biotyper identification of burkholderia pseudomallei, brucella species, and francisella tularensis, Journal of Clinical Microbiology 51 (5) (2013) 1639–1640.

[212] A. Karger, R. Stock, M. Ziller, M. C. Elschner, B. Bettin, F. Melzer, T. Maier, M. Kostrzewa, H. C. Scholz, H. Neubauer, et al., Rapid identification of burkholderia mallei and burkholderia pseudomallei by intact cell matrix-assisted laser desorption/ionisation mass spectrometric typing, BMC Microbiology 12 (1) (2012) 229.

[213] T. J. Inglis, P. E. Healy, L. J. Fremlin, C. L. Golledge, Use of matrix-assisted laser desorption/ionization time-of-flight mass spectrometry analysis for rapid confirmation of burkholderia pseudomallei in septicemic melioidosis, The American Journal of Tropical Medicine and Hygiene 86 (6) (2012) 1039–1042.

[214] L. Bllaci, S. Kjellstr om, L. Eliasson, J. R. Friend, L. Y. Yeo, S. Nilsson, Fast surface acoustic wave-matrix-assisted laser desorption ionization mass spectrometry of cell response from islets of langerhans, Analytical Chemistry 85 (5) (2013) 2623–2629.

[215] A. Lew, P. Desmarchelier, Detection of pseudomonas pseudomallei by pcr and hybridization., Journal of Clinical Microbiology 32 (5) (1994) 1326–1332.

[216] D. Gal, M. Mayo, E. Spencer, A. C. Cheng, B. J. Currie, Application of a polymerase chain reaction to detect burkholderia pseudomallei in clinical specimens from patients with suspected melioidosis, The American Journal of Tropical Medicine and Hygiene 73 (6) (2005) 1162–1164.

[217] T. Shaw, C. Tellapragada, K. Vandana, D. P. AuCoin, C. Mukhopadhyay, Performance evaluation of active melioidosis detect-lateral flow assay (amd-lfa) for diagnosis of melioidosis in endemic settings with limited resources, PloS One 13 (3) (2018) e0194595.

[218] R. L. Houghton, D. E. Reed, M. A. Hubbard, M. J. Dillon, H. Chen, B. J. Currie, M. Mayo, D. S. Sarovich, V. Theobald, D. Limmathurotsakul, G. Wongsuvan, N. Chantratita, S. J.

Peacock, A. R. Hoffmaster, B. Duval, P. J. Brett, M. N. Burtnick, D. P. Aucoin, Development of a prototype lateral flow immunoassay (lfi) for the rapid diagnosis of melioidosis, PLoS Neglected Tropical Diseases 8 (3) (2014) e2727.

[219] D. Limmathurotsakul, N. Golding, D. A. Dance, J. P. Messina, D. M. Pigott, C. L. Moyes, D. B. Rolim, E. Bertherat, N. P. Day, S. J. Peacock, S. I. Hay, Predicted global distribution of burkholderia pseudomallei and burden of melioidosis, Nature Microbiology 1 (1) (2016) 15008.

[220] N. Singhal, M. Kumar, P. K. Kanaujia, J. S. Virdi, Maldi-tof mass spectrometry: an emerging technology for microbial identification and diagnosis, Frontiers in Microbiology 6 (2015) 791.

[221] E. Carbonnelle, C. Mesquita, E. Bille, N. Day, B. Dauphin, J.-L. Beretti, A. Ferroni, L. Gutmann, X. Nassif, Maldi-tof mass spectrometry tools for bacterial identification in clinical microbiology laboratory, Clinical Biochemistry 44 (1) (2011) 104–109.

[222] K. Blackfan, Lead poisoning in children with especial reference to lead as a cause of convulsions, The American Journal of the Medical Sciences (1827–1924) 153 (6) (1917) 877.

[223] J. D. Repko, P. Jones, L. Garcia Jr, C. Corum, Effects of inorganic lead on behavioral and neurologic function. final report, Tech. rep., Louisville Univ., KY (USA) (1977).

[224] M. R. Krigman, Neuropathology of heavy metal intoxication., Environmental Health Perspectives 26 (1978) 117–120.

[225] J. Markovac, G. W. Goldstein, Picomolar concentrations of lead stimulate brain protein kinase c, Nature 334 (6177) (1988) 71.

[226] T. Simons, Lead-calcium interactions in cellular lead toxicity., Neurotoxicology 14 (2-3) (1993) 77–85.

[227] P. Bushnell, R. Bowman, Effects of chronic lead ingestion on social development in infant rhesus monkeys., Neurobehavioral Toxicology 1 (3) (1979) 207–219.

[228] D. Rice, Behavioral impairments produced by developmental lead exposure: Evidence from primate research, Human Lead Exposure (1992) 138–152.

[229] A. M. Seppäläinen, S. Tola, S. Hernberg, B. Kock, Subclinical neuropathy at "safe" levels of lead exposure, Archives of Environmental Health: An International Journal 30 (4) (1975) 180–183.

[230] D. C. Bellinger, Lead contamination in flint—an abject failure to protect public health, New England Journal of Medicine 374 (12) (2016) 1101–1103.

[231] Flint water study, www.FlintWaterStudy.org, accessed: 2019-07-24 (2019).

[232] R. C. Gracia, W. R. Snodgrass, Lead toxicity and chelation therapy, American Journal of Health-System Pharmacy 64 (1) (2007) 45–53.

[233] N. Johri, G. Jacquillet, R. Unwin, Heavy metal poisoning: the effects of cadmium on the kidney, Biometals 23 (5) (2010) 783–792.

[234] Per-capita food consumption, http://www.fao.org/faostat/en/#data/FBS, accessed: 2019-07-24.

[235] Public health impact of pesticides used in agriculture, https://apps.who.int/iris/handle/10665/39772, accessed: 2019-07-24 (2019).

[236] C. N. Kesavachandran, M. Fareed, M. K. Pathak, V. Bihari, N. Mathur, A. K. Srivastava, Adverse health effects of pesticides in agrarian populations of developing countries, in: Reviews of Environmental Contamination and Toxicology, Vol. 200, Springer, 2009, pp. 33–52.

[237] R. Śpiewak, Pesticides as a cause of occupational skin diseases in farmers, Annals of Agricultural and Environmental Medicine 8 (1) (2001) 1–5.

[238] R. McConnell, F. Pacheco, K. Wahlberg, W. Klein, O. Malespin, R. Magnotti, M. Åkerblom, D. Murray, Subclinical health effects of environmental pesticide contamination in a developing country: cholinesterase depression in children, Environmental Research 81 (2) (1999) 87–91.

[239] L. Rosenstock, M. Keifer, W. E. Daniell, R. McConnell, K. Claypoole, Chronic central nervous system effects of acute organophosphate pesticide intoxication, The Lancet 338 (8761) (1991) 223–227.

[240] Total fertilizer production, http://www.fao.org/faostat/en/#data/RA, accessed: 2019-07-24 (2019).

[241] M. Roser, H. Ritchie, Fertilizer and pesticides, Our World in DataHttps://ourworldindata.org/fertilizer-and-pesticides (2019).

[242] F. Sanchez-Santed, M. T. Colomina, E. H. Hernandez, Organophosphate pesticide exposure and neurodegeneration, Cortex 74 (2016) 417–426.

[243] M. C. Alavanja, J. A. Hoppin, F. Kamel, Health effects of chronic pesticide exposure: cancer and neurotoxicity, Annual Reviews of Public Health 25 (2004) 155–197.

[244] D. Indra, R. Bellamy, P. Shyamsundar, Facing hazards at work-agricultural workers and pesticide exposure in kuttanad, kerala, South Asian Network for Development and Environmental Economics 19 (2007) 1–4.

[245] A. W. Martinez, S. T. Phillips, G. M. Whitesides, E. Carrilho, Diagnostics for the developing world: microfluidic paper-based analytical devices (2009).

[246] G. G. Lewis, J. S. Robbins, S. T. Phillips, A prototype point-of-use assay for measuring heavy metal contamination in water using time as a quantitative readout, Chemical Communications 50 (40) (2014) 5352–5354.

[247] H. Kuang, C. Xing, C. Hao, L. Liu, L. Wang, C. Xu, Rapid and highly sensitive detection of lead ions in drinking water based on a strip immunosensor, Sensors 13 (4) (2013) 4214–4224.

[248] M. Polhuijs, J. P. Langenberg, H. P. Benschop, New method for retrospective detection of exposure to organophosphorus anticholinesterases: application to alleged sarin victims of japanese terrorists, Toxicology and Applied Pharmacology 146 (1) (1997) 156–161.

[249] M. Roser, Child & infant mortality, Our World in DataHttps://ourworldindata.org/child-mortality (2019).

[250] Infant mortality in 2017, http://data.worldbank.org/data-catalog/world-development-indicators, accessed: 2019-07-24 (2018).

[251] J. E. Lawn, S. Cousens, J. Zupan, 4 million neonatal deaths: when? where? why?, The Lancet 365 (9462) (2005) 891–900.

[252] J. Zupan, E. Aahman, Perinatal mortality for the year 2000: estimates developed by who, Geneva: World Health Organization (2005) 129–33.

[253] World Health Organization, Guidelines for health care equipment donations, Tech. rep., Geneva: World Health Organization (1997).

[254] X. Zhu, H. Fang, S. Zeng, Y. Li, H. Lin, S. Shi, The impact of the neonatal resuscitation program guidelines (NRPG) on the neonatal mortality in a hospital in Zhuhai, China, Singapore Medical Journal 38 (1997) 485–487.

[255] A. Deorari, V. Paul, M. Singh, D. Vidyasagar, M. C. Network, Impact of education and training on neonatal resuscitation practices in 14 teaching hospitals in India, Annals of Tropical Paediatrics 21 (1) (2001) 29–33.

[256] J. Kattwinkel, S. Niermeyer, V. Nadkarni, J. Tibballs, B. Phillips, D. Zideman, P. Van Reempts, M. Osmond, Resuscitation of the newly born infant: an advisory statement from the pediatric working group of the international liaison committee on resuscitation, Resuscitation 40 (2) (1999) 71–88.

[257] S. Velaphi, D. Vidyasagar, The pros and cons of suctioning at the perineum (intrapartum) and post-delivery with and without meconium, in: Seminars in Fetal and Neonatal Medicine, Vol. 13(6), Elsevier, 2008, pp. 375–382.

[258] S. N. Wall, A. C. Lee, S. Niermeyer, M. English, W. J. Keenan, W. Carlo, Z. A. Bhutta, A. Bang, I. Narayanan, I. Ariawan, J. E. Lawn, Neonatal resuscitation in low-resource settings: what, who, and how to overcome challenges to scale up?, International Journal of Gynecology & Obstetrics 107 (Supplement) (2009) S47–S64.

[259] K. Costeloe, E. Hennessy, A. T. Gibson, N. Marlow, A. R. Wilkinson, The epicure study: outcomes to discharge from hospital for infants born at the threshold of viability, Pediatrics 106 (4) (2000) 659–671.

[260] N. J. Besch, P. H. Perlstein, N. K. Edwards, W. J. Keenan, J. M. Sutherland, The transparent baby bag: a shield against heat loss, New England Journal of Medicine 284 (3) (1971) 121–124.

[261] L. E. Mitchell, N. S. Adzick, J. Melchionne, P. S. Pasquariello, L. N. Sutton, A. S. Whitehead, Spina bifida, The Lancet 364 (9448) (2004) 1885–1895.

[262] A. Drugan, A. Weissman, M. I. Evans, Screening for neural tube defects, Clinics in Perinatology 28 (2) (2001) 279–287.

[263] R. Harris, R. Jennison, A. Barson, K. Laurence, E. Ruoslahti, M. Seppälä, Comparison of amniotic-fluid and maternal serum alpha-fetoprotein levels in the early antenatal diagnosis of spina bifida and anencephaly, The Lancet 303 (7855) (1974) 429–433.

[264] Q. Yang, X. Gong, T. Song, J. Yang, S. Zhu, Y. Li, Y. Cui, Y. Li, B. Zhang, J. Chang, Quantum dot-based immunochromatography test strip for rapid, quantitative and sensitive detection of alpha fetoprotein, Biosensors and Bioelectronics 30 (1) (2011) 145–150.

[265] Who medical devices, https://apps.who.int/iris/bitstream/handle/10665/274893/9789241514699-eng.pdf?ua=1, accessed: 2019-07-24 (2019).

[266] E. W. Barasa, S. Cleary, S. Molyneux, M. English, Setting healthcare priorities: a description and evaluation of the budgeting and planning process in county hospitals in Kenya, Health Policy and Planning 32 (3) (2017) 329–337.

[267] C. Blegvad, A. Skjolding, H. Broholm, H. Laursen, M. Juhler, Pathophysiology of shunt dysfunction in shunt treated hydrocephalus, Acta Neurochirurgica 155 (9) (2013) 1763–1772.

[268] B. C. Warf, Comparison of 1-year outcomes for the Chhabra and Codman-Hakim Micro Precision shunt systems in Uganda: a prospective study in 195 children, Journal of Neurosurgery 102 (4 Suppl) (2005) 358–362.

[269] J. M. Drake, J. R. Kestle, R. Milner, G. Cinalli, F. Boop, J. Piatt, S. Haines, S. J. Schiff, D. D. Cochrane, P. Steinbok, N. MacNeil, Randomized trial of cerebrospinal fluid shunt valve design in pediatric hydrocephalus, Neurosurgery 43 (2) (1998) 294–303.

[270] Neglected tropical diseases, https://www.who.int/neglected_diseases/data/ntddatabase/en/, accessed: 2019-07-24 (2019).

[271] P. J. Hotez, D. H. Molyneux, A. Fenwick, J. Kumaresan, S. E. Sachs, J. D. Sachs, L. Savioli, Control of neglected tropical diseases, New England Journal of Medicine 357 (10) (2007) 1018–1027.

[272] S. Chen, M. Ravallion, The developing world is poorer than we thought, but no less successful in the fight against poverty, The Quarterly Journal of Economics 125 (4) (2010) 1577–1625.

[273] E. F. Kjetland, P. D. Ndhlovu, E. Gomo, T. Mduluza, N. Midzi, L. Gwanzura, P. R. Mason, L. Sandvik, H. Friis, S. G. Gundersen, Association between genital schistosomiasis and HIV in rural Zimbabwean women, AIDS 20 (4) (2006) 593–600.

[274] U. F. Ekpo, C. F. Mafiana, C. O. Adeofun, A. R. Solarin, A. B. Idowu, Geographical information system and predictive risk maps of urinary schistosomiasis in Ogun State, Nigeria, BMC Infectious Diseases 8 (1) (2008) 74.

[275] P. Steinmann, J. Keiser, R. Bos, M. Tanner, J. Utzinger, Schistosomiasis and water resources development: systematic review, meta-analysis, and estimates of people at risk, The Lancet Infectious Diseases 6 (7) (2006) 411–425.

[276] D. M. Parkin, The global burden of urinary bladder cancer, Scandinavian Journal of Urology and Nephrology 42 (sup218) (2008) 12–20.

[277] M. J. van der Werf, S. J. de Vlas, S. Brooker, C. W. Looman, N. J. Nagelkerke, J. D. F. Habbema, D. Engels, Quantification of clinical morbidity associated with schistosome infection in sub-Saharan Africa, Acta Tropica 86 (2-3) (2003) 125–139.

[278] M. J. Doenhoff, D. Cioli, J. Utzinger, Praziquantel: mechanisms of action, resistance and new derivatives for schistosomiasis, Current Opinion in Infectious Diseases 21 (6) (2008) 659–667.

[279] C. H. King, S. K. Olbrych, M. Soon, M. E. Singer, J. Carter, D. G. Colley, Utility of repeated praziquantel dosing in the treatment of schistosomiasis in high-risk communities in Africa: a systematic review, PLoS Neglected Tropical Diseases 5 (9) (2011) e1321.

[280] S. De Vlas, D. Engels, A. Rabello, B. Oostburg, L. van Lieshout, A. Polderman, G. Van Oortmarssen, J. Habbema, B. Gryseels, Validation of a chart to estimate true Schistosoma mansoni prevalences from simple egg counts, Parasitology 114 (2) (1997) 113–121.

[281] W. E. C. on the Control of Schistosomiasis, The control of schistosomiasis. second report of the WHO Expert Committee. WHO Technical Report Series 830. Image WHO 92721 (1993).

[282] D. G. Colley, S. Binder, C. Campbell, C. H. King, L. A. Tchuem Tchuente, E. K. N'Goran, B. Erko, D. M. S. Karanja, N. B. Kabatereine, L. van Lieshout, S. Rathbun, A simple device for quantitative stool thick-smear technique in schistosomiasis mansoni, Revista do Instituto de Medicina Tropical de São Paulo 14 (6) (1972) 397–400.

[283] D. G. Colley, S. Binder, C. Campbell, C. H. King, L.-A. T. Tchuenté, E. K. N'Goran, B. Erko, D. M. Karanja, N. B. Kabatereine, L. van Lieshout, et al., A five-country evaluation of a point-of-care circulating cathodic antigen urine assay for the prevalence of Schistosoma mansoni, The American Journal of Tropical Medicine and Hygiene 88 (3) (2013) 426–432.

[284] D. G. Colley, A. L. Bustinduy, W. E. Secor, C. H. King, Human schistosomiasis, The Lancet 383 (9936) (2014) 2253–2264.

[285] V. E. Strong, C. J. Galanis, C. C. Riedl, V. A. Longo, F. Daghighian, J. L. Humm, S. M. Larson, Y. Fong, Portable pet probes are a novel tool for intraoperative localization of tumor deposits, Annals of Surgical Innovation and Research 3 (1) (2009) 2.

[286] D. Wichmann, M. Panning, T. Quack, S. Kramme, G.-D. Burchard, C. Grevelding, C. Drosten, Diagnosing schistosomiasis by detection of cell-free parasite dna in human plasma, PLoS Neglected Tropical Diseases 3 (4) (2009) e422.

[287] J. J. Chen, C. M. Shen, Y. W. Ko, Analytical study of a microfludic dna amplification chip using water cooling effect, Biomedical Microdevices 15 (2) (2013) 261–278.

[288] E. WHO, The control of schistosomiasis: report of a who expert committee, WHO Tech Rep Ser 728 (1985) 1–114.

[289] K. M. Bosompem, O. Owusu, E. Okanla, S. Kojima, Applicability of a monoclonal antibody-based dipstick in diagnosis of urinary schistosomiasis in the central region of ghana, Tropical Medicine & International Health 9 (9) (2004) 991–996.

[290] K. Simiyu, A. S. Daar, P. A. Singer, Stagnant health technologies in Africa, Science 330 (6010) (2010) 1483–1484.

[291] A. S. Sarvestani, K. H. Sienko, Medical device landscape for communicable and noncommunicable diseases in low-income countries, Globalization and Health 14 (1) (2018) 65.

[292] C. K. Murray, D. Bell, R. A. Gasser, C. Wongsrichanalai, Rapid diagnostic testing for malaria, Tropical Medicine & International Health 8 (10) (2003) 876–883.

[293] P. Yager, G. J. Domingo, J. Gerdes, Point-of-care diagnostics for global health, Annual Review of Biomedical Engineering 10 (1) (2008) 107–144. doi:10.1146/annurev.bioeng.10.061807.160524.

[294] H. Reyburn, H. Mbakilwa, R. Mwangi, O. Mwerinde, R. Olomi, C. Drakeley, C. J. Whitty, Rapid diagnostic tests compared with malaria microscopy for guiding outpatient treatment of febrile illness in tanzania: randomised trial, BMJ 334 (7590) (2007) 403.

[295] R. A. Malkin, Barriers for medical devices for the, Appropriate Technology (2007) 759–763.

[296] P. Howitt, A. Darzi, G. Z. Yang, H. Ashrafian, R. Atun, J. Barlow, A. Blakemore, A. M. Bull, J. Car, L. Conteh, G. S. Cooke, N. Ford, S. A. Gregson, K. Kerr, D. King, M. Kulendran, R. A. Malkin, A. Majeed, S. Matlin, R. Merrifield, H. A. Penfold, S. D. Reid, P. C. Smith, M. M. Stevens, M. R. Templeton, C. Vincent, E. Wilson, Technologies for global health, The Lancet 380 (9840) (2012) 507–535.

[297] D. Wang, B. Hu, C. Hu, F. Zhu, X. Liu, J. Zhang, B. Wang, H. Xiang, Z. Cheng, Y. Xiong, Y. Zhao, Y. Li, X. Wang, Z. Peng, Clinical characteristics of 138 hospitalized patients with 2019 novel coronavirus–infected pneumonia in wuhan, china, Journal of the American Medical Association 323 (2020) 1061–1069. doi:10.1001/jama.2020.1585.

[298] G. E. Weissman, A. Crane-Droesch, C. Chivers, T. Luong, A. Hanish, M. Z. Levy, J. Lubken, M. Becker, M. E. Draugelis, G. L. Anesi, et al., Locally informed simulation to predict hospital capacity needs during the covid-19 pandemic, Annals of Internal Medicine (2020).

[299] M. L. Ranney, V. Griffeth, A. K. Jha, Critical supply shortages — the need for ventilators and personal protective equipment during the covid-19 pandemic., New England Journal of Medicine (March 2020). doi:DOI:10.1056/NEJMp2006141.
URL https://www.nejm.org/doi/full/10.1056/NEJMp2006141?query=featured_coronavirus

[300] A. S. Fauci, H. C. Lane, R. R. Redfield, Covid-19 — navigating the uncharted., New England Journal of Medicine 382 (2020) 1268–1269. doi:DOI:10.1056/NEJMe2002387.

[301] M. Cascella, M. Rajnik, A. Cuomo, S. C. Dulebohn, R. Di Napoli, Features, evaluation and treatment coronavirus (covid-19), in: StatPearls [Internet], StatPearls Publishing, 2020.

[302] J. Phua, L. Weng, L. Ling, M. Egi, C.-M. Lim, J. V. Divatia, B. R. Shrestha, Y. M. Arabi, J. Ng, C. D. Gomersall, et al., Intensive care management of coronavirus disease 2019 (covid-19): challenges and recommendations, The Lancet Respiratory Medicine (2020).

[303] P. K. Bhatraju, B. J. Ghassemieh, M. Nichols, R. Kim, K. R. Jerome, A. K. Nalla, A. L. Greninger, S. Pipavath, M. M. Wurfel, L. Evans, et al., Covid-19 in critically ill patients in the seattle region—case series, New England Journal of Medicine (2020).

[304] X. Yang, Y. Yu, J. Xu, H. Shu, J. Xia, H. Liu, Y. Wu, L. Zhang, Z. Yu, M. Fang, T. Yu, Y. Wang, S. Pan, X. Zou, S. Yuan, Y. Shang, Clinical course and outcomes of critically ill patients with sars-cov-2 pneumonia in wuhan, china: a single-centered, retrospective, observational study, The Lancet Respiratory Medicine (04 2020).

[305] L. Rosenbaum, Facing covid-19 in italy—ethics, logistics, and therapeutics on the epidemic's front line, New England Journal of Medicine (2020).

[306] J. Xie, Z. Tong, X. Guan, B. Du, H. Qiu, A. S. Slutsky, Critical care crisis and some recommendations during the covid-19 epidemic in china, Intensive Care Medicine (March 2020). doi:doi:10.1007/s00134-020-05979-7.

[307] T. Netland, A better answer to the ventilator shortage as the pandemic rages on, https://www.weforum.org/agenda/2020/04/covid-19-ventilator-shortage-manufacturing-solution/ (April 2020).

[308] H.-C. Huang1, O. M. Araz, D. P. Morton, G. P. Johnson, P. Damien, B. Clements, L. A. Meyers, Stockpiling ventilators for influenza pandemics, Emerging Infectious Diseases 23 (2017) 914–921. doi:10.3201/eid2306.161417.

[309] A. Woodyatt, The world is scrambling to buy ventilators in the covid-19 pandemic. one country has only four of them – for 12 million people, https://www.cnn.com/2020/04/18/africa/covid-19-ventilator-shortage-intl-scli/index.html (April 2020).

[310] S. Sanche, Y. T. Lin, C. Xu, E. Romero-Severson, N. Hengartner, R. Ke, High contagiousness and rapid spread of severe acute respiratory syndrome coronavirus 2, Emerging Infectious Diseases 26 (7) (2020).

[311] V. Krishnamoorthy, M. S. Vavilala, C. N. Mock, The need for ventilators in the developing world: An opportunity to improve care and save lives, Journal of global health 4 (1) (2014).

[312] S. Morrison, Ford and gm are making tens of thousands of ventilators. it may already be too late. (Apr 2020).
URL https://www.vox.com/recode/2020/4/10/21209709/tesla-gm-ford-ventilators-coronavirus

[313] C. H. Weiss, D. W. Baker, S. Weiner, M. Bechel, M. Ragland, A. Rademaker, B. B. Weitner, A. Agrawal, R. G. Wunderink, S. D. Persell, Low tidal volume ventilation use in acute respiratory distress syndrome, Critical care medicine 44 (8) (2016) 1515.

[314] M. B. Amato, M. O. Meade, A. S. Slutsky, L. Brochard, E. L. Costa, D. A. Schoenfeld, T. E. Stewart, M. Briel, D. Talmor, A. Mercat, J.-C. M. Richard, C. R. Carvalho, R. G. Brower, Driving pressure and survival in the acute respiratory distress syndrome, New England Journal of Medicine 372 (2015) 747–755. doi:10.1056/NEJMsa1410639.

[315] E. Fan, L. Del Sorbo, E. C. Goligher, C. L. Hodgson, L. Munshi, A. J. Walkey, N. K. J. Adhikari, M. B. P. Amato, R. Branson, R. G. Brower, N. D. Ferguson, O. Gajic, L. Gattinoni, D. Hess, J. Mancebo, M. O. Meade, D. F. McAuley, A. Pesenti, V. M. Ranieri, G. D. Rubenfeld, E. Rubin, M. Seckel, A. S. Slutsky, D. Talmor, B. T. Thompson, H. Wunsch, E. Uleryk, J. Brozek, L. J. Brochard, American Thoracic Society, European Society of Intensive Care Medicine, and Society of Critical Care Medicine, An official american thoracic society/european society of intensive care medicine/society of critical care medicine clinical practice guideline: Mechanical ventilation in adult patients with acute respiratory distress syndrome, American Journal Respiratory Critical Care Medicine 195 (9) (2017) 1253–1263.

[316] J. Bourenne, S. Hraiech, A. Roch, M. Gainnier, L. Papazian, J.-M. Forel, Sedation and neuromuscular blocking agents in acute respiratory distress syndrome, Annals of Translational Medicine 5 (2017) 291–303. doi:10.21037/atm.2017.07.19.

[317] Prevention, E. T. of Acute Lung Injury (PETAL) network, Early neuromuscular blockade in the acute respiratory distress syndrome, New England Journal of Medicine 380 (2019) 1997–2008. doi:10.1056/NEJMoa1901686.

[318] D. Hinton, Emergency use authorization for ventilators (Mar 2020).
URL https://www.fda.gov/media/136423/download

[319] R. L. Dellaca', C. Veneroni, R. Farre', Trends in mechanical ventilation: are we ventilating our patients in the best possible way?, Breathe 13 (2) (2017) 84–98. arXiv:https://breathe.ersjournals.com/content/13/2/84.full.pdf, doi:10.1183/20734735.007817.
URL https://breathe.ersjournals.com/content/13/2/84

[320] S. Corp, Flow sensor, https://www.sensirion.com/en/about-us/newsroom/sensirion-specialist-articles/flow-sensor-solutions-in-modern-medical-ventilators/ (March 2020).

[321] P. J. C. Biselli, R. S. Nóbrega, F. G. Soriano, Nonlinear flow sensor calibration with an accurate syringe, Sensors 18 (7) (2018).

[322] P. R. Bachiller, J. M. McDonough, J. M. Feldman, Do new anesthesia ventilators deliver small tidal volumes accurately during volume-controlled ventilation?, Anesthesia & Analgesia 106 (5) (2008).

[323] M. J. Heulitt, S. J. Holt, T. L. Thurman, Accuracy of small tidal volume measurement comparing two ventilator airway sensors, Journal of Pediatric Intensive Care 2 (2013) 33–38.

[324] R. S. Harris, Pressure-volume curves of the respiratory system, Respiratory care 50 (1) (2005) 78–99.

[325] A. Lyazidi, A. W. Thille, G. Carteaux, F. Galia, L. Brochard, J.-C. M. Richard, Bench test evaluation of volume delivered by modern icu ventilators during volume-controlled ventilation, Intensive Care Medicine 36 (12) (2010) 2074–2080.

[326] MIT, Mit emergency ventilator (e-vent) project, https://e-vent.mit.edu/ (April 2020).

[327] U. of Minnesota, Covid-19 ventilator, https://med.umn.edu/covid19Ventilator (April 2020).

[328] Sensirion, Cmosens® technology for gas flow and differential pressure, https://www.sensirion.com/en/about-us/company/technology/cmosens-technology-for-gas-flow/ (2020).

[329] M. Abir, C. Nelson, E. W. Chan, H. Al-Ibrahim, C. Cutter, K. Patel, A. Bogart, Critical care surge response strategies for the 2020 covid-19 outbreak in the united states, Tech. rep., RAND Corporation (2020).

[330] S. for critical care in medicine, Consensus statement on multiple patients per ventilator, https://www.sccm.org/Disaster/Joint-Statement-on-Multiple-Patients-Per-Ventilato (March 2020).

[331] A. Darwood, J. McCanny, R. Kwasnicki, B. Martin, P. Jones, The design and evaluation of a novel low-cost portable ventilator, Anaesthesia 74 (11) (2019) 1406–1415.

[332] A. M. Al Husseini, H. J. Lee, J. Negrete, S. Powelson, A. T. Servi, A. H. Slocum, J. Saukkonen, Design and prototyping of a low-cost portable mechanical ventilator, Transactions of the ASME-W-Journal of Medical Devices 4 (2) (2010) 027514.

[333] B. M. Rosenthal, J. Pinkowski, J. Goldstein, 'the other option is death': New york starts sharing of ventilators, https://www.nytimes.com/2020/03/26/health/coronavirus-ventilator-sharing.html (March 2020).

[334] M. E-Vent, Testing (04 2020).
URL https://e-vent.mit.edu/testing-results/

[335] R. D. Branson, J. A. Johannigman, E. L. Daugherty, L. Rubinson, Surge capacity mechanical ventilation, Respiratory Care 53 (2008) 78–88.

[336] H. S. R. Inc., Bioterrorism and other public health emergencies: Altered standards of care in mass casualty events, https://archive.ahrq.gov/research/altstand/altstand.pdf (April 2005).

[337] A. Anzueto, F. Frutos-Vivar, A. Esteban, I. Alía, L. Brochard, T. Stewart, S. Benito, M. J. Tobin, J. Elizalde, F. Palizas, et al., Incidence, risk factors and outcome of barotrauma in mechanically ventilated patients, Intensive care medicine 30 (4) (2004) 612–619.

[338] G. L. Anesi, S. Manaker, G. Finlay, A. Bloom, Coronavirus disease 2019 (covid-19): Critical care issues, UpToDate (April 2020).

[339] R. E. Apfel, C. K. Holland, Gauging the likelihood of cavitation from short-pulse, low-duty cycle diagnostic ultrasound, Ultrasound in Medicine & Biology 17 (2) (1991) 179–185.

[340] F. Blake, Technical memo 12, Acoustics Research Laboratory, Harvard University, Cambridge, MA (1949).

[341] B. E. Noltingk, E. A. Neppiras, Cavitation produced by ultrasonics, Proceedings of the Physical Society. Section B 63 (9) (1950) 674.

[342] B. A. Lewis, D. M. Engelman, Lipid bilayer thickness varies linearly with acyl chain length in fluid phosphatidylcholine vesicles, Journal of Molecular Biology 166 (2) (1983) 211–217.